Physics – Uspekhi **59** (1) 3 – 41 (2016)

REVIEWS OF TOPICAL PROBLEMS

PACS numbers: **95.75.–z**, 98.70.Vc, **98.80.–k**

Cosmological results from the Planck space mission and their comparison with data from the WMAP and BICEP2 experiments

O V Verkhodanov

DOI: 10.3367/UFNe.0186.201601b.0003

Contents

Abstract. **We review basic results from the European Space Agency's Planck space mission, which are of crucial significance to understanding the origin and evolution of the Universe. The main stages of astrophysical and cosmological data processing pipelines are considered. The Planck results are compared with the data from the NASA WMAP (Wilkinson Microwave Anisotropy Probe) space mission and the BICEP2 (Background Imaging of Cosmic Extragalactic Polarization 2) experiment.**

Keywords: cosmic microwave background radiation, cosmology, data analysis

1. Introduction

Major astrophysical results have been obtained in the last decade. Most of them are related to observations by space telescopes in different energy bands and by cosmic ray detectors. The most groundbreaking studies include observations by the WMAP (Wilkinson Microwave Anisotropy Probe) mission by NASA (USA) and the Planck mission by the European Space Agency (ESA), which measured fluctuations of the cosmic microwave background (CMB). Both satellites were launched to a quasi-stable Lagrange L2 point of the Earth–Moon system at a distance of 1.5 mln km from Earth in the direction opposite to the Sun. These space missions enabled measurements of cosmological parameters of our Universe with unprecedented precision.

The WMAP observations[1] were carried out from 2002 until 2011 in five frequency bands: 23 GHz (K-band), 33 GHz (Ka-band), 41 GHz (Q-band), 61 GHz (V-band), and 94 GHz (W-band). Data obtained over 1, 3, 5, 7, and 9 years of the mission operation [1–7] were publicly available through the site referenced in footnote 1. The analysis of time series records, including map-making and pixelization of the sky, as well as the signal decomposition, resulted in information on the anisotropy and polarization of the CMB, foreground components (synchrotron and free–free radiation, dust emission), and the calculation of their power spectra. The WMAP ILC (internal linear combination) map constructed from data combined from different observational channels was smoothed by a Gaussian beam with a 1° angular resolution. A full archive of the raw and processed observa-

O V Verkhodanov Special Astrophysical Observatory,
Russian Academy of Sciences,
369167 Nizhnii Arkhyz, Zelenchukskii rayon, Karachaevo-Cherkesia,
Russian Federation
E-mail: vo@sed.sao.ru

Received 1 August 2015, revised 21 August 2015
Uspekhi Fizicheskikh Nauk **186** (1) 3 – 46 (2016)
DOI: 10.3367/UFNr.0186.201601b.0003
Translated by K A Postnov; edited by A M Semikhatov

---

[1] http://lambda.gsfc.nasa.gov.

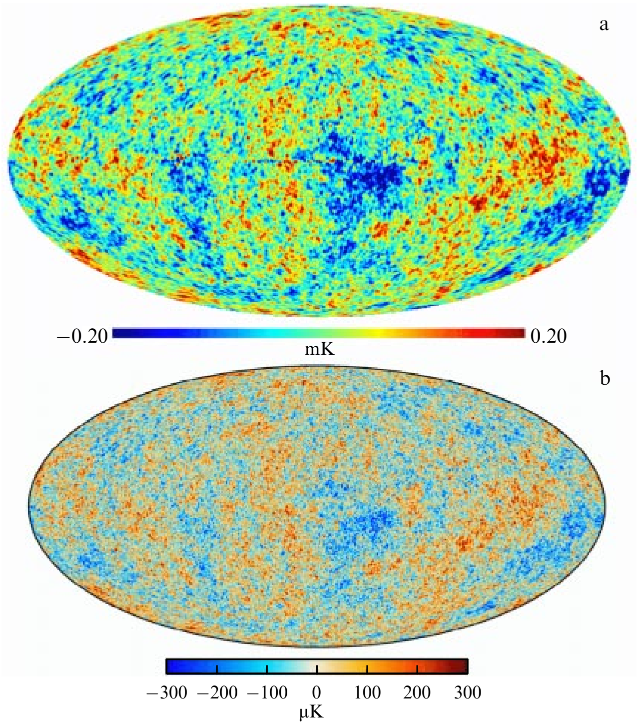

Figure 1. (Color online.) (a) The WMAP9 CMB map (for 9 years of observations) with a resolution of 1°. (b) The Planck 2015 CMB map with a resolution of 5′ (thermodynamic CMB temperature is shown in μK).

tional data is publicly available through the WMAP site. The constructed CMB map and the angular power spectra allowed determination of all cosmological parameters, and good agreement with results of independent measurements was achieved [8].

Independently of the WMAP observations, the ESA designed and launched the Planck mission.[2] Aimed at similar goals, this project is a new-generation experiment, exceeding previous experiments in sensitivity, angular resolution, and the number of frequency bands. Figure 1 shows a map built from the WMAP and Planck CMB sky surveys.

In this review, we consider different stages of information acquisition, including time series analysis, sky map making, pixelization, component separation, angular power spectrum calculation, and cosmological parameter determination. We discuss the main cosmological results of the Planck mission and compare them with the WMAP results.

The main results of the Planck mission are available through the site www.cosmos.esa.int/web/planck/publications in four groups of papers describing the early (27 papers, 2011) and intermediate (38 papers, 2012–2015) Planck results, as well as the Planck results of 2013 (31 papers) and 2015 (28 papers as of the time of writing). Each of these groups is preceded by a short summary of the results obtained in the corresponding time interval. On the same site, a joint paper by the Planck and BICEP2 (Background Imaging of Cosmic Extragalactic Polarization 2) collaborations devoted to the results of observations of the B-mode of CMB polarization is presented, as are 40 technical papers describing operation of the Planck satellite instruments. We note that data analysis is carried out in all of the above papers; in addition, theoretical aspects of the data analysis are considered in 13 papers published before the Planck mission launch (Planck pre-launch papers).

2. Planck satellite instruments

The initial name of the Planck satellite was COBRAS/SAMBA. This is a historical name, because the mission concept arose from two space experiments with similar goals, COBRAS (COsmic Background Radiation Anisotropy Satellite) and SAMBA (SAtellite for Measurement of Background Anisotropies). Both experiments were united in one mission. The mission launch was first planned by the ESA in 1994, and in 1996, upon improving the project, it was included in the ESA's 'Horizon 2000' science program. After that, the mission was renamed after the outstanding German physicist Max Planck (1858–1947). The Planck satellite (Fig. 2) was manufactured at the Cannes Mandelieu space center.

The satellite is equipped with an off-axis Gregory telescope with two parabolic mirrors (Fig. 3). The diameter of the primary and secondary mirrors is 1.9×1.5 m and 1.1×1.0 m. The detectors include 74 radiometers sensitive in the 25–1000 GHz (millimeter and submillimeter waves). Using these detectors, simultaneous sky scanning was performed with an angular resolution from 30′ at low frequencies to 5′ at high frequencies. Cross sections of the detector beams are shown in Figs 4 and 5. The detectors were separated into two groups, which are referred to as the Low Frequency Instrument (LFI), including radiometers centered at 30, 44, and 70 GHz, and the High Frequency Instrument (HFI), including bolometers with central frequencies of 100, 143, 217, 353, 545, and 857 GHz. The LFI employs high-electron-mobility transistors, and the HFI includes 48 bolometric detectors for photon detection. manufactured at the Jet Propulsion Laboratory (JPL) of the California Institute of Technology (Caltech). The receivers were cooled to 17 K by a special cryogenic system. The actual parameters of the LFI and HFI detectors are listed in Tables 1 and 2, according to the Planck collaboration 2015 data [11].

The total mass of the satellite is 1950 kg. The design of the satellite enables all-sky mapping approximately twice per year with a record high combined sensitivity, angular resolution, and frequency coverage. Planck is the ESA's project, with a contribution from NASA. The observatory includes instruments from two science teams financed by ESA countries (led by France and Italy), and telescopes and reflectors that were manufactured through ESA collaboration with a scientific consortium headed by Denmark, which financed the telescope construction.

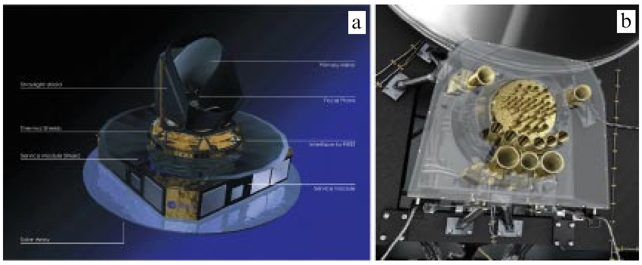

Figure 2. (a) The Planck satellite. (b) Radiometer horns (at frequencies of 30, 44, and 70 GHz) and bolometers (at frequencies of 100, 143, 217, 353, 545, and 857 GHz) in the focal plane of the telescope. (Figure from the site http://www.rssd.esa.int/Planck/.)

---

[2] http://www.esa.int/Planck.

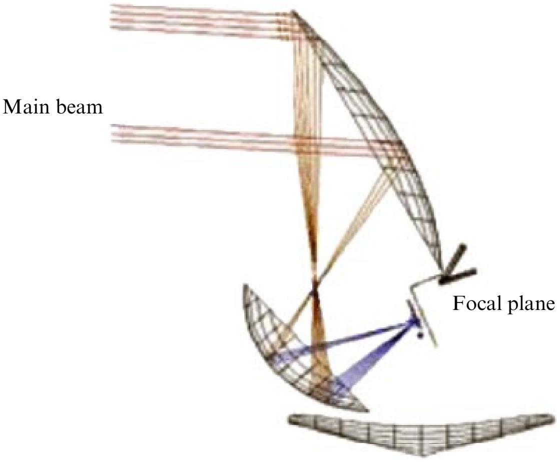

Figure 3. Gregory system of the Planck telescope.

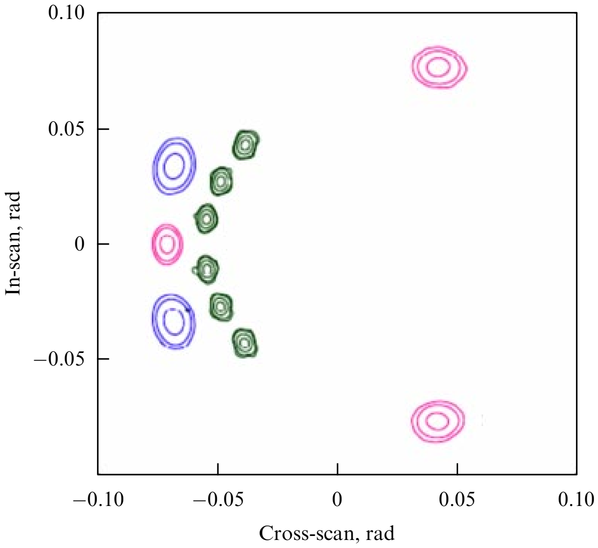

Figure 4. (Color online). Plank LFI beam profiles reconstructed from the first four Jupiter transits. The beams are represented by contours drawn at the levels of −3, −10, −20, and −25 dB from the peak at 70 GHz (green), −3, −10, −20 at 30 GHz (blue), and 44 GHz (pink). (From [9].)

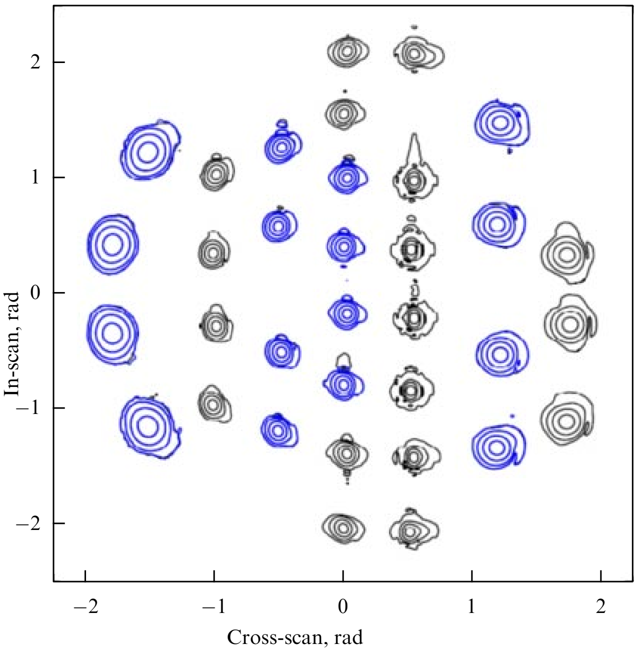

Figure 5. Planck HFI beam profiles reconstructed from transits of Mars, Saturn, and Jupiter during the first three observational runs. The beams are represented by contours drawn at the levels of −3, −10, −20, and −30 dB from the peak. (From [10].)

Table 1. Actual parameters of the LFI instruments on the Planck maps.

Characteristic	Frequency band, GHz		
	30	44	70
Central frequency, GHz	28.4	44.1	70.4
Effective full width at half maximum (FWHM), arc minutes	32.29	27.00	13.21
Effective beam ellipticity	1.32	1.04	1.22
Temperature noise (after one-degree smearing), μK	2.5	2.7	3.5
Polarization noise (after one-degree smearing), μK	3.5	4.0	5.0
Total calibration error, %	0.35	0.26	0.20
Systematic error in the Stokes parameter I, μK	0.19	0.39	0.40
Systematic error in the Stokes parameter Q, μK	0.20	0.23	0.45
Systematic error in the Stokes parameter U, μK	0.40	0.45	0.44

The satellite was launched from the Kuru cosmodrome on 14 May, 2009 by an Arian-5 rocket. The same rocket launched the orbital infrared telescope Herschel. The Planck observatory started surveying the microwave sky on 13 August by orbiting the Lagrange L2 point of the Earth–Moon system 1.5 km from Earth. The mission duration, from launch to switching-off the equipment on 23 October, 2013, was 4 years, 5 months, and 9 days. During this time, the observatory performed five all-sky surveys with both instruments.

The main advantages of the Planck mission over the previous WMAP space mission, which were achieved for some parameters, included:

- better (threefold) angular resolution, which enabled intensity measurements at smaller angular scales (down to 5′);
- higher (tenfold) detector sensitivity;
- observations in nine frequency bands, which allow improving the galactic foreground component separation from the CMB signal.

3. Goals and physics

The main goals of the Planck mission included:

- high-angular-resolution measurements of the intensity and polarization of the primordial CMB anisotropy;
- creation of a catalog of galaxy clusters using the Sunyaev–Zeldovich (SZ) effect;
- observations of gravitational lensing of the CMB due to deflection of photon trajectories passing through matter clusters and of the Sachs–Wolfe effect related to the photon frequency change when passing through galaxy clusters under formation or through expanding voids with a time-variable gravitational potential;
- observations of bright extragalactic sources in active galactic nuclei and infrared sources related to dust-rich galaxies;
- observations of the Milky Way, in particular, the interstellar medium and diffuse synchrotron radiation, as well as measurements of the Galactic magnetic field;

Table 2. Actual parameters of the HFI instrument on the Planck maps.

Characteristic	Frequency band, GHz					
	100	143	217	353	545	857
Number of bolometers	8	11	12	12	3	4
Effective FWHM, arc minutes	9.68	7.30	5.02	4.94	4.83	4.64
Effective beam ellipticity	1.186	1.040	1.169	1.166	1.137	1.336
Noise per beam solid angle, μK	7.5	4.3	8.7	29.7	...	...
kJy sr^{-1}	...	...	...	...	9.1	8.8
Temperature noise, μK grad	1.29	0.55	0.78	2.56	...	...
kJy sr^{-1} rad	...	...	...	...	0.78	0.72
Polarization noise, μK grad	1.96	1.17	1.75	7.31	...	...
Calibration accuracy, %	0.09	0.07	0.16	0.078	1.1(+5%)	1.4(+5%)

- Solar System studies: planets, asteroids, comets, and zodiacal light.

The primary goals of the Planck mission were to measure the CMB temperature and polarization, which were needed to test the standard cosmological model and to improve its parameters.

4. Data analysis

The standard CMB data processing pipeline can be conventionally separated into several stages.

1. Time ordered data (TOD) taking in the form of the radiation temperature as a function of time or sky coordinates, $T(t) = T(l, b)$; the primary data processing.
2. Map-making, including signal reconstruction on the celestial sphere from TOD and data averaging in pixels (pixelization).
3. Separation of the microwave background components: the CMB, galactic foreground components, and extragalactic sources.
4. Map decomposition into spherical harmonics (multipoles) and map reconstruction from the spherical harmonics.
5. Statistical analysis of the map signal.
6. Power spectral analysis and determination of cosmological parameters.

Each stage typically included several thousand simulations of the experiment.

We note several of the most important procedures that we need in discussing the Planck mission results in what follows.

4.1 Harmonic decomposition

The CMB data analysis is usually carried out in two equivalent parameter spaces: in the real pixel space, in which CMB maps are represented on the sky, and in the harmonic domain, in terms of spherical harmonics (or multipoles) in the case of a sphere. The data analysis, component separation, and power spectrum calculation can be performed in any parameter space using different methods to obtain the same results (but the number of operations can be different). Frequently, combined methods are used, which enables separation of specific angular spaces in the harmonic domain and then the analysis of the correspondingly reconstructed maps in the pixel space. These approaches are also used in the Planck data analysis.

The sky map decomposition with respect to the spherical functions (multipoles), denoted as $Y_{\ell,m}(\theta, \phi)$, is determined by the expression

$$\Delta T(\theta, \phi) = \sum_{\ell=2}^{\infty} \sum_{m=-\ell}^{m=\ell} a_{\ell m} Y_{\ell,m}(\theta, \phi) \,. \tag{1}$$

The functions $Y_{\ell,m}$, which are usually written in polar coordinates, depend on two arguments: the polar angle θ, which is related to the latitude b as $\theta = 90^\circ - b$, and the longitude ϕ. The index ℓ of $Y_{\ell,m}$ is the number of the spherical harmonic (multipole) corresponding to the size of hot and cold spots of a given harmonic on the sky (for example, in the case of a dipole, two spots are observed on the celestial sphere; in the case of a quadrupole, four spots are observed; etc.); m is the mode number of the multipole ℓ; the mode reflects how spots with a given size are distributed on the sphere. The sum of all spherical harmonics taken with certain coefficients $a_{\ell,m}$, which reflect the contribution of each harmonic, yields the CMB anisotropy map.

For a continuous real function $\Delta T(x, \phi)$ describing the temperature anisotropy, the contribution from each harmonic to the map, i.e., the decomposition coefficient $a_{\ell m}$, is given by

$$a_{\ell m} = \int_{-1}^{1} \mathrm{d}x \int_{0}^{2\pi} \mathrm{d}\phi \, \Delta T(x, \phi) \, Y^{*}_{\ell m}(x, \phi) \,, \tag{2}$$

where $Y^{*}_{\ell m}$ is the complex conjugate of $Y_{\ell m}$, and $x = \cos\theta$, where θ is the polar angle. Usually, only multipoles that bear cosmological information are analyzed, i.e., those with $\ell \geqslant 2$. We recall that the monopole ($\ell = 0$) shows the mean background temperature, and the dipole ($\ell = 1$) indicates the direction of the Earth motion vector in space. The sky signal decomposition into spherical harmonics is orthogonal, which distinguishes it from the usual polynomial approximation: for example, if we subtract a certain harmonic corresponding to a specific angular scale from the map, the signal on other scales does not change.

Examples of the CMB Planck signal multipole decomposition are shown in Figs 6–8 for standard quadrupole ($\ell = 2, m = 0, 1, 2$) and octupole ($\ell = 3, m = 0, 1, 2, 3$) modes.

4.2 Pixelization and map-making

The recorded temperature series are not yet a CMB map. To build the background map, it is necessary to understand exactly which original signal resulted in the registered response, taking multiple passages of the telescope beam through a given sky field and detector noises into account. This problem reduces to a system of linear equations that also incorporate the rule of sky partitioning into small areas (pixelization) and the radio dish properties, including the beam (solid angle within which the dish receives the signal) and random noise. After stacking multiple observations of chosen fields for a given sky pixelization, a map of the signal can be made. Maps of the registered signal by the Planck satellite at different frequencies are presented in Fig. 9.

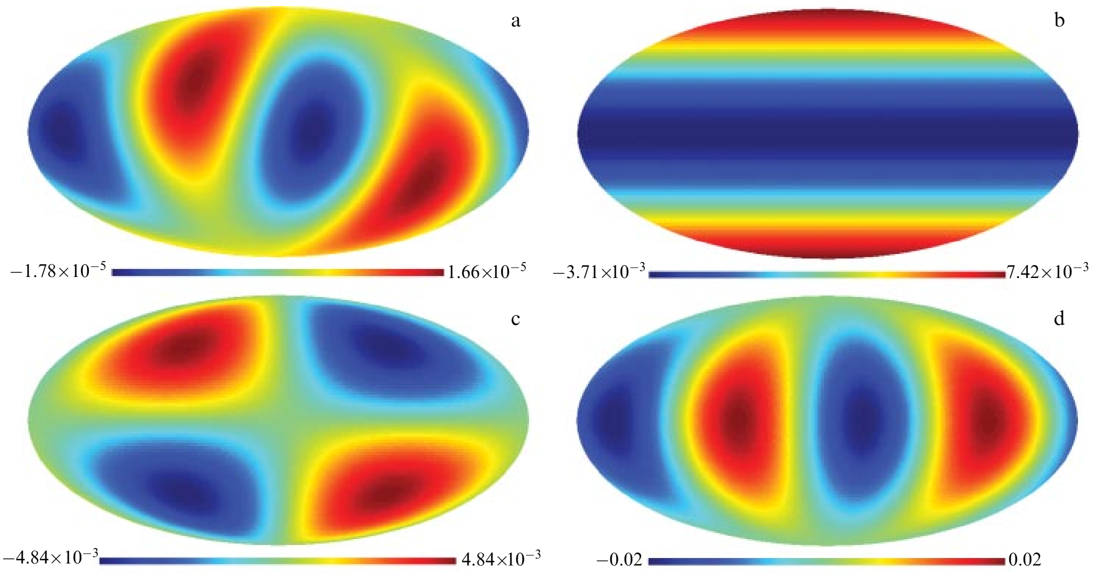

Figure 6. (a) The quadrupole ($\ell = 2$) of the CMB map and its modes (b) Y_{20} (coefficient on the Planck CMB SMICA (Spectral Matching Independent Component Analyses) map $a_{20} = (8.361 \times 10^{-6}, 0)$), (c) Y_{21} ($a_{21} = (-3.638 \times 10^{-6},\ 8.0101 \times 10^{-6})$), and (d) Y_{22} ($a_{22} = (-1.265 \times 10^{-5},\ -1.493 \times 10^{-5})$). The coefficients are shown for the CMB temperature of the Planck SMICA map in kelvins.

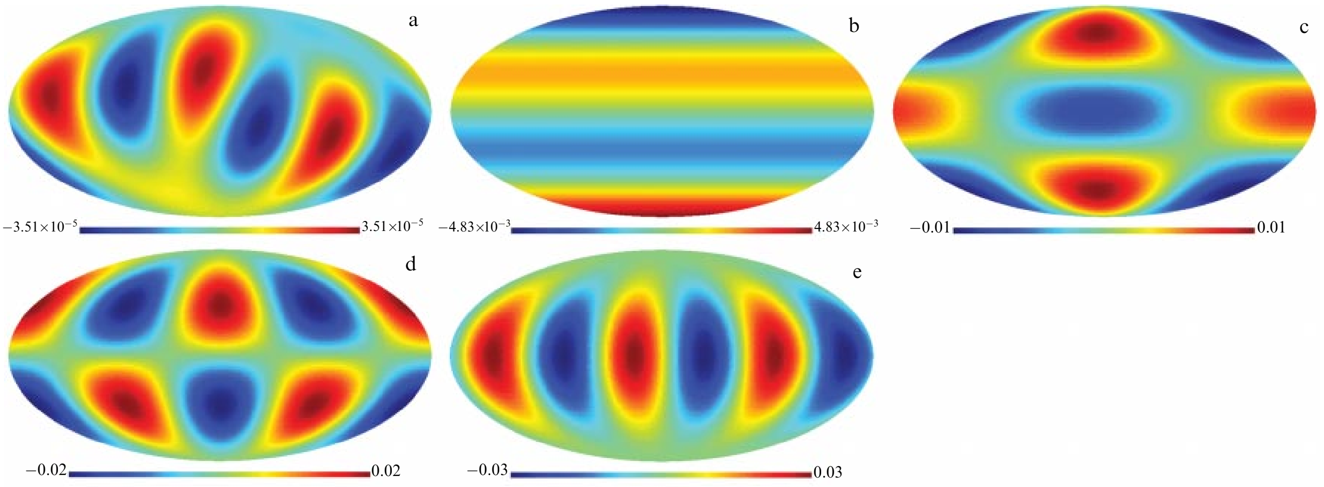

Figure 7. (a) The octupole ($\ell = 3$) of the Planck CMB map (2d 2015 data release) and its modes (b) Y_{30} (coefficient on the CMB map $a_{30} = (-6.261 \times 10^{-6}, 0)$), (c) Y_{31} ($a_{31} = (-8.912 \times 10^{-6},\ 8.715 \times 10^{-7})$), (d) Y_{32} ($a_{32} = (2.172 \times 10^{-5},\ 1.196 \times 10^{-6})$), and (e) Y_{33} ($a_{33} = (-1.401 \times 10^{-5},\ 3.048 \times 10^{-5})$). The coefficients are shown for the CMB temperature of the Planck SMICA map in kelvins.

The sky maps were obtained after processing the corresponding data from receivers working in each frequency band for the entire period of mission duration. The primary data processing took systematic effects into account, including the dipole due to Solar System motion through the CMB and Planck satellite motion in the Solar System. Zodiacal light and side-lobe scattering were also taken into consideration.

The LFI and HFI instruments have fundamentally different types of detectors (radiometers and bolometers, respectively), and therefore different signal registration and noise analysis methods should be applied. Several papers were devoted to the LFI and HFI data analysis for each instrument separately. Parameters describing systematic uncertainties are also somewhat different. We describe the results presented by the Planck collaboration with the corresponding comments. The pipeline of map-mapping from time series (TOD) includes several procedures described in the accompanying papers, which have special names (the names of the software packages). The latter are also mentioned in what follows because most of them are publicly available and can be used to solve similar problems.

4.2.1 Specifics of the LFI data processing. The first standard steps of the input time series processing include cleaning from the 4π-folded dipole with the antenna beam and the scattered light from the Galaxy, obtained by the 4π convolution of the beam side lobes with the model of the Galaxy [12]. The LFI maps are built using the special code Madam [13], in which the destriping technique is realized [14]. The algorithm is aimed at solving the problem of correlated noise observed in the initial Planck data. During each sky scanning cycle, which is determined by the satellite axial rotation for about 1 min and the similar observation of the same sky area for about 44 min before the next pointing, the 1/f-like noise due to instability of the HEMP (High Electron Mobility Transistor)

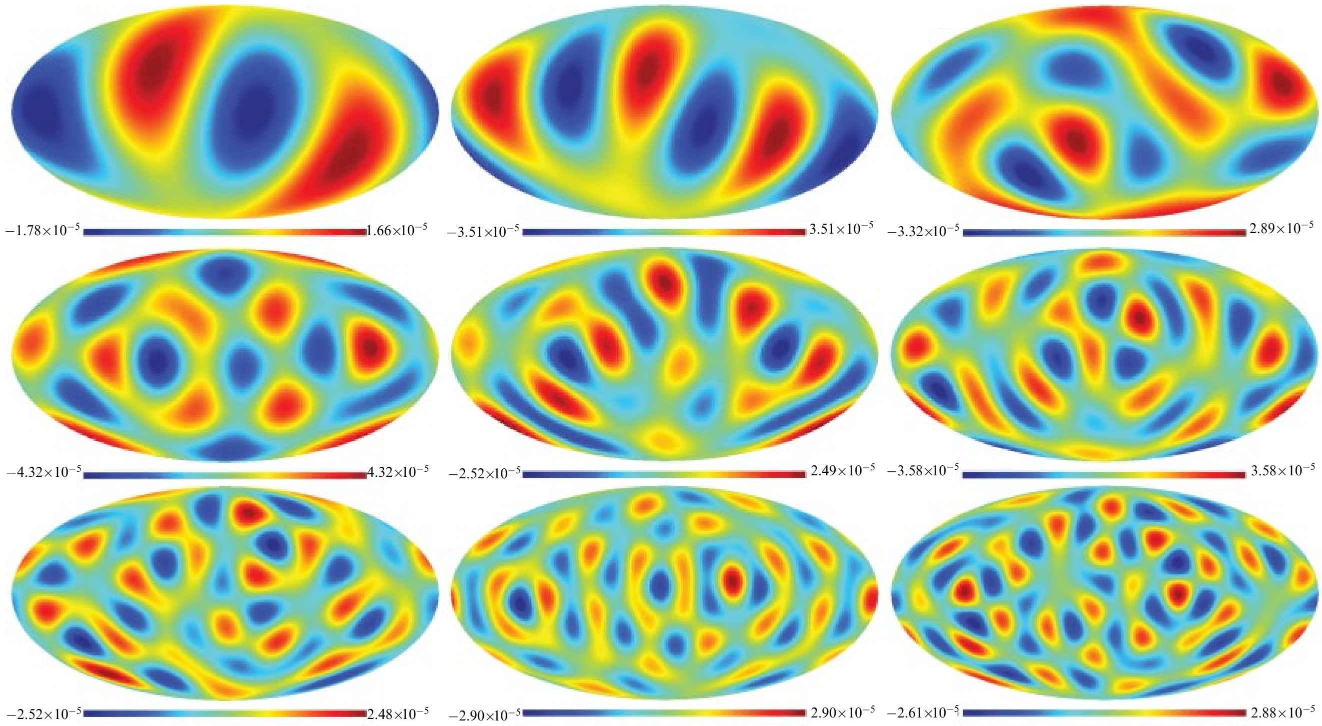

Figure 8. Multipoles ($\ell = 2, 3, 4, 5, 6, 7, 8, 9, 10$) of the Planck CMB map (SMICA).

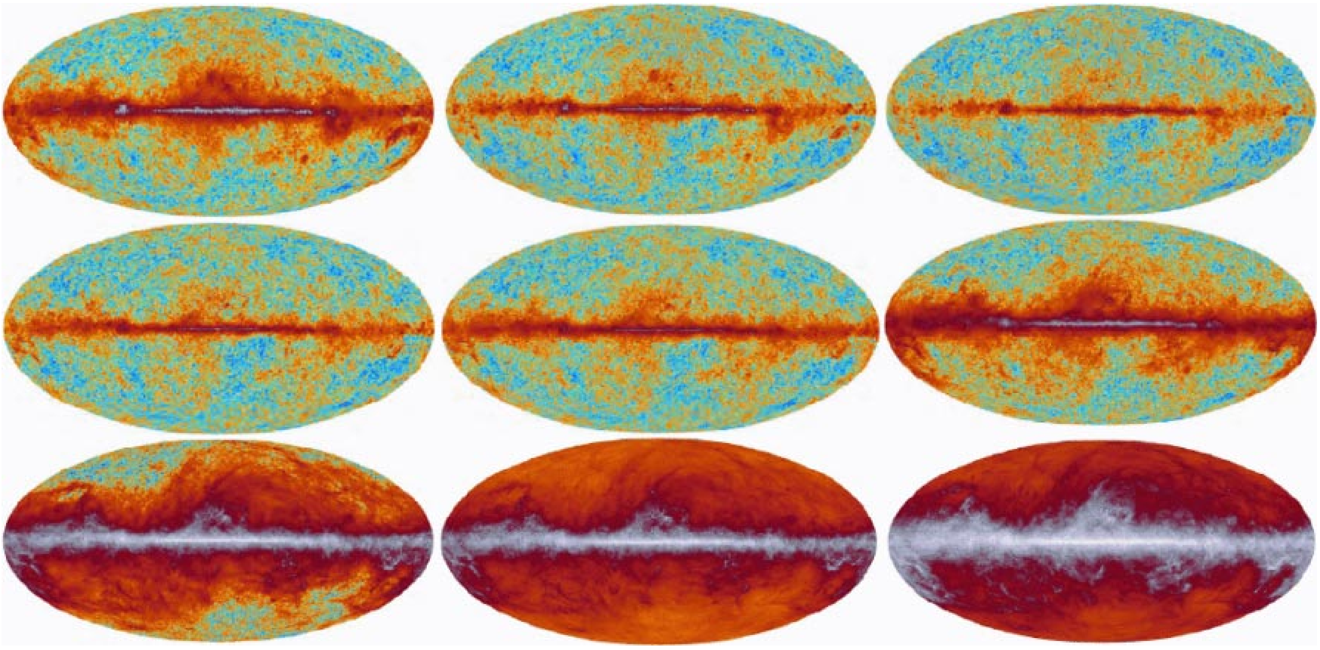

Figure 9. (Color online). Planck all-sky maps at frequencies of 30, 44, 70, 100, 143, 217, 353, 545, and 857 GHz (from left to right, top to bottom).

amplifier persists in the record. After averaging the circle records, passing through one sky area before the next satellite pointing, and cleaning small deviations from the mean value, the 1/f-noise collected during the entire observational cycle remains in the averaged data. After the primary processing, only low-frequency components of this noise survive, which appear as stripes on the final maps reflecting the Planck scan strategy.

To remove such stripes, a destriping method was designed. The algorithm is based on the removal of the correlated noise at constant-duration time intervals called baselines (Fig. 10). A noise filter is constructed on the specified baselines. At low frequencies, 0.25 s and 1 s baselines were used. The radiometer signals were combined with equal weights for each horn to minimize systematic errors. These weights were used in the map-making procedure. A detailed description of this procedure can be found in [13, 15, 16].

We note the main stages of the primary LFI time series processing:

- construction of the LFI instrument model;

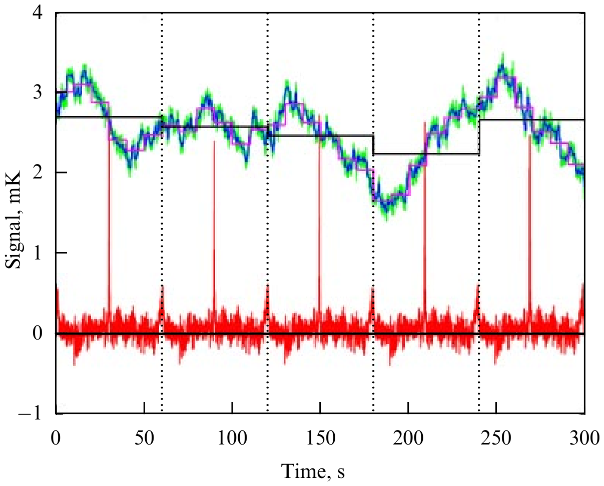

Figure 10. (Color online). Example of the destriping algorithm. A five-minute clip with simulated 1/f noise is fitted with 1 min, 10 s, and 0.625 s baselengths (in black, purple, and blue, respectively). Also shown is the model TOD signal (in red). The vertical dashed lines mark the 1 min scanning intervals. The strong peaks correspond to galactic transits. (From [14].)

- cleaning of nonlinear noises of the analog–digital converter and one-Hertz spikes;
- calculation and application of modulation amplification to minimize the 1/f-noise;
- combination of signals from diodes;
- calculation of the corresponding sky pointing for each detector using additional data and information on the antenna beam (the information includes the current distance to the Sun and temperature of electronics in the radiometer block);
- calibration of the measured signal and transformation to a physical quantity (thermodynamic CMB temperature in kelvins), calculation (fitting) of the total CMB dipole 4π-convoluted with the antenna beam, and taking the galactic scattering features into account;
- cleaning of the signal from solar and orbital dipoles 4π-convoluted with the antenna beam and of the galactic emission 4π-convoluted with the beam side lobes;
- combination of information from time series and its inclusion in the summary product, including sky maps at each frequency.

4.2.2 Specifics of the HFI data processing. The map-making procedure and calibration of the HFI signal are described in detail in [16, 17]. We note the most important steps of the primary data processing.

Telemetric data were converted into time series of measurements from each of the 52 usual bolometers, as well as of two dark bolometers, 16 thermobolometers, and two devices (resistor and capacitor) included in the HFI. The time series data (time-ordered information, TOI) were corrected if noises were detected and removed (for example, due to collision with particles), as well as after the removal of records with an unstable signal during one observational cycle (pointing period) called a ring. The ring record was binned (smoothed in a given window, a bin) according to the sky pixelization HEALPix [18] (see Section 4.2.4). Each ring corresponded to the binned data over one period of observations.

Different standards were used for data calibration at different frequencies. In the range 100–353 GHz, the calibration coefficients were determined by correlating the signal with the orbital dipole that was very precisely calculated from the Planck satellite flight dynamics. The corresponding calibration coefficients were thus derived for each bolometer. At 545 GHz and 857 GHz, the calibration was performed by observations of Uranus and Neptune (Jupiter was excluded because of its high brightness) using their emission models especially constructed for the Planck mission. At these frequencies, one calibration coefficient was used for all rings.

To clean the low-frequency noise, the ring offset was determined by minimizing the signal difference between rings (in the HEALPix pixelization) at their crossing, and then the corresponding noise signal was determined and cleaned by the destriping procedure. Using the zodiacal light model, the corresponding correction was calculated and taken into account in the TOI from calibrated rings. The obtained TOI series were converted into HEALPix maps, where the bolometer data were given weights inversely proportional to the detector noise variation.

We also note some steps to prepare maps for component separation. The preparation stage included:

1) determination of the correction for dust emission leakage using ground-based data;

2) correction of the signal calibration in the beam side lobes: the signal in the frequency bands 100, 143, and 217 GHz was multiplied by the respective factors 1.00087, 1.00046, and 1.00043 to compensate for unremovable side lobes. The corresponding covariance maps were corrected similarly by multiplying by the squares of these factors;

3) Filling of the missed pixels, which were then assigned mean values for nondamaged pixels inside a region with a given radius; for full maps in a frequency channel, this radius was chosen to be 1°.

4.2.3 Map-making procedure. The transformation of primary-processed time series into a sky map is called map making. The procedure is independently applied in each frequency channel and polarization. The map-making methods are somewhat different for LFI and HFI instruments, not only because of different beams in which signal and noise from different receivers are mixed but also because the initial data analysis was performed by different groups inside the Planck collaboration. We use the notation introduced in the corresponding Planck mission publications.

The LFI map making can be described by a system of matrix equations [12, 13, 15, 16]. The full LFI time series data stream can be represented as

$$\mathbf{y} = P\mathbf{m} + F\mathbf{a} + \mathbf{n}\,, \tag{3}$$

where the vector **a** describes the set of baselines used in the destriping technique, F is the matrix that decomposes the baselines in the TOD, the vector **n** represents white noise, and P is the pointing matrix that collects the TOD flux from the sky with a diffuse signal described by **m**. Equation (3) can be used to construct maps for three registered Stokes parameters, I, Q, and U. The *a priori* noise is described by the expected correlation between the baseline amplitudes **a**:

$$C_a = \langle \mathbf{a}\mathbf{a}^{\mathrm{T}} \rangle\,, \tag{4}$$

where T denotes matrix transposition. Preliminary parameters are obtained from noise estimates (frequency, white noise dispersion, and spectral slope). The *a priori* noise characteristics enable the destriping technique to be applied to very short baselines in order to very accurately clean the noise. The final map can be presented as

$$\mathbf{m} = (P^{\mathrm{T}} C_{\mathrm{w}}^{-1} P)^{-1} P^{\mathrm{T}} C_{\mathrm{w}}^{-1} (\mathbf{y} - F\mathbf{a}) \,, \tag{5}$$

where C_{w} is a diagonal weight matrix.

The destriping procedure constructs the sky map by solving a system of equations for different baselines. Then, by binning (smoothing in the pixel window), the final map is produced by removing baselines used previously. This two-step procedure decreases systematic errors to some extent. The procedure is controlled by applying a special mask at the destriping stage, and the map quality is estimated by the error calculated in determining the baseline as the discrepancy between the real and model signals $P\mathbf{m}$. The main signal errors are due to the signal variation inside the pixel, the difference between one-frequency radiometer responses (frequency inconsistency), and the deviation of the model beam from the actual one. The error increases mainly at low galactic latitudes, where the signal gradient is the largest. The Madam code, which implements the destriping technique, produces maps in the HEALPix format [18]. For most low-frequency maps, the resolution parameter is $N_{\mathrm{side}} = 1024$ (the parameter describes the number of pixels on the sphere $N_{\mathrm{tot}} = 12N_{\mathrm{side}}^2$ (see Section 4.2.4)). At 70 GHz, maps with $N_{\mathrm{side}} = 2048$ were also made.

For the HFI data, dipoles modulated by the orbital motion of the satellite and the Solar System motion were also taken into account in the destriping procedure [16, 17]. The orbital dipole with relativistic corrections taken into consideration was also used to calibrate data. The orbital dipole produces yearly modulation. These variations are included in the HFI map-making procedure $\mathbf{P}_t$ (in the notation of the HFI group [17]):

$$\mathbf{P}_t = G \times (A_{tp} \mathbf{T}_p + \mathbf{t}_{\mathrm{orb}} + \Gamma_{tr} \mathbf{o}_r) + \mathbf{n}_t \,, \tag{6}$$

where A_{tp} is the antenna pointing matrix; $\mathbf{t}_{\mathrm{orb}}$ is the time-dependent orbital dipole signal; $\mathbf{T}_p$ is the sky signal measured in the pth pixel that contains information on the solar dipole and Stokes parameters I, Q, and U; Γ_{tr} is the ring-pointing matrix that relates the data set $\mathbf{t}$ to the ring number r; G is the gain coefficient; $\mathbf{o}_r$ is the offset for the rth ring; and $\mathbf{n}_t$ is the noise component. Here, unknowns are G, $\mathbf{o}_r$, and $\mathbf{T}_p$. Due to degeneracy between the average offset and zero level of the maps, $\langle \mathbf{o}_r \rangle = 0$. The zero level of the HFI maps was determined using external datasets from the level of the galactic foreground emission and cosmic infrared background. The value following from the map-making procedure for each pixel is [17]

$$\mathbf{T}_p = (A^{\mathrm{T}} N^{-1} A)^{-1} A^{\mathrm{T}} N^{-1} \mathbf{d} \,, \tag{7}$$

where $\mathbf{d}$ are calibrated, cleaned ring data with offsets and the orbital dipole removed, $\mathbf{d}_t = (\mathbf{P}_t - \Gamma_{tr} \mathbf{o}_r)/G - \mathbf{t}_{\mathrm{orb}}$, and $N = \langle \mathbf{n}^{\mathrm{T}} \mathbf{n} \rangle$ is the covariance noise matrix. To make HFI maps, the polkapix code was used to implement the destriping technique. The output HFI maps at six frequencies (100, 143, 217, 353, 545, 857 GHz) are presented in the HEALPix form [18] with the resolution parameter $N_{\mathrm{side}} = 2048$.

4.2.4 Pixelization. The map-making is performed using a specified sky pixelization grid. This grid is used to further analyze the CMB data, including the harmonic decomposition and inverse map reconstruction, the component separation, and the signal statistic analysis. The pixelization choice is a purely mathematical problem of partitioning a sphere into areas. We note that there are several sky pixelization methods for CMB analysis (see review [19]). These include the Igloo pixelization [20], icosahedron pixelization [21], Hierarchical Equal Area iso-Latitude Pixelization (HEALPix)[3] [18], and Gauss–Legendre Sky Pixelization (GLESP)[4] [22, 23]. In the last case, the pixel centers coincide with nodes of a Gauss-Legendre quadrature. The GLESP pixels have quasi-equal areas and a harmonic decomposition that requires calculating an integral [see Eqn (2)]. The Gauss quadrature with specified nodes provides a very high accuracy of integration. For the HEALPix and GLESP grids, there is special software to work with maps and harmonics. The former is hierarchical, the latter is nonhierarchical and is mainly designed to work with spherical functions and their phases. Comparisons and descriptions of all proposed pixelization methods can be found in review [19].

In the Planck experiment, the HELAPix pixelization was used. HEALPix became the first software package (named after the sphere pixelization method) that implemented the procedure of harmonic decomposition of maps up to high harmonics ($\ell > 100$), the calculation of the angular power spectrum, and sky map visualization. Pixelization was also used to present data in the WMAP experiment [1] and in other CMB experiments [24–27].

The authors of [18] determined three main requirements for the mathematical structure of a discrete grid on the full sky.

1. *Hierarchical database structure*. This requirement is needed for very large databases and was also postulated for a quadrilatericized spherical cube. The simple argument supporting this is that all data elements from an adjacent multi-dimensional space (here, it is a spherical surface) are also neighbors in the tree-like structure of the database. This property facilitates the use of different topological methods for data analysis and enables easy construction of wavelet transforms on triangular and quadratic grids with a fast choice of neighboring pixels.

2. *Equal area of discrete elements*. This requirement is very useful because white noise at a given instrument frequency leads during integration to white noise in the pixel space, and the registered signal is recorded independently of the pixel size. Here, of the course, attention should be given to the choice of the pixel size, which should be sufficiently small compared to the instrumental resolution to avoid excessive signal smearing and the dependence on the pixel shape.

3. *Distribution of pixels in one row along one latitude circle*. Such a pixel distribution is significant for ensuring a high speed of calculation of spherical harmonics. Because the associated Legendre polynomials are calculated via slow recursions, the deviation of the grid nodes from one latitude circle leads to significant time losses upon increasing the number of points processed.

The base resolution in HEALPix is determined by 12 pixels (or sides) on three rings around the poles and the equator. The next hierarchy level is produced from the previous one by splitting each pixel of the preceding level into four equal pixels. Hence, the resolution is determined by

---

[3] http://healpix.jpl.nasa.gov.

[4] http://www.glesp.nbi.dk.

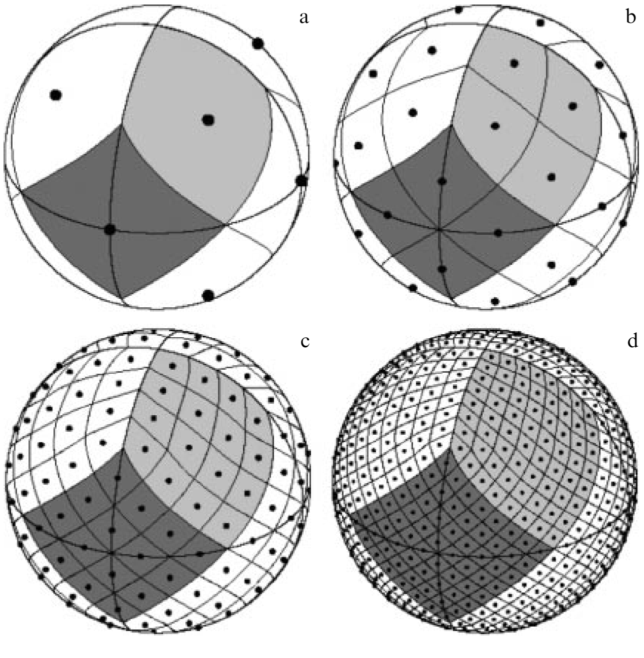

Figure 11. Orthographic view of the HEALPix partition of the sphere. The superimposed of equators and meridians illustrate the octahedral symmetry of HEALPix. The lowest resolution corresponds to 12 basic pixels (a). The sphere is hierarchically partitioned into curvilinear quadrangles. The light gray shading shows one of the 8 (4 north and 4 south) identical polar base-resolution pixels. Dark gray shading shows one of the 4 identical equatorial base-resolution pixels. The resolution of the mosaic increases in subdividing each pixel into four new ones. The grid resolution increases from the base level in three steps. The resolution is characterized by the grid resolution parameter N_{side} (equal to 1, 2, 4, 8 here), which determines the total number of pixels $N_{\text{pix}} = 12N_{\text{side}}^2$, and the sphere in this example is subdivided into (a) 12, (b) 48, (c) 192, and (d) 768 pixels. The areas of all pixels with a given resolution are identical. The pixel centers are located on constant-latitude rings, which is important for the harmonic analysis and spherical harmonic calculations. (The figure is reproduced from [18].)

the parameter N_{side} (Fig. 11) that gives the number of the base pixel splittings. This parameter is used to choose a given map resolution as defined, for example, by the antenna beam. All isolateral rings are located between the top and bottom vertices of equatorial faces (i.e., $-2/3 < \cos\theta_* < 2/3$) or in the equatorial zone. After partitioning into an equal number of pixels, we have $N_{\text{eq}} = 4N_{\text{side}}$. The remaining rings located inside the polar caps ($|\cos\theta_*| > 2/3$) contain a variable number of pixels, which increases from ring to ring with increasing the distance from the pole to one pixel in each square. Thus, a HEALPix map has $N_{\text{pix}} = 12N_{\text{side}}^2$ pixels with the equal area $\Omega_{\text{pix}} = \pi/(3N_{\text{side}}^2)$.

4.3 Separation of components

The next stage after map-making is the extraction of the CMB signal. In addition to the CMB, the Planck signal contains the galactic diffusion component, the extragalactic background, and galactic and extragalactic radio sources. One of the standard methods of the full CMB signal reconstruction is a combination of observational data at different frequencies multiplied by some factors that remove the galactic signal and extract the CMB radiation. This method of component separation was used by the WMAP collaboration [4] (also see [28]). The method is based on the idea that the spectra of the galactic components (namely, synchrotron radiation, free–free emission, and dust emission) are different from the CMB spectrum. Because the combination of channels in the WMAP mission was used without involving external experimental data, the method was named the Internal Linear Combination (ILC), and the sky map produced by this method is accordingly called the ILC map. The coefficients can be determined by minimizing dispersion in the resulting map, with their sum equal to unity in order to preserve the general normalization of the CMB signal. We note that there are many various methods of component separation (see, e.g., [29–36]), which on average give similar results.

In the Planck experiment, four methods were used by different groups inside the collaboration: the Commander-Ruler (C-R) method for the 2013 data release [37], which was later transformed into the extended Commander method for the 2015 data release [38]; internal linear combination in the space of special spherical wavelets — needlets (NILC); template fitting using data at different frequencies to estimate the CMB power spectrum by the expectation maximization algorithm (Spectral Estimation Via Expectation Maximization — SEVEM), and the method realized in the spherical harmonic domain of amplitude matching of the CMB spectral parameters and background components (Spectral Matching Independent Component Analysis, SMICA). These four methods can be separated into two groups. The first includes NILC and SEVEM, where the foreground components are assumed to correspond to specified spectral templates and the CMB is represented by a black-body component, and the CMB variation minimum is sought. The methods of the second group (Commander and SMICA) are based on parametric modeling of the foreground components.

In the Commander method, a Bayesian separation of components in the pixel space by matching a parametric model with data using an *a posteriori* distribution of parameters of model foregrounds is implemented. The fitting is made in two stages. At the first stage, both foreground component amplitudes and spectral parameters are calculated from low-resolution maps by the Markov chain Monte Carlo (MCMC) method using the Gibbs algorithm [39, 40]. At the second stage, the amplitudes are recalculated for high-resolution maps by solving the corresponding system of equations by the generalized least square system method (GLSS) for each pixel with spectral parameters obtained in solving for low-resolution signals at the first stage. The data model $\mathbf{d}_\nu$ at a frequency ν is expressed as a linear combination of N_{c} astrophysical components with instrumental noise added:

$$\mathbf{d}_\nu = \sum_{i=1}^{N_{\text{c}}} F_\nu^i(\theta)\,\mathbf{A}^i + \mathbf{n}_\nu\,, \tag{8}$$

where $\mathbf{A}^i$ is the data vector describing the sky map and containing the ith component amplitude, reduced to the observed frequency, and $F_\nu^i(\theta^i)$ is a diagonal matrix describing the spectral emission of the ith component as a function of the frequency, depending on a small set of spectral parameters θ. The CMB signal is included in the sum of the components and can be represented in the harmonic or pixel spaces. This depends on the purpose of the analysis: the CMB power spectrum calculation or the component separation [37]. The Bayesian theorem determines the *a posteriori* distribution of the model parameters:

$$P(\mathbf{A}^i, \theta|\,\mathbf{d}) \propto \mathfrak{L}(\mathbf{A}^i, \theta)\,P(\mathbf{A}^i, \theta)\,, \tag{9}$$

where $\mathfrak{L}(\mathbf{A}^i, \theta)$ is the Gaussian likelihood function, and the *a priori* function $P(\mathbf{A}^i, \theta)$ depends on the method of accounting for the foreground components. This approach results in a dataset obtained from the *a posteriori* distribution, which is different from direct estimates of each component amplitude and spectral parameters. We note that the Commander procedure is applied to data taken by one detector or a set of detectors, and not to full sky maps at a given frequency. Also, part of the input data from detectors with significant systematic errors is excluded. In addition, the WMAP nine-year data [7] and maps at 408 MHz [41] are included in the analysis. Thus, the input data for the Commander procedure differ from those used by other methods.

The NILC [37] method is a method for extracting the CMB signal (or another component with known spectral behavior) from the original map using the internal linear combination technique applied to multi-frequency observations in the space of special spherical wavelets, needlets. The needlets are taken with weights that can be varied over the whole sky (depending on the coordinates) and for all multipoles (depending on the angular scale). The possibility of taking linear combinations of input maps, which can be varied over the sky and the multipoles, is referred to as localization. In the needlet domain, the harmonic localization is realized by determining the sky areas for each scale. The harmonic localization in the implemented procedure uses spectral bands covering multipoles up to $\ell = 3200$.

The space localization depends on the scale. At large scales, which include low multipoles, only one localization zone was used, whereas at small scales (high multipoles), the sky was partitioned into 20 zones. The NILC method calculates a linear combination in each zone for each scale, by enabling the ILC weights to be naturally adjusted to the variable power of other components as a function of the multipole and location.

A detailed description of the NILC method can be found in [42]. The actually realized method differs from that described in [42] in processing large scales. Because there is no NILC filter for low multipoles, the simple NILC map is equivalent to the ILC map in the pixel space for all multipoles in this range. This procedure is very sensitive to an offset in the signal estimate (the Bayesian offset) in the ILC due to random correlations between the CMB and foreground components. To decrease this effect, the covariance matrix determining the ILC coefficients on large scales is not calculated in the pixel space but is estimated in the harmonic domain as the average of spherical harmonic coefficients with weights that balance the CMB modes. This decreases errors on large scales.

Another algorithm, SEVEM, produces CMB maps at several frequencies using template fitting of foreground components. The method estimates the power spectrum of cleaned CMB maps and data at several frequencies using the expectation minimization algorithm, which is used in mathematical statistics to find maximum-likelihood estimates of probabilistic models when the model depends on some hidden variables [43]. Based on the CMB power spectrum, a CMB map is built using a multi-frequency Wiener filter. The method implemented used CMB maps made from data grouped into different frequency channels. The final map was obtained by combining these maps made in each group. Internal templates, i.e., those constructed from the Planck measurements without an external dataset, which usually complicates the analysis and can result in inconsistencies, were used for the map cleaning. The cleaning did not require assumptions on the spectral shape of the foreground components or noise, because the CMB separation technique is very stable [37]. The templates were constructed by subtracting two maps at close Planck frequencies, fitting them to an equal angular resolution, and testing the correctness of the CMB signal removal. The linear combination of templates t_j was subtracted from the input map d to make the CMB map at a given frequency. This can be done both in the pixel space and in the wavelet domain (scale by scale):

$$T_{\mathrm{c}}(x, \nu) = d(x, \nu) - \sum_{j=1}^{n_{\mathrm{t}}} \alpha_j t_j(x)\,, \tag{10}$$

where n_{t} is the number of templates. If the map cleaning is performed in the pixel space, the coefficients α_j are calculated by minimizing variations on the clean map T_{c} outside the masked region. In the wavelet domain, the cleaning is performed in the same way, but independently for each scale, i.e., the linear coefficients depend on the map resolution. Although contaminated fields of the map are excluded by minimizing the variation, they are nevertheless used to calculate the difference, and thus the map covers the entire sky. Here, the residual foreground signal can be observed in the excluded areas. Because the method is linear, it can easily transfer the noise properties to the final CMB map. The method is realized with a fast calculation algorithm allowing several thousand simulations for studying statistical properties, in particular, for cosmological applications.

The SMICA spectral matching method reconstructs the CMB map using a linear combination in the harmonic domain from N_{chan} maps at different frequencies with the weights depending on the multipole number ℓ. With a given set of $N_{\mathrm{chan}} \times \mathbf{x}_{\ell m}$ spherical harmonic coefficients for input maps, the coefficients $\hat{s}_{\ell m}$ of the CMB maps can be calculated as

$$\hat{s}_{\ell m} = \mathbf{w}_\ell^{\mathrm{T}} \mathbf{x}_{\ell m}\,, \tag{11}$$

where the vector $\mathbf{w}_\ell$ with N_{chan} components containing weights depending on the multipole number is chosen by minimizing the CMB variation:

$$\mathbf{w}_\ell = \frac{C_\ell^{-1}\mathbf{a}}{\mathbf{a}^{\mathrm{T}} C_\ell^{-1} \mathbf{a}}\,. \tag{12}$$

Here, $\mathbf{a}$ is the CMB spectrum calculated in each channel and C_ℓ is the $N_{\mathrm{c}} \times N_{\mathrm{chan}}$ spectral covariance matrix for $\mathbf{x}_{\ell m}$. Taking C_ℓ in the form of a simple covariance matrix of observations,

$$\hat{C}_\ell = \frac{1}{2\ell + 1} \sum_m \mathbf{x}_{\ell m} \mathbf{x}_{\ell m}^{\mathrm{T}}\,, \tag{13}$$

it is possible to obtain an ILC map similar to that obtained in [30]. The data in this method are modeled as a superposition of the CMB, noise, and foreground components. The last of these is not modeled parametrically but is represented as the total foreground emission components d in the form of templates with arbitrary spectra, angular spectra, and correlations. In the spectral domain, this is equivalent to the covariance matrices

$$\hat{C}_\ell = \mathbf{a}^{\mathrm{T}} \mathbf{a} C_\ell + A P_\ell A^{\mathrm{T}} + N_\ell\,, \tag{14}$$

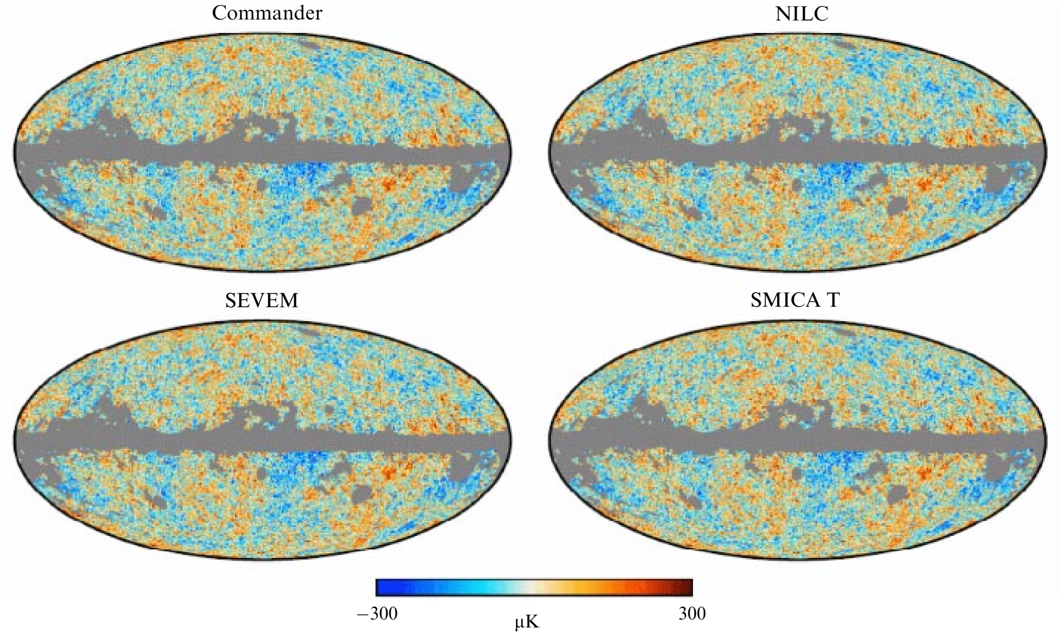

Figure 12. (Color online.) Planck CMB maps reconstructed by different methods: Commander, NILC, SEVEM, and SMICA. The resolution is FWHM $= 5'$, and $N_{\mathrm{side}} = 2048$. The maps are masked. (From [38].)

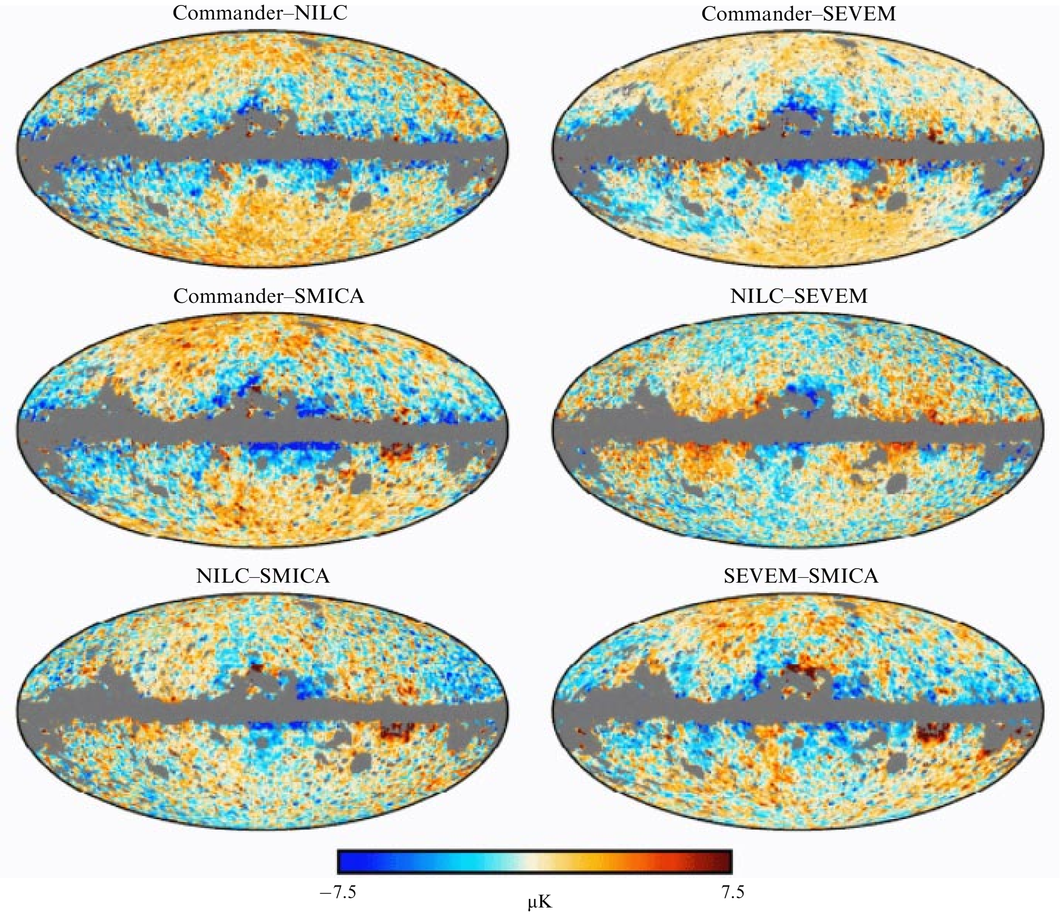

Figure 13. (Color online.) Difference maps between Planck CMB maps reconstructed by different methods: Commander, NILC, SEVEM, and SMICA. The maps are smeared down to resolution with FWHM $= 80'$, $N_{\mathrm{side}} = 128$. The maps are masked. (From [38].)

where C_ℓ is the CMB angular power spectrum, A is an $N_{\mathrm{chan}} \times d$ matrix, P_ℓ is a positive definite $d \times d$ matrix, and N_ℓ is a diagonal matrix representing the noise and data power spectra.

Maps of CMB fluctuations made by different means are shown in Fig. 12. At first glance, no significant differences in the maps can be seen outside the mask. The differences among the reconstructed maps are presented in Fig. 13.

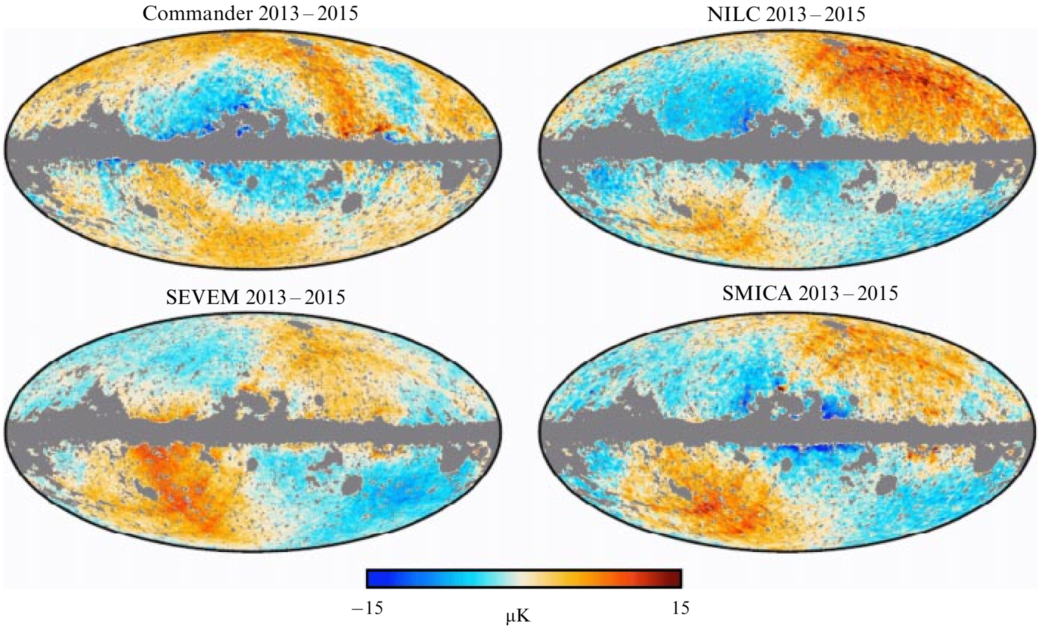

Figure 14. (Color online.) Difference maps between Planck CMB maps reconstructed from different data releases (2013 and 2015) by different methods: Commander, NILC, SEVEM, and SMICA. The maps are smeared down to resolution with FWHM $= 80'$, $N_{\text{side}} = 128$. The maps are masked. (From [38].)

The difference between 2013 and 2015 maps is shown in Fig. 14. Most of the observed differences are due to residuals caused by systematic errors in the CMB signal reconstruction [37]. For the Commander method, the most prominent are large-scale areas with peak-to-peak amplitudes of about 10 μK; the presence of such fields, in fact, reflects the scan strategy of the Planck mission. The difference among the CMB maps made by the Commander method for different data releases demonstrates an excess noise signal that was removed in the 2015 data. Here, two effects can be seen: destriping errors due to different bands for different detectors and side-lobe contamination [17, 44]. For the other three reconstructed CMB maps, the residuals between the signal sky distributions constructed in different years are close to each other but greatly differ from the Commander maps. The main feature of the maps include the quadrupole at a level of 5 μK aligned with the CMB dipole due to the Solar System motion (at the galactic coordinates $(l, b) = (264°, 48°)$) [11], and stripes reflecting the contribution from zodiacal light. Residuals of the first type occur because, during the 2013 HFI data processing, the relativistic Doppler quadrupole ~ 6 μK was not subtracted, but it was taken into account in the 2015 data. Residuals of the second type are due to taking the zodiacal light into account in the improved map-making procedure applied for the 2015 maps [17, 45].

As noted in [38], among all maps, the SMICA map has the lowest temperature power excess at high multipoles caused by the contribution from noncleaned sources. The excess has an almost flat spectrum for multipoles in the range from $\ell \approx 1200$ to 1700, by reflecting the frequency weighting in the harmonic multipole domain. Therefore, effectively taking the source contribution into account is more complicated. For this, a special signal modeling in the full focal plane (FFP) was used in the FFP8 run, where templates with extragalactic sources as a function of multipoles were used for each method. Possible residuals caused by the unknown frequency dependence of the emission intensity of real sources lead to an ℓ-dependent error in the NILC, SEVEM, and SMICA methods. The Commander method can be more stable to this particular effect because it involves the fitting of all maps to a common angular resolution prior to the component separation procedure. However, this stability leads to an overestimation of the source amplitudes.

4.4 Foreground components

Component separation resulted in maps of the galactic and extragalactic microwave foregrounds. The standard components of microwave emission are discussed in Section 5. Spectral coefficients are calculated for these components at each observable frequency. The main components [44] include synchrotron radiation, free–free emission, spinning dust emission and thermal dust radiation, and emission in lines: transitions $J \to 1-0$, $J \to 2-1$, and $J \to 3-2$ in CO molecules. The contribution from gas in galaxy clusters due to the Sunyaev–Zeldovich effect is calculated separately.

4.4.1 Foreground components in temperature maps. Diffuse *synchrotron* radiation is generated by relativistic electrons spiraling along galactic magnetic field lines. The radiation is highly polarized. The polarized component fraction reaches 75% (see the polarization map of synchrotron radiation at the frequency of 30 GHz in Fig. 15 in Section 4.4.2). Theoretical models and observational data suggest that synchrotron radiation is closely approximated by a power law with the exponent $\beta_{\text{s}} \approx -3$ at frequencies above 20 GHz, but becomes flatter at lower frequencies. A one-parameter model is used to determine the synchrotron spectrum, with the parameter relating the signal ratio at the frequency 480 MHz and higher frequencies.

Free–free (*or bremsstrahlung*) *radiation* is due to collisions of electrons with ions, and hence has a specific frequency dependence. The intensity distribution in this case is described by a model with two free parameters: the emission measure (integral of the electron density squared

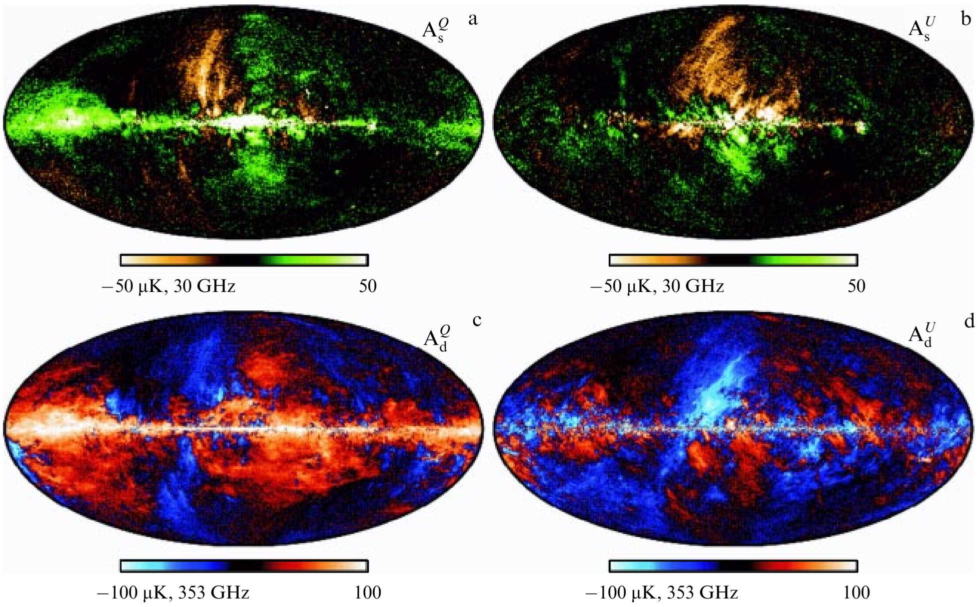

Figure 15. Planck maps of the foreground polarization components: (a, b) synchrotron radiation at 30 GHz and (c, d) dust emission at 363 GHz. Maps (a, c) show the Stokes parameter Q; maps (b, d) show the Stokes parameter U. (From [11].)

along the line of sight) and the electron temperature. At low frequencies, galactic free–free emission is thoroughly mixed with synchrotron radiation, but due to its flatter spectrum it can be recovered from the HFI data with a high signal-to-noise ratio.

At frequencies above 100 GHz, dust thermal radiation dominates [46–49]. The main emission frequency is determined by the temperature of dust particles, and therefore it changes depending on the type of dust and its surroundings. In the ideal case, thermal dust emission at the Planck mission frequencies can be described by a black-body spectrum with two free parameters: the radiation index d and the dust temperature T_{d} per pixel [37, 48]. At frequencies above 857 GHz (towards the COBE–DIRBE (Cosmic Background Explorer — Diffuse Infrared Background Experiment) range), the physical properties of dust grains become more complex; moreover, accounting for systematic instrumental errors becomes more difficult. This justifies the analysis of the dust spectrum only below 857 GHz.

When dust rotates, its grains not only spin but also oscillate (vibrate). If the dust grains have a nonzero electric dipole moment, this motion necessarily produces microwave emission [50]. Progress in observational methods [51–54] has allowed separating this emission component and describing it by the corresponding spectral template calculated for a cold neutral medium [55, 56]. The template has one free parameter: the peak frequency ν_{p}, like the free parameter for synchrotron radiation, which allows performing stable calculations in the parameter space $\log\nu - \log S$, where S is the radiation flux density. With such a two-parameter description [7], numerous versions of spinning dust models can be taken into account with high accuracy.

Emission in CO *lines* and at 94/100 GHz according to the Planck data [57] is reliably measured at 100, 217, and 353 GHz. For CO rotational transitions $J \to 1-0$, $J \to 2-1$, and $J \to 3-2$, special maps are made. Several other lines (CN, HCO$^+$, CS, etc.) also contribute at the 5%–10% level each. Because neither velocity effects nor the physics of clouds (transparency, local thermodynamic equilibrium, etc.) were taken into account during the component separation, CO signal scattering is present in the maps. This is why such a special map was called ‘line emission at 94/100 GHz’ in [57]. Parametrically, the line emission is described in terms of the signal amplitude at the line frequency $a(p)$ normalized to the signal amplitude in a specific detector at a fixed frequency. The amplitude $a(p)$ serves as a scale for h_{ij} constructed in the line ratio space, where the index i encodes the spectral line number and the index j corresponds to the detector number.

The last astrophysical component that was taken into account in the CMB temperature analysis is related to nearby galaxy clusters, from which a strong thermal Sunyaev–Zeldovich (SZ) effect is observed. This effect is due to the CMB photon scattering by hot electrons in galaxy clusters [58]. As a result, the effective spectrum deviates from the black-body spectrum. The only free parameter is the Comptonization parameter y_{SZ}, which is used as a simple amplitude. The microwave spectrum observed from a galaxy cluster due to the SZ effect leads to a negative signal at frequencies 30–143 GHz and to a positive excess at frequencies above 217 GHz. This is a unique feature of the thermal SZ effect, which allows separating it from other foreground fluctuations. Because the effect is weak, it can be registered for the brightest galaxy clusters only. For dimmer objects, the y_{SZ} map becomes sensitive to both model parameters and systematic errors. During the component separation, the authors of [44] applied this method only for two individual sky fields near the Coma and Virgo clusters, where the amplitude of the effect is maximal and can be mixed with other foregrounds. The SZ decrement for the Coma cluster is about −400 μK at frequencies up to 100 GHz at angular scales of several arc minutes [59], and for the Virgo cluster, the effect is several tens of μK at the scales of a few degrees [60], whereas for other objects its amplitude is below several μK for a comparatively wide beam. The SZ signal extraction across the entire sky is discussed in [61].

For each channel (frequency), the monopole and dipole were taken into account. For example, the primordial monopoles include the CMB monopole with a temperature of 2.7255 K and the cosmic infrared background monopole [62]. The CMB mainly contributes to the dipole; the dipole temperature amplitude is 3365.5 μK from the LFI data and 3364.0 μK from the HFI data. The difference between the LFI and HFI dipoles, 1.5 μK, is within the admissible error [11]. In the ideal case, the dipole contribution is already removed at the map-making stage [12, 17], but due to a nonzero error in its determination and the difference in dipoles used in the Planck and WMAP data, it should be taken into account separately for each map.

4.4.2 Polarization of the foreground components. Three main components are separated in the polarized microwave emission: the proper CMB and the brightest foregrounds, synchrotron radiation and thermal dust emission. Figure 15 shows polarization maps of these components at frequencies of 30 and 353 GHz.

The CMB polarization is caused by Thomson scattering on electrons, which leads to internal polarization. If the incident radiation is fully isotropic, there is no pure polarization in the scattered radiation. But if there is a local quadrupole in the incident radiation, the CMB signal has a nonzero polarization component [63, 64]. Thus, any process that forms quadrupole structures during the recombination epoch would give rise to a CMB polarization. Scalar fluctuations responsible for the CMB anisotropy produce the so-called E-mode — the scalar polarization component in which the polarization direction is either orthogonal or parallel to the wave vector. Primordial gravitational waves from inflation and gravitational lensing of the E-mode produce the so-called B-mode of polarization (the pseudoscalar component), in which the polarization is turned by $-45°$ or $+45°$ to the wave propagation vector.

The synchrotron radiation mechanism in a fully regular magnetic field in the electron motion plane generates power seven times as large as in the orthogonal direction. Here, the polarization can be as high as 70% [65], although it is much smaller for real fields. In addition, the WMAP data revealed that the fraction of the detected polarized emission is about 3% inside the galactic plane and about 20% at high galactic latitudes [66]. Other data suggest that the fraction of polarized galactic emission can be as high as 40–50% [67, 68]. The Planck measurements at 40 and 44 GHz complement these results and allow making independent estimates [69].

The thermal dust effects arise in the galactic magnetic field. Magnetic field acts on asymmetric dust particles by aligning their longer axes along the field direction. The alignment generates emission and additionally contributes to the polarized component in the dust thermal spectrum. The frequency coverage in the Planck HFI channels allows estimating this contribution with high accuracy, which is discussed in [70–75].

Other polarized components (for example, spinning dust particles or polarized CO line emission) contribute at the level of $\sim 11\%$.

4.5 Masks

Separating the galactic diffuse component and the source (galactic and extragalactic) component involves masks — binary maps showing which part of the sky should be screened, i.e., excluded from the data analysis (Fig. 16). The mask construction takes the complexity of the contaminating signal and its level with respect to the CMB into account (Fig. 16). Due to the specifics of the methods and their dependence on the spectral features of the masked signal, the masks are different for different cleaning methods and different frequencies. By combining masks used for different methods and screening different sky areas, standard masks for the Planck data analysis were constructed. The first mask for the temperature anisotropy analysis combines masks used in the Commander, SEVEM, and SMICA methods. The NILC mask is not included because it screens a much smaller sky area. The joined mask has the nonscreened sky area (the percent of the total sky area) $f_{\rm sky} = 77.6\%$. This mask, called UT78, is preferred for the analysis of temperature maps (Fig. 16a). Its extended version, UT76, which is constructed by adding pixels with temperature deviations from the mean of more than 10 K, has $f_{\rm sky} = 76.1\%$. In addition, the FFP8-UT74 mask with $f_{\rm sky} = 73.5\%$ is available, which was designed to work with simulations of the experiment (e.g., in FFP8 simulations).

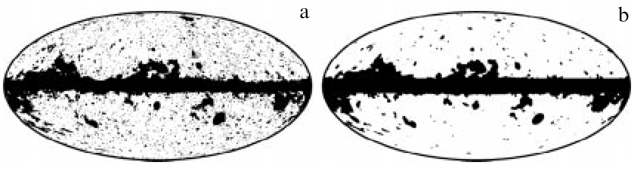

Figure 16. Preferable masks for the analysis of (a) the CMB temperature and (b) polarization maps reconstructed by the component separation methods.

For polarization, as for temperature, standard masks are constructed by combining screened zones used in the Commander, SEVEM, and SMICA methods. The UP78 mask has the working area $f_{\rm sky} = 77.6\%$. In spite of the large coverage, a statistical analysis of screened polarization maps suggests the presence of contaminating point-like sources [38] when applying the Commander, NILC, and SMICA masks. The SEVEM procedure is free from this problem, because the brightest point-like sources are removed in this method. Thus, two versions of the next polarization mask were constructed. The first (UPA77) includes additional pixels in which the signal exceeds the CMB intensity averaged in Q and U modes by 4 K. This mask has the working area $f_{\rm sky} = 76.7\%$. The second mask (UPB77), with $f_{\rm sky} = 77.4\%$, excludes regions of polarized point-like sources discovered in each frequency channel from the combination of masks used in different component separation methods (Fig. 16b). This mask is considered preferential in map analysis because it is more physically justified. There are additional masks constructed as a result of simulations: FFP8-UP76 with $f_{\rm sky} = 76.3\%$ and FFP8-UPA76 with excluded polarized sources and $f_{\rm sky} = 75.7\%$.

5. Astrophysics

The main results can be classified according to the announced tasks of the Planck mission. The most important results, in our opinion, were obtained in the CMB studies, which were the primary purpose of the mission. However, we start with astrophysical papers, which we mentioned in the Introduction, devoted to intermediate results of the mission (2012–2015) and the results of 2013.

5.1 Solar System studies

Millimeter and submillimeter emission is detected from various Solar System objects: planets, small bodies and interplanetary dust (IPD). The Planck satellite also detected this emission. It can be effectively separated from the galactic foreground and other foregrounds because each region of the Solar System was observed by the Planck satellite many times from different positions and with different cross sections of IPD. As early as the COBE mission operation, a model of zodiacal light was constructed, which was checked and used in the data analysis of the multi-frequency Planck maps. The model includes a diffuse cloud, three dust asteroid belts, a circumsolar ring, and dust behind Earth. As expected from the previous analysis, the emissivity of the zodiacal diffuse cloud decreases with increasing the wavelength [47]. At the same time, the emissivity of the asteroid dust stripes decreases more slowly, which implies somewhat different properties of dust granules in these belts. We note that this study is from the third cycle (2013) of the Planck collaboration results.

One of the main conclusions of the zodiacal light emission study suggests that the level of zodiacal light contamination in the CMB analysis is insignificant. In other words, the correction for the zodiacal light in the CMB power spectrum C_ℓ is rather small. In [47], a list of 28 detected asteroids and their parameters measured at the Planck frequency bands is presented. It is assumed that the zodiacal light studies will be continued and augmented with polarization measurements. In addition, a separate study of Kuiper Belt emission is planned.

5.2 Galactic studies

Diffuse galactic emission is interesting not only as a contaminating factor in the CMB analysis but also as an important component providing invaluable information on the physics of our Galaxy. Each release of the Planck collaboration papers discussing the obtained results contained studies of the galactic diffuse emission and extended objects. Submillimeter bolometers of the Planck mission made it possible to study the galactic distribution of dust and molecular gas.

5.2.1 Interstellar medium. The comparative analysis of dust maps at 353, 545, and 857 GHz and IRAS (Infrared Astronomical Satellite) maps at 3000 GHz (100 μm) and 5000 GHz (60 μm), as well as Green-Bank 21 cm maps (emission at the wavelength of atomic hydrogen HI) enables investigations of interstellar dust, high-velocity clouds (HVCs), and intermediate-velocity clouds (IVCs) in the galactic halo [76]. For these studies, 14 high-galactic-latitude fields were chosen on the Planck maps. The structure of the clouds can be probed by the level of correlation between the dust and neutral hydrogen emission and its concentration. As a result, dust emission with a temperature of 20 K was discovered in IVCs, very small dust granules were found to occur four times as frequently as large dust grains, and the conclusion was made that IVCs can be part of the galactic reservoir in which dust destruction and fragmentation occurs. In contrast, no dust emission was found in HVCs. Apparently, the dust grains are combined, as in molecular clouds, due to condensation and star formation processes.

Correlations were also used to study molecular clouds, like the Taurus molecular complex, in which deviations from black-body spectrum and the ^{12}CO and ^{13}CO line emission were found.

5.2.2 Cold clumps. The Planck collaboration published data on an object of a new type: cold clumps, which have been discussed in several papers. For the first time, an all-sky catalogue of 10,342 such cold sources based on the Planck and IRAS data was presented. In these clumps, a cold core is surrounded by warmer matter [78, 79]. The objects were selected by the spatial distribution, dust temperatures, distance, mass, and morphology. The clumps are distributed across the entire sky, including the galactic plane.

A strong spatial correlation of these objects with galactic molecular structures and infrared dark clouds is discovered. The cold clumps are not isolated: they are joined into groups. The temperature of the sources ranges from 7 to 19 K with a peak at 13 K. The distances are measured for about one third of the clumps. Most of them are found within 2 kpc from the Sun. Some sources lie farther than 7 kpc. From the dust emission measurements, their masses are estimated from $0.4M_\odot$ to $2.4\times10^5 M_\odot$, where $M_\odot = 2\times10^{33}$ g is the solar mass. The physical properties of the sources suggest that these clumps are related to different objects, from low-mass nuclei to giant molecular clouds. A statistical analysis reveals at least two populations of objects with temperatures from 7 to 12 K: nuclei located closer to the Sun, and cold clumps inside the inner Galaxy region.

5.2.3 Spinning dust. A separate study is devoted to spinning dust grains, which are associated with anomalous microwave radiation (AMR) [80]. The results of these studies are also required for diffuse component separation. This emission was observed by different experiments in the frequency range from 10 to 60 GHz. Using the Planck maps and multi-frequency external datasets, two sky regions with AMR were studied: molecular clouds in Perseus and the ρ Ophiuchi cloud. In both spectra, the component separation was made into free–free, CMB, warm dust emission, and the electric dipole emission by small dust granules. AMR found with high statistical significance in both fields is peaked at 20–40 GHz. Using the method applied to these two regions, the authors of [80] found two new AMR candidates in the Planck maps, S140 and S235, which are bright HII regions. These objects with AMR are well explained by the spinning dust model.

5.2.4 Molecular gas. Several papers are devoted to the CO molecular gas distribution. These studies were based on the Planck high-frequency bolometer measurements. In particular, the correlation of the HFI Planck maps (from 350 μm to 2 μm) with the IRAS maps (100 μm) allowed measurements of the thermal dust temperature and optical depth distribution [81, 82]. The optical depth, in turn, correlates with the distribution of atomic (HI) and molecular (CO) gas. The correlation with the observed gas column density is linear in the least dense high-galactic-latitude regions. At high $N_{\rm H}$, the correlation is consistent with that for low $N_{\rm H}$ with a given coefficient of transition from CO to H_2. In the intermediate range of $N_{\rm H}$, the correlation with the dust optical depth deviates from a linear dependence.

The discovered excess is explained by thermal dust emission interacting with dark gas, which is not found by available HI and CO surveys. It is shown that the spatial distribution of dark gas in the solar vicinity ($|b_{\rm II}| > 10°$) corresponds to known molecular regions discovered by the CO observations. The measured mean dust emissivity with the HI phase in the vicinity of the Sun, $\tau_{\rm D}/N_{\rm H}^{\rm tot} = 5.2\times10^{-26}$ cm^2

at 857 GHz, approximately corresponds to the power law with the spectral exponent $\beta = 1.8$ at wavelengths up to 3 mm, although the spectral energy distribution somewhat flattens in the millimeter range. The mass of the dark gas is estimated to be 28% of that of the atomic gas and 118% of that of the CO-emitting molecular gas in the solar vicinity. The galactic latitude distribution shows that the dark gas fraction is relatively constant up to several degrees from the galactic plane. A possible explanation of the dark gas is related to the dark molecular phase in which H_2 'survives' during photodissociation and CO does not. The observed transition in the solar vicinity agrees with theoretical predictions. In addition, it is possible that up to half the mass of the dark gas could be in the atomic form due to optical depth effects in the HI measurements.

A separate issue is the CO gas distribution in the Galaxy, which is especially important in radio astronomical studies, because it is used to probe galactic star formation and structure. In molecular radio astronomy, rotational transitions of the CO molecule at frequencies of 115, 230, and 345 GHz are well known. The close observational frequencies of the Planck instruments enabled separation of the corresponding emission components and extraction of the CO gas galactic distribution. We note once again that this emission component is important for monitoring possible CMB map contaminations.

5.2.5 Gould Belt. The study of the diffuse emission from the Gould Belt[5] is interesting [83]. In the southern part of the Gould Belt ($130° \leqslant l \leqslant 230°$ and $-50° \leqslant b \leqslant -10°$), low-frequency galactic components (synchrotron radiation, free–free emission, and anomalous microwave radiation) were separated and analyzed. It was shown that the synchrotron radiation is insufficient to account for the background emission, and AMR due to vibrational and rotational dust emission dominates in this galactic region.

5.2.6 Haze around the galactic center. Finally, we discuss the Planck measurements of the 'haze' around the galactic center (Fig. 17) in the microwave range [84]. The haze represents a separate diffuse component of the galactic emission around the galactic center extending up to latitudes $|b| \sim 35° - 50°$ and longitudes $|l| \sim 15° - 20°$, which was discovered already in the WMAP data [85]. The size and boundaries of the haze coincide with the 'bubbles' observed in gamma rays by the Fermi satellite [86]. This suggests a relation between the haze and Fermi bubbles and requires further studies to explain the galactic cosmic ray acceleration mechanisms. The Planck data confirm the presence of the haze around the galactic center in the microwave range. The seven-year WMAP data were processed jointly with low-frequency LFI data to show that the haze is indeed seen in the microwave range and that the results of both missions are in agreement in amplitude and spectrum. The residual signal, obtained after subtracting the CMB restored only from the HFI data in which the haze is virtually invisible, allowed finding the haze spectral exponent. It turned out that the haze spectrum is described by a power law with the exponent $\beta_H = -2.55 \pm 0.05$ and most likely corresponds to synchrotron radiation, excluding the free–free mechanism. The haze region can be considered a separate emission component but not a region from the general template of the synchrotron radiation map with an individual spectral exponent. The haze morphology remains almost the same in the frequency range 23–44 GHz, which suggests the absence of variations of β_H depending on the measurement location. The polarization in this formation will be studied in the future.

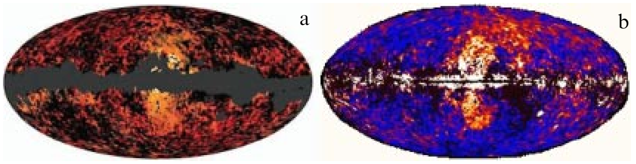

Figure 17. (Color online.) (a) A 'haze' structure near the galactic center in accordance with Planck's data. The galactic plane is masked. (b) Gamma-ray 'bubbles' in accordance with the Fermi satellite data. The maps are constructed in galactic coordinates.

5.3 Galaxies

Due to the relatively low angular resolution of the Planck maps (5′), most of the galaxies look like point-like or low-extended microwave sources. Therefore, their studies are focused on flux measurements, including flux time variations, on the spectral energy distribution, and on the statistical properties of the sources.

5.3.1 Magellanic Clouds. There *are* extended extragalactic objects on the sky. These are the Large and Small Magellanic Clouds (LMC and SMC). To study microwave emission from these nearby galaxies, the standard procedure of background component separation was performed, and the CMB and the galactic background components were removed [87]. After that, the energy spectral distribution in the Magellanic Clouds in the millimeter and submillimeter ranges was studied. The remaining emission correlates with the atomic and molecular gas emission. Thermal emission is also observed in the inner arm of the LMC. It is also shown that there is a cold outer arm. Several cold regions of this arm are identified with known molecular clouds. The SMC emission shows an excess in the millimeter range and spectral flattening in the submillimeter range. The discovered effect can be explained by a combined radiation of warm spinning dust and its grains composed of more amorphous granules than those of the Milky Way dust.

5.3.2 Andromeda galaxy. The Andromeda galaxy (M31) is one of the few galaxies with a large angular size that can be resolved by the Planck instruments (Fig. 18). The galaxy is visible at all Planck mission frequencies [88]. At high frequencies, the dust emission is resolved into the M31 spiral arms and smaller structures. The dust heating mechanism in different parts of M31 was studied. It was found that at long wavelengths (> 0.3 mm), the heating is determined by the diffuse stellar population (visible in the emission at 3.6 μm), and at shorter wavelengths, the dust is heated by the combined emission from the old stellar population and star formation regions (according to 24 μm measurements).

The Andromeda energy spectrum was constructed in each 5′ pixel, and dust properties were calculated across the galaxy with different dust heating mechanisms taken into account.

---

[5] The Gould Belt, which includes a group of very young massive stars with ages up to 30 mln years, has the shape of a disk 500–1000 pc across, whose center is located 150–250 pc away from the Sun towards the Galaxy anticenter. The system is named after Benjamin Gould, who first noticed this region.

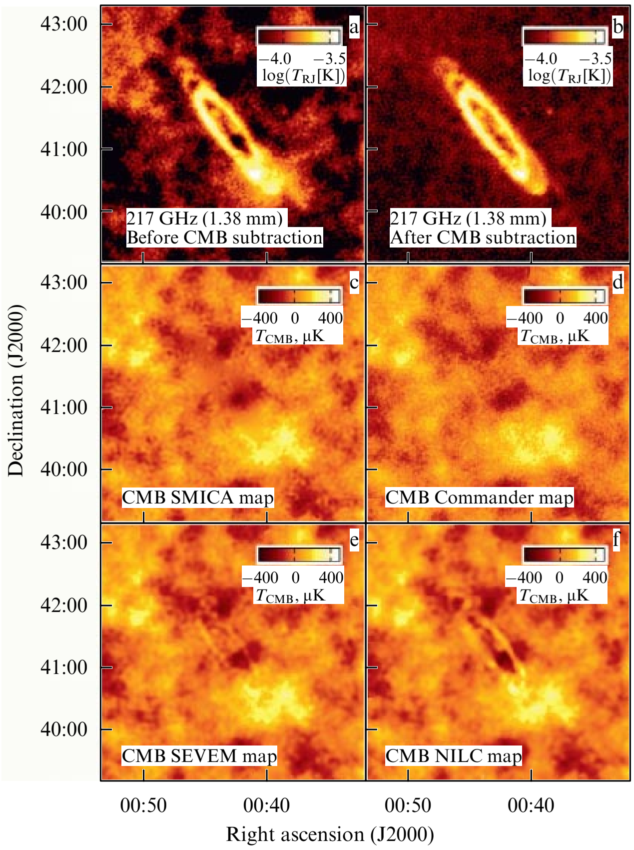

Figure 18. (Color online). M31 at 217 GHz (1.38 mm) (a) before and (b) after the CMB subtraction (SMICA map at 217 GHz). The same region on the CMB (c) SMICA, (d) Commander, (e) SEVEM, and (f) NILC maps.

The dust temperature was found to linearly decrease with the galactocentric distance if the heating is due to an old stellar population, which could be expected when the temperature decreases from 22 K near the galaxy nucleus to 14 K outside the 10 kpc ring. The integral Andromeda spectrum was measured to be in good agreement with the dust temperature (18.2 ± 1.0) K with the spectral exponent 1.62 ± 1.0, assuming one black-body component but with the addition of a significant free–free component at intermediate frequencies of 20–60 GHz. For this model, the star formation rate is calculated to be $0.4 M_{\odot}$ per year, which is in agreement with the rate derived from H_{α} data. In addition, at the 2.3σ level, the spinning dust emission with the amplitude 0.7 ± 0.3 Jy at 30 GHz was found, which the is also observed in our Galaxy.

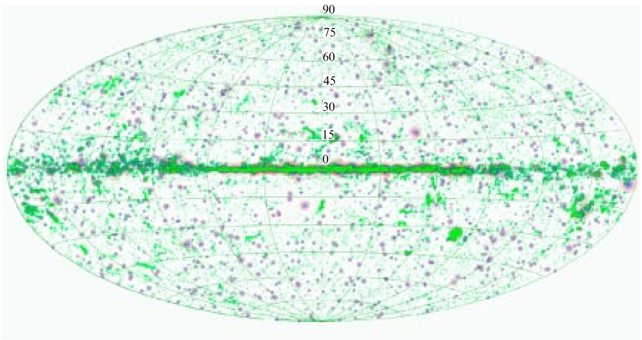

Figure 19. (Color online.) Positions of Planck catalogue sources on the sky. Different colors show data at different frequencies: 30 GHz (purple), 143 GHz (pink), and 857 GHz (green). (From [92].)

5.3.3 The Planck source catalogue. The building of an extragalactic source catalogue containing mm and sub-mm fluxes is expected from the extragalactic source studies. In each Planck data release and corresponding publications, there are updated catalogues of sources discovered by the Planck mission [89–93]. The last version of PCCS2 (Planck Catalogue of Compact Sources 2) contains 1560 sources (the 90% completeness level is 427 mJy, the fraction of coincidence with nearby channel objects is 50.1%) at 44 GHz, 1296 sources (501 mJy, 86.8%) at 70 GHz, 4229 (269 mJy, 71.6%) at 100 GHz, 6229 sources (177 mJy, 81.9%) at 143 GHz, 18,977 sources (152 mJy, 66.1%) at 217 GHz, 24,009 sources (304 mJy, 88.7%) at 353 GHz, 32,782 sources (555 mJy, 85.8%) at 545 GHz, and 4818 sources (791 mJy, 74.9%) at 857 GHz. The object lists are built separately at each frequency. The angular resolution varies depending on the frequency from 32.88′ to 4.33′. It is noted in [93] that the confidence of the catalogue sources is > 80 %, and more than 65% of objects are discovered in at least two channels. Figures 19–21 demonstrate some characteristics of the catalogue: sky location, completeness, and distribution of spectral exponents calculated using consecutive Planck mission frequencies.

At high frequencies, the catalogue includes many galactic objects. Most of the extragalactic sources in the catalogue are nearby galaxies. Of them, 1717 are infrared galaxies from the IRAS sky survey, for which energy spectral distributions are built. Among the last objects, a group with cold dust ($T < 20$ K) is singled out, which was not observed previously.

The Planck catalogue also includes extragalactic radio sources identified with active galactic nuclei — radio galaxies, quasars, and blazars. Measurement at the nine Planck frequencies improved the spectral energy distribution in these sources, ranging from radio to gamma rays, in the poorly studied frequency range. This helps in discussing charged particle acceleration in shocks and jets from active galactic nuclei. The Planck data suggest that the gamma-ray emission emerges in the same shocks that produce radio emission. The source statistics observed at different wavelengths allow separating these objects into groups and performing independent calculations and estimating their contribution to the luminosity function. We also note that, in the Planck maps in different frequency channels and the maps containing the cleaned CMB emission, at a 3σ level (below the sensitivity of Planck catalogues), there are quite a few extragalactic sources with different radio spectra [94, 95].

The photometric data of the Planck catalogue combined with the IRAS measurements enables distant ($z > 2$) objects to be found [96]. For this, the brightest cold submillimeter sources with a spectral energy distribution peak between 353 and 857 GHz were selected. The total list includes 2151 high-z candidate sources (Planck High-Z source, PHZ), which were selected in the most background-clean sky regions (with a total area of 26%) at a flux level above 500 mJy at the 545 GHz frequency. Being present as spike sources in the infrared cosmic backgrounds at a level close to the confusion limit, these PHZ candidates have cooler colors than their surroundings, which is consistent with objects at $z > 2$ under the assumption of the dust temperature $T_{\text{xgal}} = 35$ K and the spectral exponent $\beta_{\text{xgal}} = 1.5$.

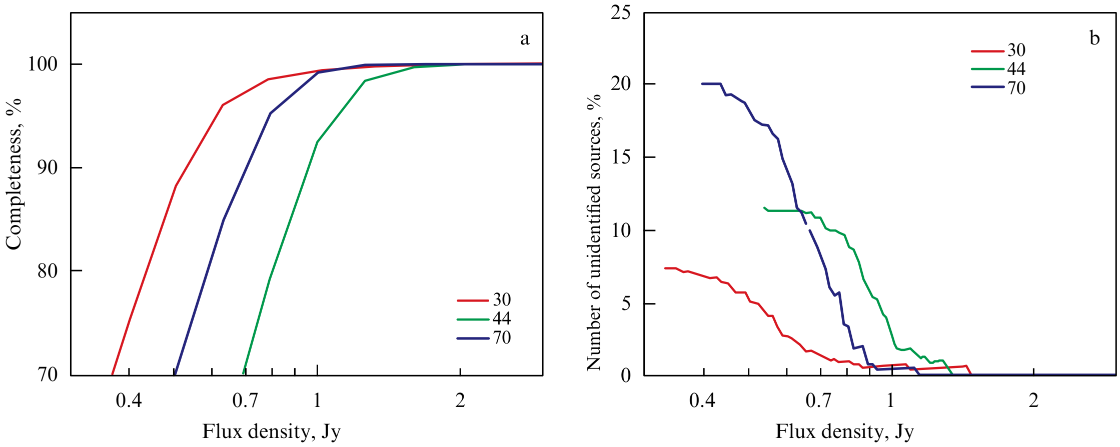

Figure 20. (Color online.) (a) The completeness and (b) the number of unidentified sources at frequencies of 30, 44, and 70 GHz. (From [92].)

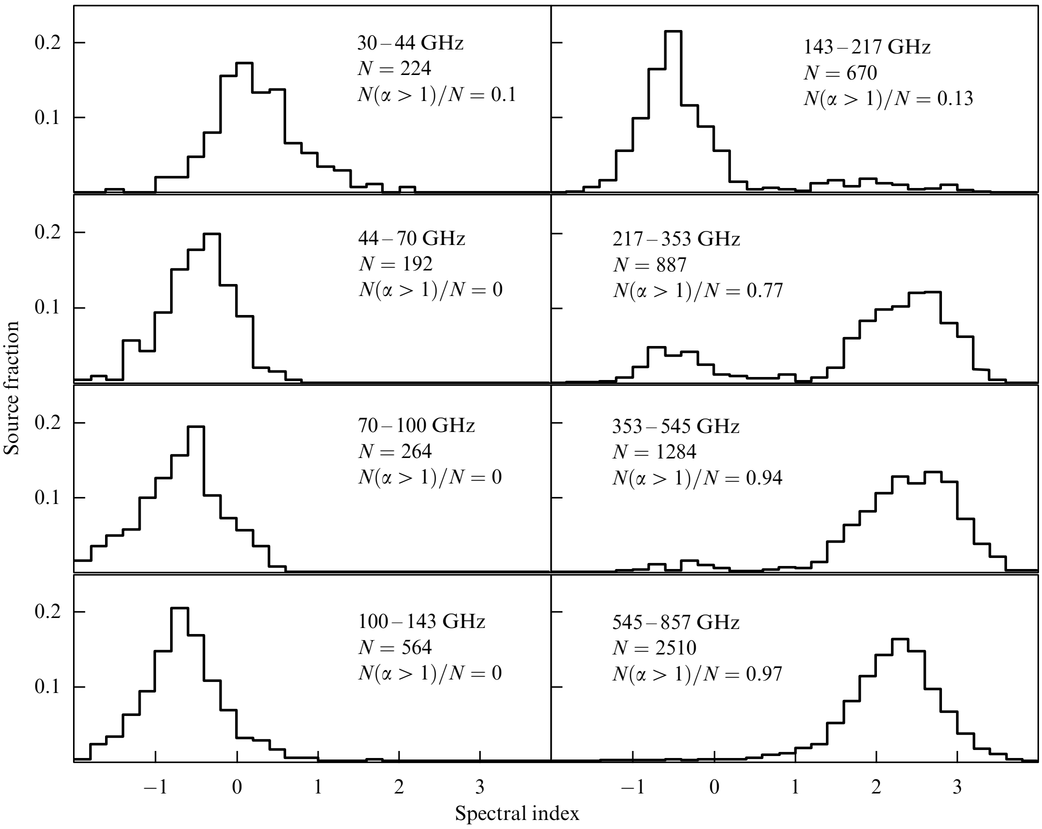

Figure 21. Normalized distribution of spectral exponents of the Planck sources at high Galactic latitudes, $|b| > 30°$. The spectral exponents are calculated using source intensities at adjacent frequencies. (From [92].)

The first observations from the optical-to-submillimeter range [96] confirmed that the PHZ catalogue includes objects from two different populations. A small fraction (about 3%) of the objects is identified with strongly gravitationally lensed star-forming galaxies, which are the brightest submillimeter objects with a flux density from 350 mJy to 1 Jy at 545 GHz at redshifts from 2 to 4.

But most of the PHZ objects appear as a background excess of dusty star-forming galaxies with colors corresponding to the source redshifts $z > 2$. These sources can be considered proto-galaxy cluster candidates. From this standpoint, the PHZ catalog represents an original sample adding to the Planck PSZ2 catalogue with objects showing the SZ effect. The PSZ2 catalogue includes the population of virialized massive galaxy clusters with an SZ signal at redshifts $z < 1.5$. The PHZ objects with $z > 1.5$ allow studies of pre-galaxy clusters, opening an additional window into the investigation of the early stages of structure formation at the intense early phase of star formation at large redshifts.

5.3.4 Sunyaev–Zeldovich effect on bright galaxies. The last galactic study to be mentioned here already relates to cosmology. For the brightest nearby galaxies, estimates of the dark matter halo mass were made based on the SZ effect [58, 97] and on the galaxy mass that influences this effect [98]. For these studies, 260,000 SDSS (Sloan Digital Sky Survey)

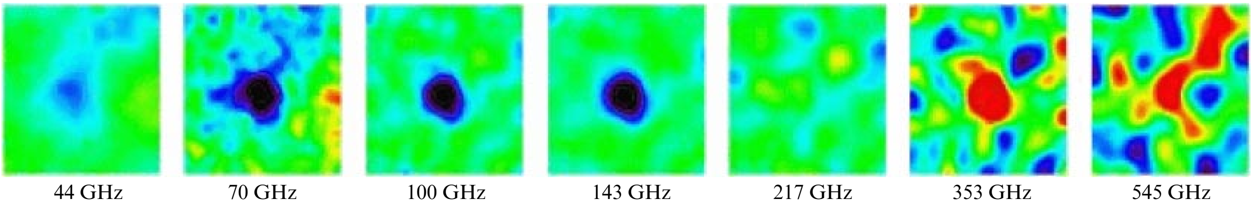

Figure 22. (Color online.) Sunyaev–Zeldovich effect on the Abell 2319 galaxy cluster. From left to right: the same sky field at frequencies of 44, 70, 100, 143, 217, 353, and 545 GHz.

galaxies were selected. Using averaged data and the results of the Millenium Cosmological Simulations, the SZ signal was measured down to masses $M \sim 2 \times 10^{11} M_{\odot}$, assuming the power-law gas halo density observed in galaxy clusters. The effect in low-mass haloes assumes that a quarter of all baryons reside in the hot halo gas, and this gas is less dense than dark matter, which is confirmed by X-ray observations.

5.4 Galaxy clusters

5.4.1 Sunyaev–Zeldovich effect on galaxy clusters. We now turn to the main results of the Planck mission. Discovering galaxy clusters using the SZ effect is one of the main goals of the mission. This problem is considered in 23 papers that studied galaxy clusters and described the results of application of parameters of the SZ clusters of galaxies in cosmology. The latest results are summarized in [99–101].

We recall that the SZ effect [58, 97] (see also [102]) is due to the inverse Compton interaction of CMB photons with free electrons in the hot gas of a galaxy cluster (see also the Kompaneets equation in [103]). The SZ amplitude is determined by the so-called Comptonization y-parameter and depends only on the physical characteristics of the cluster: the temperature of electrons T_{e} and their number density n_{e},

$$y = \frac{k\sigma_{\mathrm{T}}}{m_{\mathrm{e}}c^2} \int^{l} T_{\mathrm{e}}(l)\, n_{\mathrm{e}}(l)\, \mathrm{d}l\,, \tag{15}$$

where k is the Boltzmann constant, σ_{T} is the Thomson scattering cross section, $m_{\mathrm{e}}c^2$ is the rest-mass energy of an electron, and l is the length along the line of sight. The total SZ effect is characterized by the integral Compton parameter $Y = \int y\, \mathrm{d}\Omega$, where Ω is the solid angle subtended by a cluster on the sky. We can write $D_{\mathrm{A}}^2 Y = (\sigma_{\mathrm{T}}/m_{\mathrm{e}}c^2) \int p\, \mathrm{d}V$, where D_{A} is the angular distance to the object (determined by the angular diameter) and $p = n_{\mathrm{e}}kT_{\mathrm{e}}$ is the electron pressure. In the analysis, integral quantities Y_{500} and Y_{5R500} are also used, which are calculated for spheres with radii of R_{500} and $5R_{500}$, where R_{500} is the size of the cluster determined for the region in which the density of matter is 500 times higher than the critical density in the Universe.

There are two types of the SZ effect: thermal, in which photons are scattered by randomly moving thermal electrons, and kinematic, caused by the bulk motion of electrons. In the thermal SZ effect, the scattered CMB photons have a spectral dependence, while during the kinetic SZ effect, the CMB spectrum remains Planckian. In the thermal SZ effect at low-frequency Planck mission channels, the mm signal from the direction to a galaxy cluster is negative (i.e., a deficit of photons is observed due to their upscattering on electrons). In the submillimeter range, due to an increase in the number of photons at higher energies, an excess of CMB emission is observed in the direction to the cluster (Fig. 22).

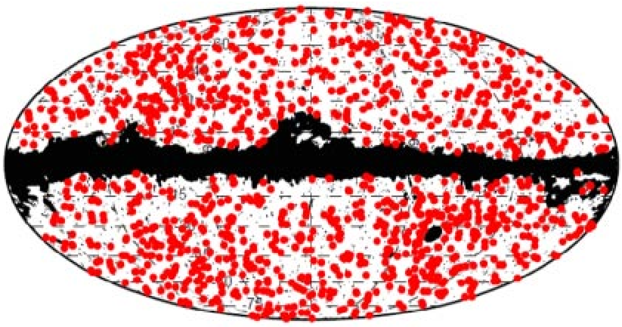

Figure 23. Location of the SZ clusters of galaxies on the sky in galactic coordinates. The masked region is shown in black.

The SZ effect has several advantages in galaxy cluster studies. The Comptonization y-parameter, which measures the integral gas pressure along the line of sight and determines the SZ amplitude, does not suffer from cosmological brightness dimming. This makes the SZ effect a powerful tool in searching for high-redshift galaxy clusters. In addition, the total SZ effect integrated over the cluster angular diameter directly estimates the total thermal gas energy and hence the mass, which is expected to correlate with the temperature (see Fig. 22).

From 29 months of Planck mission observations, a catalogue containing 1653 galaxy clusters and cluster candidates from 83.5% of the total sky in which the SZ effect is observed was built (Fig. 23). The catalogue includes 1203 galaxy clusters confirmed by optical observations. This catalogue is the largest and the most complete one and contains 1094 objects with a known redshift up to $z \sim 1$. The cluster masses fall within the wide range $(0.1\text{–}1.6) \times 10^{15} M_{\odot}$.

The Coma cluster was studied separately, and its physical conditions were estimated. In particular, two shock fronts were discovered moving with velocities two times higher than the sound speed in the cluster's gas. The results of observations also suggest that the magnetic field decreases towards the cluster outskirts much more slowly than thought previously.

The relation between the cluster mass and the SZ-signal amplitude was also checked using the Planck data. For this, mass estimates obtained in the program of weak gravitational lensing observations by the Subaru telescope and the XMM-Newton (X-ray Multi-Mirror Mission) observatory were used. Good agreement between the Planck estimates and the Subaru data was found, while the X-ray measurements inside the R_{200} radius overestimate the cluster mass by $\sim 20\%$. It has been shown that the difference between the estimates obtained by the two methods is significant for perturbed galaxy systems and is related to a shift in the galaxy center position as determined by different methods [104].

5.4.2 Interaction between galaxy clusters. The Planck mission first discovered gas between interacting galaxy clusters. The intergalactic and intracluster gas can contain up to half the baryons of the Universe. This gas is distributed in the form of filaments (like fibers in a spiderweb) and represents a hot low-density medium. Attempts to find it using X-ray observatories failed because of limited sensitivity. Pairs of galaxy clusters are good candidates for the Planck searches for hot gas. Selected galaxy cluster pairs were studied on the microwave maps, and one of them, A339–A401, revealed a significant SZ signal between the clusters [106] (Fig. 24). In the filament, the physical parameters (the temperature $kT = 7.1 \pm 0.9$ keV, corresponding to previous estimates, and the baryon number density $(3.7 \pm 0.2) \times 10^{-4}$ cm^{-3}) were determined.

The Planck mission also (jointly with the XMM-Newton X-ray observatory) discovered the triple galaxy cluster PLCKG214.6 + 37.0, which is in the merging phase. For all three components, redshifts were measured by the X-ray iron line, and it was confirmed that the three clusters probably belong to one supercluster. Analysis of the dynamics of the objects and the lack of detectable X-ray excess suggest that the system is still at the early stage of merging.

6. Cosmology

The number of cosmology papers by the Planck collaboration increases with every data release. The papers are devoted to determining not only cosmological parameters but also different physical and geometrical properties of the Universe. Part of the Planck results is related to the SZ effect observations. Another, more fundamental, part is devoted to the analysis of the primordial anisotropy of the CMB temperature.

6.1 Peculiar velocities of galaxy clusters

Among the papers of the first cycle, we note studies of the peculiar velocities of galaxy clusters using the kinetic SZ effects caused by the proper motion of the clusters, which is different from the thermal SZ effect described in Section 5.6. A study of galaxy cluster velocities was initiated by a series of papers by the American astrophysicist Kashlinsky [107, 108] related to the discovery of the so-called dark flow of the large-scale structure, i.e., the motion of a giant mass of matter in the Universe. This conclusion was made from the WMAP data, whose angular resolution was insufficient to see this effect directly, but the estimate was made by adding a dipole to the CMB pixels corresponding to the location of galaxy clusters.

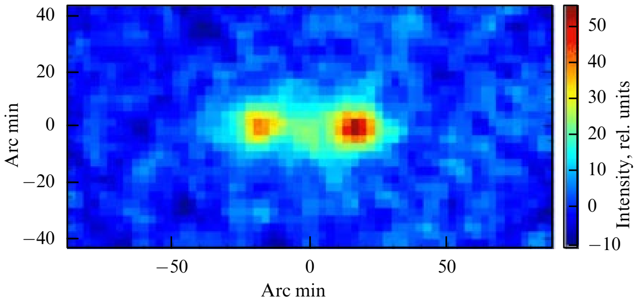

Figure 24. (Color online.) SZ filament connecting the pair of interacting clusters of galaxies A339–A401 in the microwave Planck observations. (From [105].)

The Planck collaboration devoted a special paper to this problem [109]. The list of galaxy clusters includes both the Planck results and data from the catalogue of X-ray clusters.[6] By separating the kinematic SZ effect using special filters at the locations of clusters of galaxies, the authors estimated the matter velocity amplitude. The mean redshift of the entire sample of galaxy clusters was $z = 0.8$. The measured peculiar velocity, which was in fact monopole at that cosmological epoch, was found to be 72 ± 60 km s^{-1}. As can be seen from the last value, the error in the velocity estimate is quite large. In addition, this estimate is less than 1% of the relative velocity of the Hubble flow (expansion velocity) of the cluster sample in the local CMB reference frame in our neighborhood. If there is matter flow in the volume centered on the Local Group of galaxies, then the upper limit of the galactic velocities in this frame, 254 km s^{-1} (at a 95% confidence level), shows that this estimate is dominated by instrumental noises and CMB dispersion. This, in turn, suggests that the Universe is very homogeneous on the gigaparsec scale, and large-scale matter flows observed from the kinematic SZ effect correspond to the standard ΛCDM (Lambda Cold Dark Matter) model. In other words, nothing special has been found.

6.2 Anisotropy of the cosmic infrared background

The anisotropy of the cosmic infrared background (CIB) was studied in one of the early Planck collaboration publications [110], and further results can be found, in particular, in [62]. The CIB anisotropy presumably reflects the large-scale structure of the Universe and can be used to study galaxy mergers, which, in turn, are related to the formation of dark matter halos. The dark matter clustering mechanisms are generally well understood; therefore, the CIB anisotropy can be used to find the relation between dusty star-forming galaxies and dark matter distribution. High-frequency Planck instruments are very suitable for these studies.

To calculate the angular power spectrum for multipoles ranging from $\ell = 200$ (angular size $\sim 27'$) to $\ell = 2000$ ($\sim 3'$), six sky fields with a low level of galactic dust emission were selected. Observational data were taken at 217, 353, 545, and 857 GHz. The total area of the field was about 140 square degrees. To eliminate the galactic dust emission, neutral hydrogen radio maps (at 21 cm) were used, and the CMB emission was removed using the Planck maps at 143 GHz. By applying the model including dusty galaxies, a multi-parameter model of the evolution of galaxies, and a simple model of dark mater halo formation, the authors found a good correspondence between the measured angular power spectrum of the CIB anisotropy and the model. It was also shown that halo forms calculated at different frequencies should be different because the main contribution comes from different redshifts at different frequencies. According to the Planck data, half the power in the signal anisotropy for the $\ell = 2000$ multipole is due to galaxies with redshifts $z < 0.8$ at 857 GHz and with $z < 1.5$ at 545 GHz, while distant objects with $z > 2$ contribute 90% at 353 and 217 GHz.

6.3 Angular power spectrum and determination of cosmological parameters

Measurement of cosmological parameters has been one of the main results of the Planck mission published to date. To do this, it is first of all necessary to build the CMB map and the

---

[6] MCXC: the Meta Catalogue of X-ray detected Clusters of galaxies.

corresponding power spectrum C_ℓ, which is the correlation function C_ℓ^{TT} of temperature fluctuations. The CMB power spectrum is determined by the sum of weighted squares of mode harmonic amplitudes for a given number ℓ described by the coefficients $a_{\ell m}$. These coefficients, which are calculated by expanding maps in multipoles, determine the contribution of harmonics to the map under analysis:

$$C_\ell = \frac{1}{2\ell+1} \sum_{m=-\ell}^{\ell} |a_{\ell m}|^2 . \tag{16}$$

We note that the Gaussian distribution of the $2\ell+1$ coefficients $a_{\ell m}$ is assumed in Eqn (16), and their squared amplitudes are averaged with equal weights. In this case, for a two-point correlation (with the averaging done over an ensemble of universes), we have

$$\langle a_{\ell m} a^*_{\ell' m'} \rangle = C_\ell \delta_{\ell\ell'} \delta_{mm'} . \tag{17}$$

We also note that for non-Gaussian data, the averaging of ℓ at a given C_ℓ is no longer obvious. In addition, the CMB signal is assumed to be ergodic, which means that averaging over an ensemble of universes is equivalent to averaging the spectra measured from different locations of the observer in the Universe. We recall that C_ℓ is measured on our sky, and a different observer's location would yield a somewhat different C_ℓ. The actual spectrum C_ℓ can be estimated by averaging over all observers, which is equivalent to averaging over an ensemble of admissible universes. The presence of noise in the data also affects the true values of $a_{\ell m}$ in the sky multipole expansion. But even for ideal data, we could measure only $2\ell+1$ modes for low multipoles ℓ. This leads to an internal variance (dispersion) in the spectrum called the cosmic (better to say, cosmological) variance, or cosmological uncertainty.

We recall that the CMB power spectrum is shaped by many physical processes during the recombination stage related to density, velocity, and metric perturbations evolving as sound waves (see monographs [111–113]). The CMB fluctuations after the recombination are modulated by sound waves in the plasma at the stage prior to recombination, according to the effect of baryonic oscillations predicted by Sakharov [114]. The CMB anisotropy caused by the Sakharov oscillations manifests itself in the power spectrum of fluctuations in the multipole domain.

Thus, the formation conditions of the CMB fluctuations, and hence the corresponding cosmological parameters are 'imprinted' in the CMB power spectrum, and in fact determine the present state of the Universe. Therefore, the coefficients $a_{\ell m}$ and the corresponding angular power spectrum, on the one hand, are measured from observations, and on the other hand, describe the physics during the generation of density perturbations. There is a theoretical linear relation between the primordial fluctuations given by adiabatic scalar perturbations and the coefficients $a_{\ell m}$ [115]:

$$a_{\ell m} = (-\mathrm{i}) \int \frac{\mathrm{d}^3\mathbf{k}}{(2\pi)^3}\, \Phi(\mathbf{k})\, g_{\mathrm{Tl}}(k)\, Y^*_{\ell m}(\hat{\mathbf{k}}) , \tag{18}$$

where $\Phi(\mathbf{k})$ describes the primordial density perturbation (more precisely, perturbation of the gravitational potential) in the Fourier domain, $g_{\mathrm{Tl}}(k)$ is a transfer function, $\mathbf{k}$ is the wave vector, and $\hat{\mathbf{k}} = \mathbf{k}/k$ is the unit vector. The temperature fluctuations $\Delta T(\theta, \phi)$ and the primordial fluctuations $\Phi(\mathbf{k})$ are also linearly related. The full transfer function $g_{\mathrm{Tl}}(k)$ can be calculated using the CAMB (Code for Anisotropies in the Microwave Background) package [116].

Thus, the power spectrum C_ℓ is a function of cosmological parameters [111]:

$$C_\ell \equiv C_\ell(h, \Omega_{\mathrm{b}} h^2, \Omega_{\mathrm{CDM}} h^2, \Omega_\Lambda, \Omega_\nu, n, \ldots) . \tag{19}$$

This, in particular, involves the Hubble constant $h = H_0/100$ km s^{-1} Mpc^{-1}, the baryonic matter density Ω_{b}, the dark matter density Ω_{CDM}, the dark energy density Ω_Λ, the density of massive neutrinos Ω_ν, and the spectral exponent of adiabatic fluctuations n (spectral slope). If we know the physical mechanisms of angular power spectrum formation and we can calculate it from cosmological parameters, and if it is known from real observations, the inverse problem of extracting cosmological parameters from the observed angular power spectrum of CMB fluctuations can be solved. The algorithm for solving this problem is realized in the well-known cosmological CAMB software package.[7] For example, Fig. 25 shows the CMB power spectra calculated by CAMB for different cosmological parameters.

We note that observations with a partial sky coverage (for example, from Earth or using masks) have some peculiarities in the data analysis associated with the boundaries of observed fields, which should be taken into account.

In addition to C_ℓ^{TT}, correlation functions corresponding to the E- and B-polarization modes C_ℓ^{TE}, C_ℓ^{EE}, C_ℓ^{TB}, and C_ℓ^{BB} are also used in the CMB data analysis. Table 3 lists the location and amplitudes (with the notation $D_\ell = \ell(\ell+1)\, C_\ell/2\pi$) of peaks of three power spectra obtained by the Planck mission [11]. Figure 26 shows the Planck CMB map and the angular power spectra C_ℓ^{TT}, C_ℓ^{TE}, and C_ℓ^{EE}.

6.3.1 Parameterization. In the analysis of the angular power spectra, the standard analysis and procedures especially modified for the Planck data processing were used (in

Table 3. Location of peaks in the Planck power spectra D_ℓ^{TT}, D_ℓ^{TE}, and D_ℓ^{EE}

Number of peak	Location ℓ	Amplitude, μK^2
TT-power spectrum		
1	220.0 ± 0.5	5717 ± 35
2	537.5 ± 0.7	2582 ± 11
3	810.8 ± 0.7	2523 ± 10
4	1120.9 ± 1.0	1237 ± 4
5	1444.2 ± 1.1	797.1 ± 3.1
6	1776 ± 5	377.4 ± 2.9
7	2081 ± 25	214 ± 4
8	2395 ± 24	105 ± 4
TE-power spectrum		
1	308.5 ± 0.4	115.9 ± 1.1
2	595.3 ± 0.7	28.6 ± 1.1
3	916.9 ± 0.5	58.4 ± 1.0
4	1224 ± 1.0	0.7 ± 0.5
5	1536 ± 2.8	5.6 ± 1.3
6	1861 ± 4	1.2 ± 1.0
1	137 ± 6	1.15 ± 0.07
2	397.2 ± 0.5	22.04 ± 0.14
3	690.8 ± 0.6	37.35 ± 0.25
4	992.1 ± 1.3	41.8 ± 0.5

---

[7] Available online at http://lambda.gsfc.nasa.gov/toolbox/tb_camb_form.cfm.

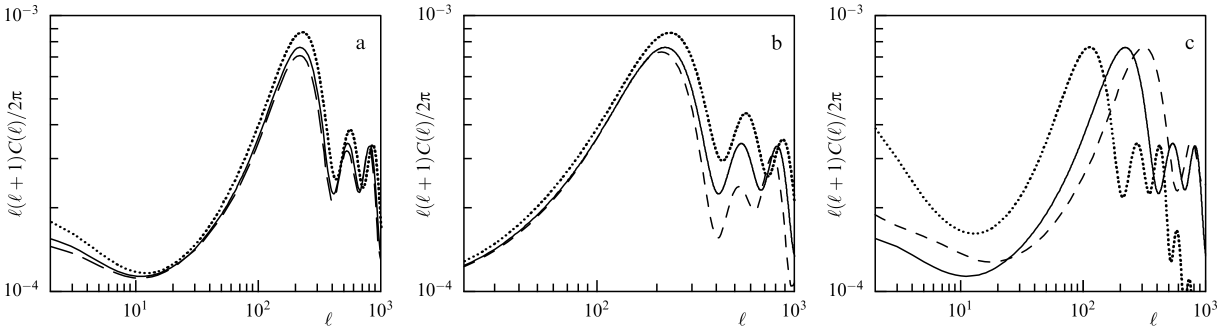

Figure 25. The CMB angular power spectrum $\ell(\ell+1)\,C(\ell)/2\pi$ for different cosmological parameters. The solid line shows the power spectrum in the standard ΛCDM model ($\Omega_{\text{CDM}} = 0.26$, $H_0 = 68$ km s^{-1} Mpc^{-1}, and the curvature density parameter $\Omega_K = 0$). (a) Dependence on the dark matter density parameter Ω_{CDM}. The respective dotted and dashed lines correspond to $\Omega_{\text{CDM}} = 0.17$ and $\Omega_{\text{CDM}} = 0.27$. (b) Dependence on the Hubble constant. The respective dotted and dashed lines correspond to $H_0 = 60$ km s^{-1} Mpc^{-1} and $H_0 = 85$ km s^{-1} Mpc^{-1}. (c) Dependence on the curvature parameter Ω_K. The respective dotted and dashed lines correspond to $\Omega_K = -0.3$ and $\Omega_K = 0.3$, respectively.

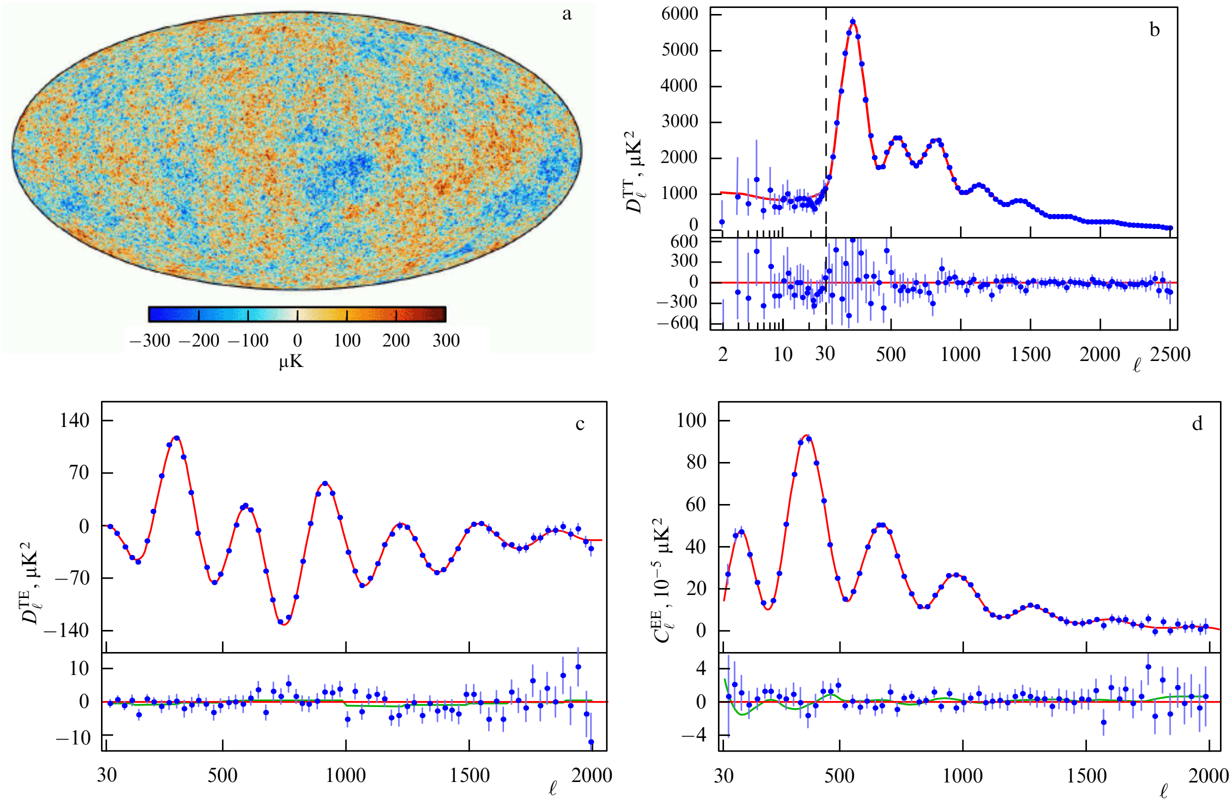

Figure 26. (Color online.) (a) Most probable CMB anisotropy map with a 5′ resolution obtained from the joint analysis of the WMAP and Planck 408 MHz data. The central narrow strip in the galactic plane with 1.6% of the all-sky area is filled with the model signal properties like the rest of the sky. The angular power spectrum D_ℓ^{TT} from the Planck 2015 data (upper panel). The solid line shows the ΛCDM model best fitted to the Planck TT-spectra at low multipoles. The residuals are shown in the bottom panel, with 1σ errors indicated. (c) TE-spectrum and (d) EE-spectrum from the Planck data. Solid lines in the upper panels of Fig. (c) and (d) show ΛCDM spectra derived from the CMB temperature anisotropy. The residuals are shown in the bottom panels. The error bars reflect $\pm 1\sigma$ deviations in the model due to independent fitting of the TT-spectra and separate fitting of the TE- and EE-spectra. (From [117].)

particular, in [118], and with slight modifications, in [117]). The CMB anisotropy is treated as small fluctuations in the Friedmann–Lemaître–Robertson–Walker metric evolving in accordance with General Relativity. Under these assumptions, the evolution of perturbations can be very precisely calculated using a Boltzmann code for the CMB [116], taking the initial conditions, ionization history, and components of the Universe into account. It is assumed that the pressure of cold dark matter is zero, is stable and noninteracting, and has the physical density $\omega_{\text{c}} = \Omega_{\text{CDM}} h^2$, with the Hubble constant $H_0 = 100h$ km s^{-1} Mpc^{-1}. Baryons primarily consist of hydrogen and helium, and their density is $\omega_{\text{b}} = \Omega_{\text{b}} h^2$. The helium fraction Y_{P} is parameterized. The standard Big Bang nucleosynthesis (BBN) can be modeled to calculate Y_{P}, the photon-to-baryon number ratio, and the expansion velocity depending on the number of relativistic degrees of freedom. These calculations were done with the PArthENoPE BBN cosmological package [119]. The CMB photon temperature is well known: $T_0 = 2.7255 \pm 0.0006$ K. Thermodynamic equilibrium is assumed to hold until the neutrino decoupling [118], which is almost (but not fully) completed by the time of electron–positron annihilation. This results in a slight heating of neutrinos in addition to what is expected for photons, and hence leads to a slight deviation from the thermal equilibrium prediction $T_\gamma = (11/4)^{1/3} T_\nu$ for the photon temperature T_γ and the neutrino temperature T_ν. When taking the additional neutrino energy density into account, it is assumed that the neutrinos have a thermal distribution with the effective energy density

$$\rho_\nu = N_{\text{eff}} \, \frac{7}{8} \left(\frac{4}{11} \right)^{4/3} \rho_\gamma \,, \tag{20}$$

where the effective number of neutrino types is $N_{\text{eff}} = 3.046$ in the base model. The energy density is equally distributed between three neutrino flavors, which are relativistic.

In calculating the ionization history (at $z \approx 1090$), the duration of the process from the stage of the full hydrogen and helium ionization to the completion of recombination with a residual electron fraction $x_{\text{e}} \sim 10^{-4}$ was taken into account. The CMB power spectrum sensitivity to x_{e} shows up in a change in the sound horizon during recombination, the time of recombination, and details of the recombination transition, which affect the thickness of the last scattering sphere and hence the damping of fluctuations (Silk damping) due to small-scale diffusion, polarization, and averaging of perturbations along the line of sight.

The basic physical processes are modeled using software packages that calculate the corresponding atomic transitions and details of recombination. The HyRec [120] and CosmoRec [121] codes show good agreement at a level that is better than required for the Planck data. The standard code recfast [122] is also used for the recombination analysis to compare the power spectrum C_ℓ with the latest results obtained with HyRec and CosmoRec. The difference turns out to be at the 0.05σ level. Thus, no noticeable deviations from the assumed recombination history have been found. If such deviations were present, the parameter estimates would show a significant offset relative to those found in [117, 118].

The calculations assume purely adiabatic scalar perturbations from the very early times with the power spectrum

$$\mathfrak{P}_{\mathfrak{R}}(k) = A_{\text{s}} \left(\frac{k}{k_0} \right)^{n_{\text{s}} - 1 + (1/2)(\mathrm{d}n_{\text{s}}/\mathrm{d}\ln k)\,\ln(k/k_0)} \,, \tag{21}$$

where A_{s} is the amplitude of primordial perturbations, $k_0 = 0.05\ \text{Mpc}^{-1}$ is the wave number characterizing the scale of perturbations, which is approximately the middle of the logarithmic range of scales probed by the Planck mission, n_{s} is the spectral exponent (the slope of the primordial perturbation spectrum), and $\mathrm{d}n_{\text{s}}/\mathrm{d}\ln k$ is the so-called running exponent, i.e., the running of the spectral exponent showing the rate of the spectral exponent change. Also considered are models with a significant contribution from primordial gravitational waves (tensor modes) parameterized as

$$\mathfrak{P}_{\text{t}}(k) = A_{\text{t}} \left(\frac{k}{k_0} \right)^{n_{\text{t}}} . \tag{22}$$

The corresponding parameter $r_{0.05} \equiv A_{\text{t}}/A_{\text{s}}$ is introduced, which is the ratio of the primordial tensor-to-scalar modes at $k = k_0$. The model for $r_{0.002}$ with $k = 0.002\ \text{Mpc}^{-1}$ close to the scales that are sensitive to the tensor mode in the angular power spectrum at low harmonics was also considered.

The parameterization of dark energy assumed that it is described by the cosmological constant and is represented by the dark energy density Ω_Λ. For dynamical dark energy, the parameter w is introduced into the equation of state, either as a constant or as a function of the cosmological scale factor a:

$$w(a) \equiv \frac{p}{\rho} = w_0 + (1 - a)\, w_a \,. \tag{23}$$

Dark energy interacts with other components only gravitationally (also see reviews [123, 124]).

The main mechanisms of perturbation growth and the CMB fluctuation formation are algorithmicized and included as procedures in the software packages for CMB power calculation [116, 125–130]. The main program for the CMB power spectrum used by the Planck collaboration is based on the numerical Boltzmann-type code CAMB version 2013 and later versions [116]. The program used procedures developed in the CMBFAST [128] and Cosmics [127] codes. The latter calculates gravitational lensing effects in the CMB temperature and polarization maps. Gravitational lensing was taken into account in two ways. First, the CMB power spectra were modeled with smearing at a level of about 5% in the region of acoustic peaks due to the lensing. Second, the lensing was taken into account in the likelihood function by the corresponding potential (mainly in the form of shape squeezing in the CMB trispectrum) in the power spectrum [131]. Theoretical estimates of the power spectrum of the lensing potential were calculated using CAMB. Although the corrections to the temperature anisotropy power spectrum due to gravitational lensing on nonlinearly growing structures are negligible, the consequences of the reconstruction of the lensing potential are important. To describe the nonlinear structure growth, the HaloFit model [132, 133] was used to calculate the power spectrum of the lensing potential.

To investigate the possible cosmological parameter space and calculate confidence intervals, the CosmoMC package that implements the MCMC method was used [134]. This package employs the Metropolis–Hastings mechanism to generate chains to build cosmological parameter samples and to assess variations of the parameters by changing the procedures used. The parameter sample is internally orthogonal, which enables the parameter degeneracy to be probed and the basic parameter set to be obtained. The CosmoMC package has become a de facto standard in different cosmological studies, and is quite naturally used in the Planck data analysis. In this analysis, the set of chains is generated until the calculations converge, and tails of distributions for each parameter are studied inside the confidence intervals [118]. *A posteriori* estimates of each parameter inside the confidence interval were generated for the samples. For the parameters at which the distributions have different tails, the interval is presented between extreme points that have approximately equal marginal density distributions. For parameters with preliminarily calculated bounds, the limits are presented for one distribution tail or are not presented at all, depending on how much the *a posteriori* value of the bound differs from zero. If parameters have an almost symmetric distribution, the mean value and the standard deviations ($\pm 1\sigma$) are given.

6.3.2 Difference between the 2013 and 2015 Planck data releases. To understand the reason for the difference in measurements of cosmological parameters in the two releases, it is necessary to discuss the changes in the 2013 and 2015 data analysis. Briefly, in addition to the sensitivity improvement, the main differences can be summarized as follows (see [117] for more details).

1. Some changes in the low-level data processing [16, 135] were made. They include the filtration algorithm to remove lines due to 4K cooling from the TOD; the method of TOD cleaning from interference due to cosmic rays; the improved absolute calibration due to better satellite orbital dipole measurements; and more precise telescope beam models, which improved the treatment of side lobes.

2. In the 2013 papers, the WMAP polarization data [7] at low multipoles $\ell \leqslant 23$ were used to calculate the optical depth parameter. In the 2015 data analysis and the likelihood function calculations, instead of the WMAP data, the Planck Q- and U-polarization data with low resolution at 70 GHz were used, and the foregrounds were treated using the polarization data at 30 GHz (for synchrotron emission) and at 353 GHz (for galactic dust emission) [136].

3. In the 2013 papers, the likelihood function for the temperature anisotropy analysis was hybrid: for the $\ell = 2-49$ multipoles, it was calculated using the Commander algorithm, and it was applied to 94% of the sky area. At high multipoles ($\ell = 50-2500$), the likelihood function was built from the cross spectra at 100–217 GHz using the CamSpec package [137] and 15.5 months of observations. In the 2015 papers, data obtained over the full mission operation time were analyzed: 29 months for HFI and 48 months for LFI. In the 2015 data analysis, the likelihood functions were built from cross spectra of semi-annual and annual observations. The basic likelihood function for the new anisotropy and polarization data was also hybrid and was constrained for low multipoles, $\ell = 30$, in the pixel maps.

4. The sky coverage in the 2013 data for the CamSpec calculations was intentionally conservative: only 58% of the sky was used at 100 GHz and 37.5% at 143 and 217 GHz. In the 2015 data, the sky area analyzed was increased at each frequency. In addition, to detect point-like sources at each frequency, individual masks were used instead of one mask for all objects discovered at different frequencies.

5. Most of the 2015 results were obtained using the modified Plik package to calculate the likelihood functions, which uses cross spectra obtained over half the time of the mission operation.

6. Foreground component models used in the signal separation were slightly corrected.

Physical models of the generation and evolution of perturbations in the CosmoMC procedure were also improved [138]. In particular, the baryon mass fraction $Y_{\rm P}$ in helium, which was previously not treated as an independent parameter, was calculated directly in the 2015 papers from the BBN predictions by interpolating the fitting formula in the PArthENoPE (Public Algorithm Evaluating the Nucleosynthesis of Primordial Elements) package [119] that calculates the BBN processes. A small error was corrected in the model of dark energy for $w \neq -1$, although it hardly affected the results. To model the matter power spectrum at small scales, an updated halofit procedure was used, which accounts for massive neutrinos.

6.3.3 Gravitational lensing of the CMB. Gravitational lensing of the CMB as observed by the Planck mission is discussed in [131, 139], and should be considered in more detail. A detailed study of this effect by the Planck mission is advantageous relative to the WMAP mission, which did not carry out such studies, and shows the viability of an essential cosmological test. The CMB lensing can be regarded as interference for the analysis of real CMB anisotropy, but at the same time it provides information on the matter distribution at intermediate redshifts ($0.1 < z < 5$) [140]. In the ΛCDM model, there are methods that can calculate the lensing effect on the CMB power spectrum [141] and even reconstruct the lensing potential [142]. Before the Planck results, effects of the CMB lensing were estimated using the WMAP data and large-scale structure data obtained in galaxy surveys [143–145]. In addition, the modern ground-based CMB experiments with low-noise detectors, such as the Atacama Cosmology Telescope (ACT) and the South Pole Telescope (SPT), reliably demonstrated the presence of the CMB lensing signal at a 4.6σ level by ACT [146] and a 8.1σ level in the power spectrum and 6.3σ level for the reconstructed potential from the SPT data [147].

With multiple full-sky coverage at nine frequencies with a comparatively narrow beam and the high sensitivity in the Planck mission, it was natural to study CMB lensing with a deflection angle of photons up to $2.04'$ [131]. In the most sensitive frequency bands of 145 GHz and 217 GHz of the Planck observatory with FWHM $\approx 7'$ and $\approx 5'$ for the respective beams, sensitivities of 30 μK (60 μK in polarization) and 40 μK (95 μK in polarization) were reached in the multipole range $1000 \leqslant \ell \leqslant 3000$ [139]. With these parameters, the lensing potential was reconstructed in the multipole range most sensitive to this effect ($\ell \geqslant 1000$).

The lensing effect is observed as small deflections of the real CMB fluctuations. The observed CMB temperature anisotropy in a direction $\hat{\mathbf{n}}$ can be represented in terms of the nonlensed primary temperature as [131, 142]

$$\begin{aligned} T(\hat{\mathbf{n}}) &= T^{\rm unl}\big(\hat{\mathbf{n}} + \nabla\phi(\hat{\mathbf{n}})\big) \\ &= T^{\rm unl} + \sum_i \nabla^i \phi(\hat{\mathbf{n}})\, \nabla_i T^{\rm unl} + O(\phi^2)\,, \end{aligned} \tag{24}$$

where

$$\phi(\hat{\mathbf{n}}) = -2 \int_0^{\chi_*} {\rm d}\chi \frac{f_K(\chi_* - \chi)}{f_K(\chi_*) f_K(\chi)}\, \Psi(\chi\hat{\mathbf{n}}; \eta_0 - \chi) \tag{25}$$

is the lensing potential. Here, χ is the conformal distance ($\chi_* \approx 14000$ Mpc), which is the distance to the last scattering surface, and $\Psi(\chi\hat{\mathbf{n}}, \eta)$ is the gravitational potential at the conformal distance χ in the direction $\hat{\mathbf{n}}$ at the conformal time η (η_0 for the present epoch). The angular distance $f_K(\chi)$, which depends on the curvature of the Universe, is given by

$$f_K(\chi) = \begin{cases} K^{-1/2} \sin\,(K^{1/2}\chi)\,, & K > 0\,(\text{close})\,, \\ \chi\,, & K = 0\,(\text{flat}), \\ |K|^{-1/2} \sinh\,\big(|K|^{1/2}\chi\big)\,, & K < 0\,(\text{open})\,. \end{cases} \tag{26}$$

The lensing potential is a measure of the integral mass distribution up to the last scattering sphere. The power spectrum of the potential is related to that of matter, which is in turn sensitive to parameters describing the growth of structures, for example, to the neutrino mass [148]. The lensing effect amplitude is also sensitive to geometrical parameters, such as the curvature of the Universe.

In [139], the lensing potential is reconstructed with the help of quadratic estimators that use the statistic anisotropy produced by lensing [149]. Neglecting the lensing of the primordial gravitational-wave B-mode of polarization, five possible estimators can be constructed: $\hat{\phi}^{\mathrm{TT}}$, $\hat{\phi}^{\mathrm{TE}}$, $\hat{\phi}^{\mathrm{EE}}$, $\hat{\phi}^{\mathrm{TB}}$, and $\hat{\phi}^{\mathrm{EB}}$ [139]. They involve different correlations of the CMB temperature (T) and polarization (E and B). Based on these five estimators, the combined estimation algorithm $\hat{\phi}^{\mathrm{MV}}$ of the minimization of deflections is constructed and used to reconstruct the lensing potential.

The following points are taken into account in reconstructing the potential.

I. A fixed lensing potential used in multiple realizations of the CMB temperature anisotropy superimposes a statistical anisotropy on the observed CMB anisotropy; fluctuations then remain Gaussian, but the covariance changes as a function of location and direction on the sky. This idea is used to estimate $\phi(\hat{\mathbf{n}})$. The noise on this map is a combination of the instrumental and statistical noise caused by the analysis of a single observed CMB realization, similar to the noise during galactic lensing.

II. Both the lensing potential and CMB fluctuations averaged over realizations lead to a non-Gaussianity of the observed CMB fluctuations at the lowest orders in the connected part of the four-point correlation function of the CMB (in the trispectrum). This fact is used to measure the lensing power spectrum $C_L^{\phi\phi}$. The corresponding estimators are built by maximizing the likelihood function for the lensed CMB on the basis of the above hypothesis and are expected to be optimal (from the standpoint of minimal variation). The nonoptimal choice would decrease the signal-to-noise ratio.

As noted in [131], the above facts and description do not fully explain how the convergence estimates are matched and the separation on different parts of the sky is eliminated, or which weight should be given to local estimates of the power spectrum, which is a function of the angular scale. These problems are resolved when the estimator of the general form with optimization of its weight function by the sensitivity to the lensing effect is considered [149]. The statistical anisotropy induced by lensing in the first order in the lensing potential is given by the off-diagonal contribution to the CMB covariance matrix [131]:

$$\Delta\langle T_{\ell_1 m_1} T_{\ell_2 m_2}\rangle = \sum_{LM}\sum_{\ell_1 m_1 \ell_2 m_2}(-1)^M \begin{pmatrix} \ell_1 & \ell_2 & L \\ m_1 & m_2 & M \end{pmatrix} W^{\phi}_{\ell_1 \ell_2 L}\phi_{LM}\,. \quad (27)$$

Here, the angular brackets are applied to the CMB realizations with a fixed gravitational potential, large parentheses denote Wigner's 3j symbols, $\phi_{LM} = \int \mathrm{d}^2\hat{\mathbf{n}}\, Y^*_{LM}(\hat{\mathbf{n}})\,\phi(\hat{\mathbf{n}})$ is the harmonic expansion of the lensing potential, L and M are indices of the potential expansion modes, and $W^{\phi}_{\ell_1\ell_2 L}$ is the weight function given in [131].

The quadratic estimator of the lensing potential for the covariance search, which takes contamination from point-like sources into account, is constructed in the form

$$\hat{\phi}^X_{LM} = \sum_{L'M'}\left(\mathfrak{R}^{x\phi}\right)^{-1}_{LM,\,L'M'}\left(\hat{X}_{L'M'} - X^{MF}_{L'M'}\right), \quad (28)$$

where $\mathfrak{R}^{x\phi}$ is the normalization matrix, $\hat{X}_{LM}$ is the quadratic 'building block' calculated from two filtered sky maps $\hat{T}^{(1)}_{\ell m}$ and $\hat{T}^{(2)}_{\ell m}$ by adding their empirical covariance matrices, and the mean field term $\hat{X}^{MF}_{LM}$ includes all known sources of statistical anisotropy on the map that could shift the lensing level estimate. The algorithms for constructing and computing $\mathfrak{R}^{x\phi}$, $\hat{X}_{LM}$, and $\hat{X}^{MF}_{LM}$ are presented in [131]. We note that the calculation of the lensing potential and the potential power spectrum (which is also presented in the cited paper) was checked by Monte Carlo simulations.

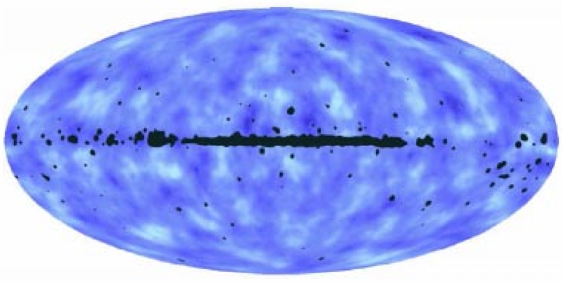

Figure 27. (Color online.) The lensing potential map after applying the Wiener filter with a minimal mask superimposed to reconstruct the NILC. The map is limited to harmonics in the range $8 \leqslant L \leqslant 2048$ (the multipole notation L is conventionally used for maps and the power spectrum of the potential). (From [11].)

The lensing potential map from [139] is shown in Fig. 27. Its power spectrum is presented in Fig. 28.

The gravitational lensing tests enable not only constraining cosmological ΛCDM parameters, such as $\Omega_{\mathrm{b}}h^2$, n_{s}, A_{s}, $\Omega_{\mathrm{CDM}}h^2$ (see also Table 4 in Section 6.3.4), but also independently estimating the parameters Ω_{m}, H_0, and σ_8. Results of the likelihood function method for gravitational lensing tests are presented in Fig. 29. The contours in this figure show the range of admissible values of the Hubble constant, which demonstrates the consistency of the tests. The contour crossing implies the reliability of determination of the admissible parameters on the $\Omega_{\mathrm{m}} - \sigma_8$ plane. We note that this test involves the relation

$$\sigma_8\Omega_{\mathrm{m}}^{0.25} = 0.591 \pm 0.021\,. \quad (29)$$

This combination of parameters is measured with an accuracy of about 3.5% [139]. A detailed discussion of the possibilities for the power spectrum and the relation between parameters in (29) is given in Appendix E of [139].

The main results on CMB gravitational lensing presented by the Planck collaboration [139], in addition to the map and power spectrum of the lensing potential, are as follows:

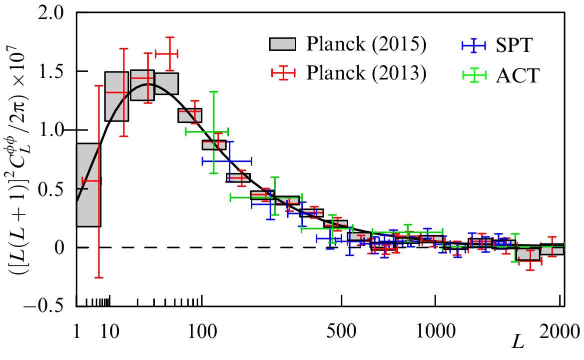

Figure 28. (Color online.) Power spectrum of the lensing potential reconstructed with the use of the MV estimator from the Planck 2015 data. Shown also are the reconstructions from the Planck 2013 data [131], ACT [146], and SPT [150]. The solid line is the fiducial ΛCDM spectrum. (From [139].)

Table 4. Parameters of the cosmological ΛCDM model calculated from the likelihood ratios using the Planck 2015 data in combination with different tests.* (Table 3 in [117].)

Parameter	1	2	3	4	5
	TT + lowP	TE + lowP	EE + lowP	TT, TE, EE + lowP	$(\sigma_1 - \sigma_4)/\sigma_1$
$\Omega_b h^2$	0.02222 ± 0.00023	0.02228 ± 0.00025	0.0240 ± 0.0013	0.02225 ± 0.00016	− 0.1
$\Omega_{\rm CDM} h^2$	0.1197 ± 0.0022	0.1187 ± 0.0021	$0.1150^{+0.0048}_{-0.0055}$	0.1198 ± 0.0015	0
$100\theta_{\rm MC}$	1.04085 ± 0.00047	1.04094 ± 0.00051	1.03988 ± 0.00094	1.04077 ± 0.00032	0.2
τ	0.078 ± 0.019	0.053 ± 0.019	$0.059^{+0.022}_{-0.019}$	0.079 ± 0.017	− 0.1
$\ln(10^{10} A_s)$	3.089 ± 0.036	3.031 ± 0.041	$3.066^{+0.046}_{-0.041}$	3.094 ± 0.034	− 0.1
n_s	0.9655 ± 0.0062	0.965 ± 0.012	0.973 ± 0.016	0.9645 ± 0.0049	0.2
H_0	67.31 ± 0.96	67.73 ± 0.92	70.2 ± 3.0	67.27 ± 0.66	0
Ω_m	0.315 ± 0.013	0.300 ± 0.012	$0.286^{+0.027}_{-0.038}$	0.3156 ± 0.0091	0
σ_8	0.829 ± 0.014	0.802 ± 0.018	0.796 ± 0.024	0.831 ± 0.013	0
$10^9 A_s \exp(-2\tau)$	1.880 ± 0.014	1.865 ± 0.019	1.907 ± 0.027	1.882 ± 0.012	− 0.1

* $\Omega_b h^2$ is the physical baryon density; $\Omega_{\rm CDM} h^2$ is the physical density of dark matter; $100\theta_{\rm MC}$ is the approximation of the CMB acoustic scale in the CosmoMC procedure increased 100-fold, which is equal to $r_*/D_{\rm A}$ (the ratio of the comoving horizon size in the epoch z_* when the optical depth is equal to unity relative to the angular-diameter distance); τ is the Thomson optical depth due to reionization; $\ln(10^{10} A_s)$ is the logarithm of the primordial isocurvature perturbations; n_s is the spectral exponent of the scalar mode power spectrum; H_0 is the Hubble constant, the current expansion rate of the Universe; Ω_m is the matter density in units of the critical density; σ_8 is the rms fluctuations at the present time in the linear theory; and $10^9 A_s \exp(-2\tau)$ is an additional combined parameter.

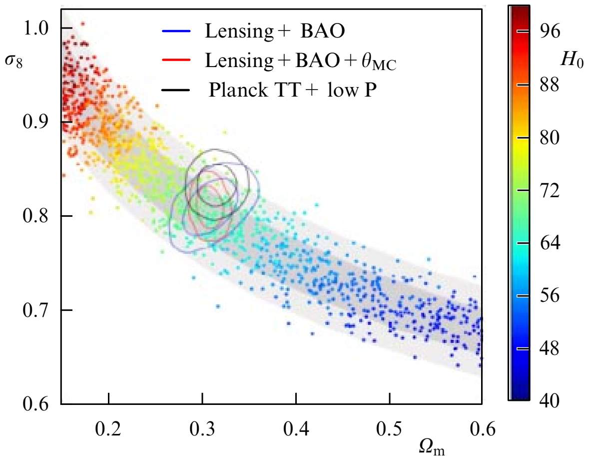

Figure 29. (Color online.) Likelihood functions for determining the ΛCDM parameters using the CMB lensing data alone are shown by gray bands corresponding to the 1σ and 2σ constraints [see Eqn (29)]. The solid colored contours show the 68% and 95% constraints when additional information is included: the baryon acoustic oscillation (BAO) data from optical SDSS and 3DF surveys [151–153] (blue); the same data but with the acoustic scale parameter fixed as $\theta_{\rm MC} = 1.0408$ (red); and using the Planck TT low-P polarization data (black). The symbols are color-coded by the value of the Hubble constant H_0. (From [139].)

- the B-mode lensing in the Planck data is discovered with a 10σ significance from cross-correlation with the cosmic infrared background as a factor that traces the lensing potential, as well as from the CMB trispectrum TTEB; this confirms the sensitivity of the Planck instruments to known sources of the B-mode at intermediate and small scales;
- the three-point correlation function (bispectrum) is measured from the CMB data with an improved accuracy; this correlation function is due to a correlation between the lensing potential and the integral Sachs–Wolfe (ISW) effect, whose origin in the last epoch is the accelerating expansion of the Universe; the lensing and the ISW bispectrum demonstrate the effect at the 3σ level;
- the use of only lensing information allows the likelihood function construction for the combination parameters $\sigma_8 \Omega_m^{0.25}$ with an accuracy of up to 3.5%.

Therefore, lensing, as one of the additional cosmological tests, significantly increases the potential of the Planck data over the WMAP data.

6.3.4 Cosmological parameters. Table 4 shows the cosmological parameters inferred from the 2015 Planck data release using the power spectrum of the CMB temperature anisotropy and polarization in combination with different tests. Column 1 shows the parameters inferred from the TT-spectra at low and high multipoles. Columns 2 and 3 shows the results as derived from the TE- and EE-spectra only at high multipoles with polarization at low multipoles (lowP). Column 4 presents the parameters obtained with the likelihood function calculation from all the available data. Column 5 lists deviations of the cosmological parameters obtained with the likelihood functions calculated for TT + lowP and TT, TE, EE + lowP spectra. The corresponding likelihood functions with confidence regions are presented in Fig. 30.

We note the difference in values of some frequently used parameters and the measurement results in the Planck 2015 [117], Planck 2013 [118], and WMAP9 [8] data. Table 5 shows both the base model parameters and parameters of the extended cosmological model for the three CMB data releases. The most frequently used additional parameters of the extended ΛCDM models include: the density parameter determined by the curvature ($\Omega_K = 1 - \Omega_0$), the effective number of neutrino types $N_{\rm eff}$, the total mass of the standard neutrinos $\sum m_\nu$, the helium contribution to the baryonic

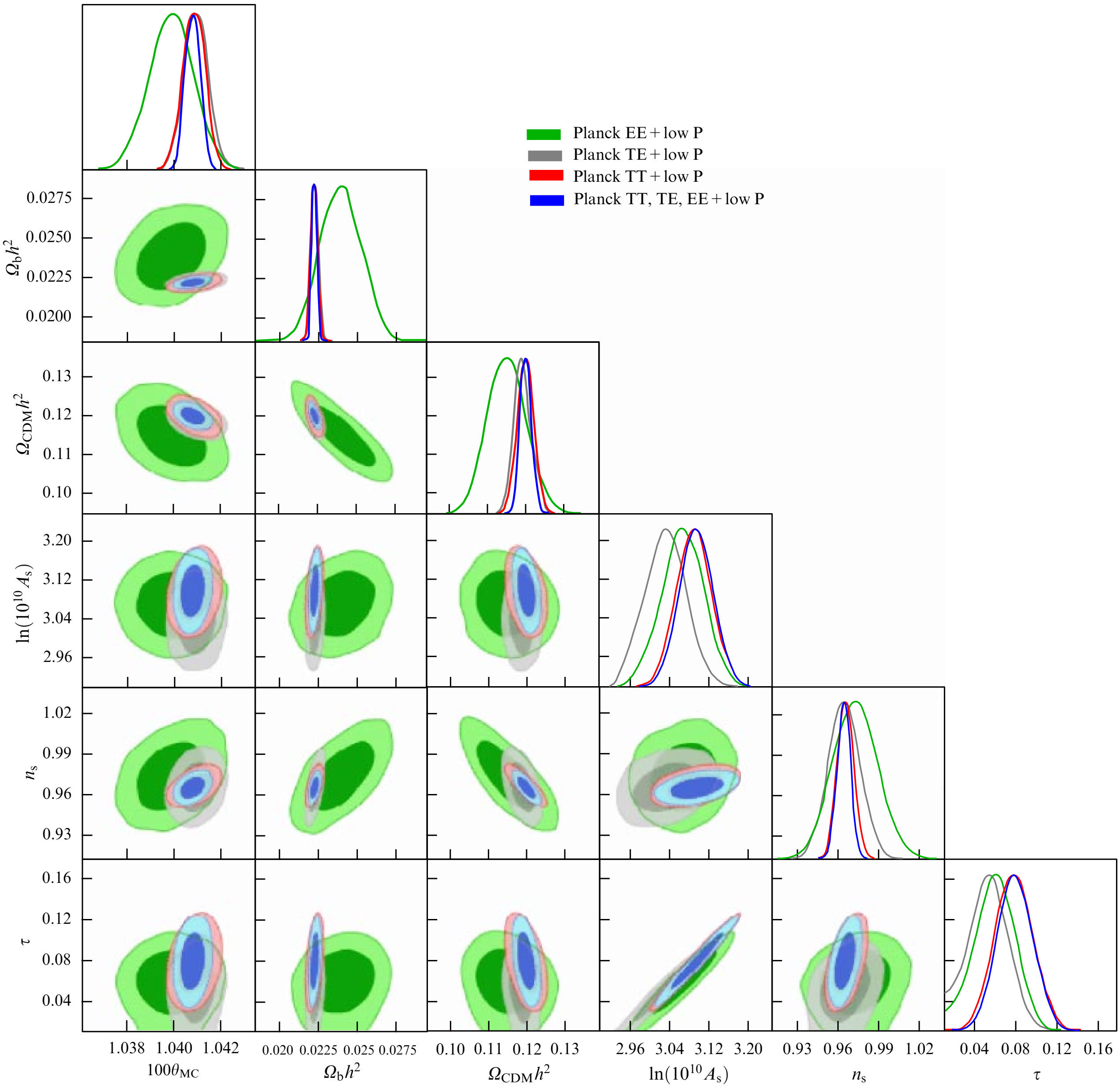

Figure 30. (Color online.) Likelihood functions in the base ΛCDM model for pairs of cosmological parameters according to the Planck temperature anisotropy and polarization data. (From [117].)

density N_{eff}, the tensor-to-scalar-mode ratio $r_{0.002}$, and the parameter of dynamic dark energy w in the equation of state. The presented results are obtained using both internal experimental data and a model consistent with other experiments.

We note that the use of CMB fluctuation data to infer the properties of neutrinos is quite natural. The basic ΛCDM model used by the Planck collaboration assumes the normal neutrino mass hierarchy with $\sum m_\nu \approx 0.06$ eV but with a possible violation of the mass hierarchy with $\sum m_\nu \gtrsim 0.1$ eV. The possibility of testing this hypothesis motivated the analysis of the neutrino properties from the CMB data. In addition, the nonzero mass of neutrinos enables decreasing σ_8 to bring the Planck mission results to agreement with data on weak lensing and rich cluster abundance. The likelihood functions for the parameter pairs are shown in Fig. 31.

6.4 Inflation

The precise measurements of temperature and polarization in the Planck experiment have allowed estimating the parameters of admissible inflationary models (such as n_s, $dn_s/d\ln k$, and $r_{0/002}$) [154]. In 2014, it was reliably established in [155] (at a confidence level $> 5\sigma$) that there are deviations of the scalar spectral exponent from the one corresponding to an exact scalar invariant: it was found that $n_s < 1$, and further data were required to determine the running exponent. Nevertheless, the measured values and bounds favored simple slow-roll inflationary models. Inflationary models with one field and the standard kinetic term also fitted the new bounds on the non-Gaussianity parameter f_{NL} obtained in [118]. No evidence was found for the isocurvature perturbations generated in multi-field inflationary models or by cosmic strings and topological defects [155, 156]. The Planck 2013 results have renewed interest in some

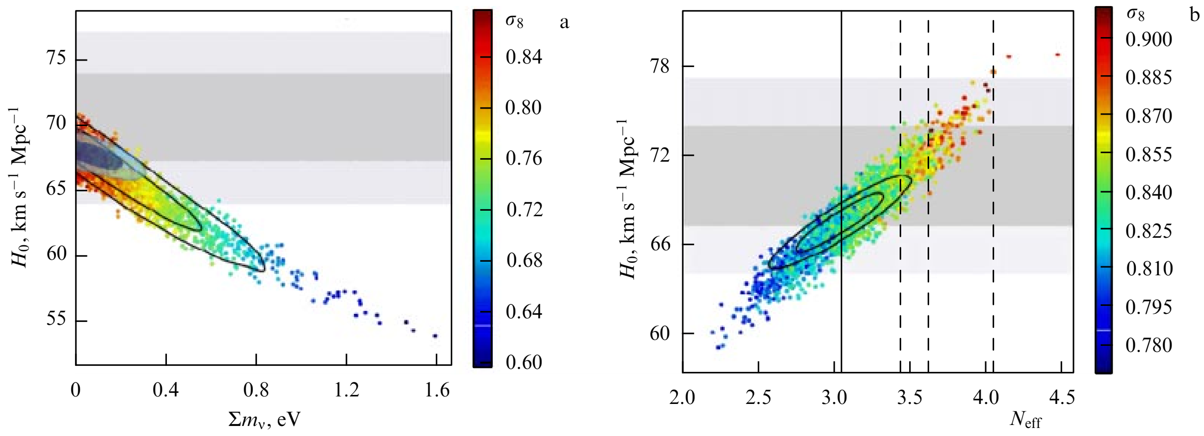

Figure 31. (Color online.) (a) The $H_0 - \sum m_\nu$ plane from the Planck TT + low P data. Color-coded are the σ_8 matter fluctuations. Higher $\sum m_\nu$ damp σ_8, but also decrease H_0. The black solid contours show the constraints from Planck TT + lowP + lensing. The filled contours show the constraints from the Planck TT + lowP + lensing + BAO data. (b) $H_0 - N_{\rm eff}$ diagram from the Planck TT + lowP data. Grey bands show direct measurements of $H_0 = 70.6 \pm 3.3$ km s^{-1}Mpc^{-1}. Higher $N_{\rm eff}$ brings H_0 into better consistency with direct measurements but increases σ_8. Solid black contours show the constraints from the Planck TT, TE, EE + lowP + BAO data. Models with $N_{\rm eff} < 3.046$ (left of the solid vertical line) require photon heating after the neutrino decoupling or incomplete thermalization. Dashed vertical lines correspond to specific fully thermalized particle models, for example, one additional massless boson that decouples at around the same time as the neutrinos ($\Delta N_{\rm eff} \approx 0.57$) or before the muon annihilation ($\Delta N_{\rm eff} \approx 0.39$), or an additional sterile neutrino that decouples at around the same time as the active neutrinos ($\Delta N_{\rm eff} \approx 1$). (From [117].)

Table 5. Standard cosmological ΛCDM parameters inferred from the Planck 2015, Planck 2013, and WMAP9 data. Some parameters of the extended model are also presented.*

Base model					
Parameter	Planck 2015		Planck 2013		WMAP9 2012
	TT + lowP	TT + TE + EE + lowP + lens + ext	TT	Planck + WP + highL + BAO	WMAP + eCMB + BAO + H_0
H_0	67.31 ± 0.96	67.71 ± 0.46	67.4 ± 1.4	67.80 ± 0.77	69.32 ± 0.80
Ω_Λ	0.685 ± 0.013	0.6811 ± 0.0062	0.686 ± 0.020	0.692 ± 0.010	$0.7135^{+0.0095}_{-0.0096}$
$\Omega_{\rm m}$	0.315 ± 0.013	0.3089 ± 0.0062	0.314 ± 0.020	0.308 ± 0.010	0.2830 ± 0.0097
$z_{\rm re}$	$9.9^{+1.8}_{-1.6}$	$8.8^{+1.2}_{-1.1}$	$11.4^{+4.9}_{-2.8}$	11.3 ± 1.1	10.1 ± 1.0
Age of the Universe	13.813 ± 0.038	13.799 ± 0.021	13.813 ± 0.058	13.798 ± 0.037	13.772 ± 0.059
$n_{\rm s}$	0.9655 ± 0.0062	0.9667 ± 0.0040	0.9616 ± 0.0094	0.9608 ± 0.0054	0.9608 ± 0.0080
σ_8	0.829 ± 0.014	0.8159 ± 0.0086	0.834 ± 0.027	0.826 ± 0.012	$0.820^{+0.013}_{-0.014}$

Extended model					
Parameter	Planck 2015		Planck 2013		WMAP9 2012
	TT	TT + TE + EE + lens + ext	Planck + WP	Planck + WP + highL + BAO	WMAP + eCMB + BAO + H_0
Ω_K	$-0.052^{+0.049}_{-0.055}$	$0.0008^{+0.0040}_{-0.0039}$	$-0.037^{+0.043}_{-0.049}$	$-0.0005^{+0.0065}_{-0.0066}$	$-0.0027^{+0.0039}_{-0.0038}$
$\sum m_\nu$, eV	< 0.715	< 0.194	< 0.933	< 0.230	< 0.44
$N_{\rm eff}$	$3.13^{+0.64}_{-0.63}$	$3.04^{+0.33}_{-0.33}$	$3.51^{+0.80}_{-0.74}$	$3.30^{+0.54}_{-0.51}$	3.26 ± 0.35
Y_P	$0.252^{+0.041}_{-0.042}$	$0.249^{+0.025}_{-0.026}$	0.24771 ± 0.00014	$0.257^{+0.038}_{-0.040}$	$0.308^{+0.032}_{-0.031}$
$\mathrm{d}n_{\rm s}/\mathrm{d}\ln k$	-0.008 ± 0.016	-0.002 ± 0.013	$-0.013^{+0.018}_{-0.018}$	$-0.014^{+0.016}_{-0.017}$	-0.023 ± 0.011
$r_{0.002}$	< 0.103	< 0.113	< 0.120	< 0.111	< 0.13
w	$-1.54^{+0.62}_{-0.52}$	$-1.019^{+0.075}_{-0.080}$	$-1.49^{+0.65}_{-0.57}$	$-1.13^{+0.23}_{-0.25}$	$-1.037^{+0.071}_{-0.070}$

* The results are derived both from internal data of the experiments and in the model consistent with other experiments. Abbreviations used: lens — lensing data, ext — use of additional tests of the CMB data, WP — polarization WMAP data, eCMB — additional data on the CMB from other experiments.

aspects of inflationary models, both conceptual [157–160] and specific, such as, for example, Starobnsky's R^2 inflationary model [161]. The model predicts cosmological fluctuations [161, 162] consistent with the Planck 2013 results [155]. The R^2 model corresponds to the potential

$$V(\phi) = \Lambda^4 \left[1 - \exp\left(-\sqrt{\frac{2}{3}}\,\frac{\phi}{M_{\rm Pl}}\right)\right]^2 , \tag{30}$$

which leads to the slow-roll model predictions and gives $n_{\rm s} - 1 \approx -2/N$ and $r \approx 12/N^2$. Additional interest in the problem appeared after the publication of the results of the BICEP2 experiment at the South Pole [163, 164]. This experiment covered a 380 sq. deg sky field. The BICEP2 team suggested that the signal discovered by them in the polarization B-mode in the multipole range $50 < \ell < 150$ at 150 GHz is due to primordial gravitational waves [165–170]. The effect of polarized warm dust in our Galaxy was assumed to be excluded using the dust emission models. Under these assumptions, BICEP2 derived the tensor-to-scalar-mode ratio $r = 0.2^{+0.07}_{-0.05}$ for the scalar invariant perturbation spectrum. The BICEP2 team presumed that the value $r = 0.2$ changed the Planck mission hypothesis favoring slow-roll inflation models: such a high value of r required a high running exponent or another modification of the simple power-law spectrum of perturbations to bring the contribution from gravitational waves to the temperature anisotropy at low multipoles in agreement with the observed TT-spectrum. But analysis of the dust polarization data at 353 GHz called the BICEP2 conclusions into doubt [99, 100, 155, 171].

The Planck measurements determined the frequency dependence of the galactic dust emission intensity and polarization. It was found that the polarization fraction is higher than expected in low-intensity regions. In this case, the interpretation of the polarization B-mode as a sum of signals from the primordial tensor mode and lensing is not statistically preferable to the expected dust emission at 150 GHz with a lensing contribution.

In [62], the polarization B-mode power spectrum built from the dust polarization data at 353 GHz in the multipole range $40 < \ell < 120$ was extrapolated to the 150 GHz band. The extrapolation demonstrated that the B-mode signal discovered by BICEP2 can be fully accounted for by dust emission. A recent joint analysis of high-sensitive BICEP2/Keck Array and Planck data [172] confirmed that the dust dominates. Cross-correlation of all maps in the BICEP2 field did not reveal a statistically significant signal from the primordial gravitational waves and set an upper bound $r < 0.12$ at the 95% confidence level. Although this upper bound is numerically almost identical to the Planck 2013 result inferred from the combination of the Planck temperature maps and WMAP polarization data [118, 155], this upper bound is more stable to modifications of inflationary models, because the B-mode is insensitive to the form of the predicted pattern describing the scalar anisotropy.

Using the Planck 2015 temperature and polarization full-sky CMB data, new estimates of the spectral slope and running exponent, $n_{\rm s} = 0.968 \pm 0.006$ and $\mathrm{d}n_{\rm s}/\mathrm{d}\ln k = -0.003 \pm 0.007$, were obtained in [154] using the likelihood function method in combination with the Planck lensing data. With polarization data at high multipoles taken into account, a new upper bound on the tensor-to-scalar ratio has been derived, $r_{0.002} < 0.11$ at the 95% confidence level, which is in agreement with the results of the joint BICEP2/Keck and Planck data analysis [172]. This result assumes the inflation potential $V(\phi) \propto \phi^2$, and the natural inflation is less favorable than in models predicting smaller tensor-to-scalar ratio, such as the R^2-inflation.

The primordial power spectrum was reconstructed using three independent methods, which reproduce a smooth spectrum without peculiarities, $\mathfrak{P}_{\mathfrak{R}}(k)$, in the scale range $0.008 \lesssim k \lesssim 0.1$ Mpc^{-1}. At larger scales, a deviation from the power law is discovered due to the signal deficit in the temperature anisotropy power spectrum at $\ell \approx 20-40$, but within the cosmic variance. By combining power-spectrum and non-Gaussianity bounds, the authors of [154] constructed models with generalized Lagrangians, including a Galileon model and an axion monodromy model. The Planck data are consistent with the hypothesis of adiabatic primordial perturbations, and the obtained estimates of parameters of the main initial conditions are consistent within this hypothesis. For correlated mixed adiabatic models and models with constant curvature, the respective upper bounds on the nonadiabaticity contribution to the CMB temperature variations at the 95% confidence level are $|\alpha_{\text{non-adi}}| < 1.9\%$, 4%, and 2.9% for cold dark matter, neutrino density, and constant-curvature modes for the neutrino velocity. Inflationary models leading to an anisotropic modulation of the primordial curvature power spectrum were tested and it was shown that the dipole modulation in the CMB temperature field caused by constant-curvature cold dark matter perturbations is not favored at a statistically significant level. The Planck 2015 results from all available observational data are consistent with the Planck 2013 results and single-field slow-roll inflationary models. A comparison of the likelihood functions for different inflationary models in the $r_{0.002} - n_{\rm s}$ diagram are shown in Fig. 32.

6.5 Search for non-Gaussianity

One of the most important tests of the inflation theory consists in testing the Gaussianity of the CMB signal (see, e.g., review [28]). The standard parameterization of the non-Gaussianity level is in terms of the coefficient $f_{\rm NL}$ determined from the bispectrum. We recall that the simplest and best-studied quantity in which the non-Gaussianity of CMB fluctuations can show up is the three-point correlation function or its harmonic analog, the bispectrum

$$\langle a_{\ell_1 m_1} a_{\ell_2 m_2} a_{\ell_3 m_3} \rangle \, . \tag{31}$$

The bispectrum is very sensitive to certain forms of non-Gaussianity, which are considered standard and include the so-called local form obtained under the assumption that the primordial fluctuations have a local nonlinearity in the coordinate space [115]:

$$\Phi(x) = \Phi_{\rm L}(x) + f_{\rm NL}\left(\Phi_{\rm L}^2(x) - \left\langle \Phi_{\rm L}^2(x) \right\rangle\right) , \tag{32}$$

where $\Phi_{\rm L}(x)$ is a linear Gaussian field, $\langle \Phi_L(x) \rangle = 0$, and $f_{\rm NL}$ is a constant describing the nonlinearity in the form of a quadratic correction to the gravitational potential (curvature) perturbations. The 'equilateral' $f_{\rm NL}^{\rm equil}$ [173] and 'orthogonal' $f_{\rm NL}^{\rm ortho}$ [174] non-Gaussianity forms are also considered 'standard'.

The non-Gaussianity amplitude $f_{\rm NL}$ of the Planck CMB bispectrum was measured in [175]. The non-Gaussianity was analyzed using three bispectrum estimators (fitted by separable templates, binned, and modal). The estimators were

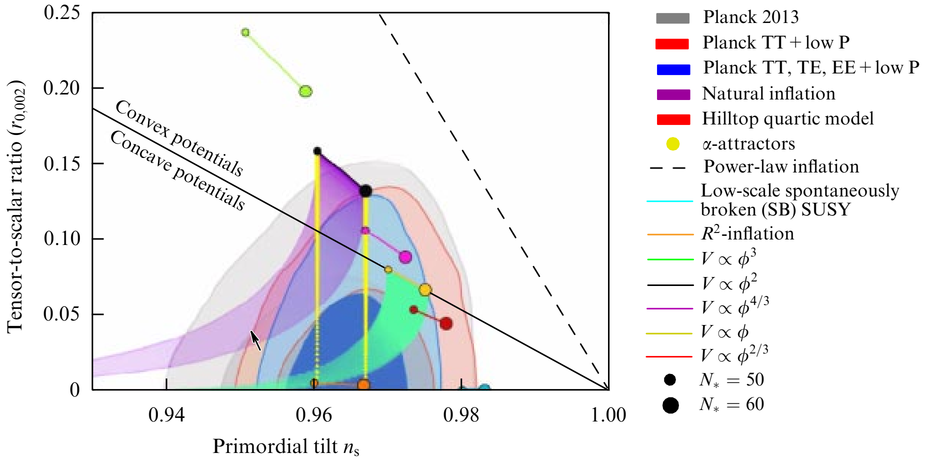

Figure 32. (Color online.) 68% and 95% confidence regions of the likelihood function on the $r_{0.002} - n_s$ plane from the Planck 2015 data in combination with other cosmological data sets compared to the theoretical predictions of selected inflationary models. N_* is the number of e-foldings. (From [154].)

applied to the Planck 2015 full-sky temperature anisotropy and E-polarization maps reconstructed by four component separation methods: SMICA, SEVEM, NILC, and Commander. On the maps, masks were used to filter intervening structures, such as bright galactic regions or powerful point-like sources, and 70% of the full sky was studied.

The analysis resulted in the following consistent non-Gaussianity parameters (after taking the Bayesian offset caused by lensing and the Sachs–Wolfe effect into account): $f_{\rm NL}^{\rm equil} = -16 \pm 70$, $f_{\rm NL}^{\rm ortho} = -34 \pm 33$ if only temperature anisotropy maps were used, and $f_{\rm NL}^{\rm equil} = -3.7 \pm 43$, $f_{\rm NL}^{\rm ortho} = -26 \pm 21$ at the 68% confidence level if both temperature and E-polarization data were used. The local non-Gaussianity level is $f_{\rm NL}^{\rm local} = 2.5 \pm 5.7$ according to the T-data and $f_{\rm NL}^{\rm local} = 0.8 \pm 5.0$ using joint T- and E-data (68% confidence level). From the likelihood function for $f_{\rm NL}$ by which the regime of small primordial non-Gaussianity is probed, estimates of the sound speed limits during inflaton fluctuations or other microscopic oscillations in the inflation models can be derived [176]. The constraints on the sound speed are then used in combination with the angular power spectrum.

We note that the non-Gaussianity level estimates were obtained in the framework of a certain method enabling inflationary model studies. Besides the bispectrum, non-Gaussianity can appear in the Planck data as violations of the statistical isotropy of the signal, the most prominent of them being classified as CMB anomalies.

6.6 BICEP2 and Planck results

We now discuss the BICEP2/Keck experiment separately. BICEP2 was a dedicated low-angular-resolution experiment (the telescope aperture is 26 cm, the resolution is 0.52°) carried out at the South Pole in 2010–2012 at 150 GHz with a sensitivity comparable to that of the Planck instruments at high galactic latitudes. A TES (Transition Edge Sensor) bolometer consisting of 512 sensors was installed in the focal plane of the telescope. The BICEP2 collaboration presented the results in [163, 164], where the polarization B-mode is reported to significantly exceed the expected level in the ΛCDM model with $r = 0$ with lensing taken into account in the multipole range $30 < \ell < 150$. Although the CMB lensing due to galaxy clusters, which distorts only the B-mode, is significant only at small scales, its contribution was taken into account in the component separation procedure. The dust contribution estimated from the previous BICEP1 measurements and WMAP maps was thought to be insignificant at high galactic latitudes. The data analysis resulted in an excess of the polarization B-mode emission on degree and sub-degree scales (Fig. 33). This, in principle, suggested a new effect observed in the B-mode at 150 GHz. The authors interpreted the excess as a cosmological signal, namely, as a result of the presence of primordial gravitational waves. The detected signal implies a larger contribution to the CMB anisotropy than followed from the WMAP data and Planck data on the CMB temperature fluctuations published by that time. The discovery entailed complications with theoretical models. On the other hand, it could be assumed that the detected signal contained some additional emission component that was not taken into account in single-frequency experiments such as BICEP2.

Already in April 2014, Liu et al. from the Niels Bohr Institute published paper [177], where they discussed the effect of magnetized dust on the polarization B-mode signal at high galactic latitudes. The emission from this cold dust component consisting of microscopic elongated dust grains with inclusion of metals additionally contributes to the polarized foreground. Such clouds are found in supernova remnants with relatively strong magnetic fields, which leads to polarized emission generation. Angular scales in the sky on which such an emission can be detected are very large: for example, the North Galactic Spur formed by supernova remnants is observed as an anomalous band on the synchrotron radiation map extending from the north galactic pole to almost middle latitudes in the southern hemisphere. The integral emission on such scales exactly contributes on the scales of a few degrees and tens of degrees. As noted in [177], observations at the South Pole in the Antarctic in the BICEP2 experiment could study exactly the sky fields that contain such charged dust. Later, the idea that the B-mode excess on degree scales could be related to the charged dust was also checked in [178, 179]. The Planck collaboration paper [180] devoted to this issue appeared in the second half of September 2014. Unlike BICEP2, the Planck mission observed the linear polarization by four bolometric detectors at 100, 143, 217, and 353 GHz. This enabled various emission components with different spectral exponents and brightness to be taken into account at different angular scales. Contributions from different sky fields with a different level of screening of

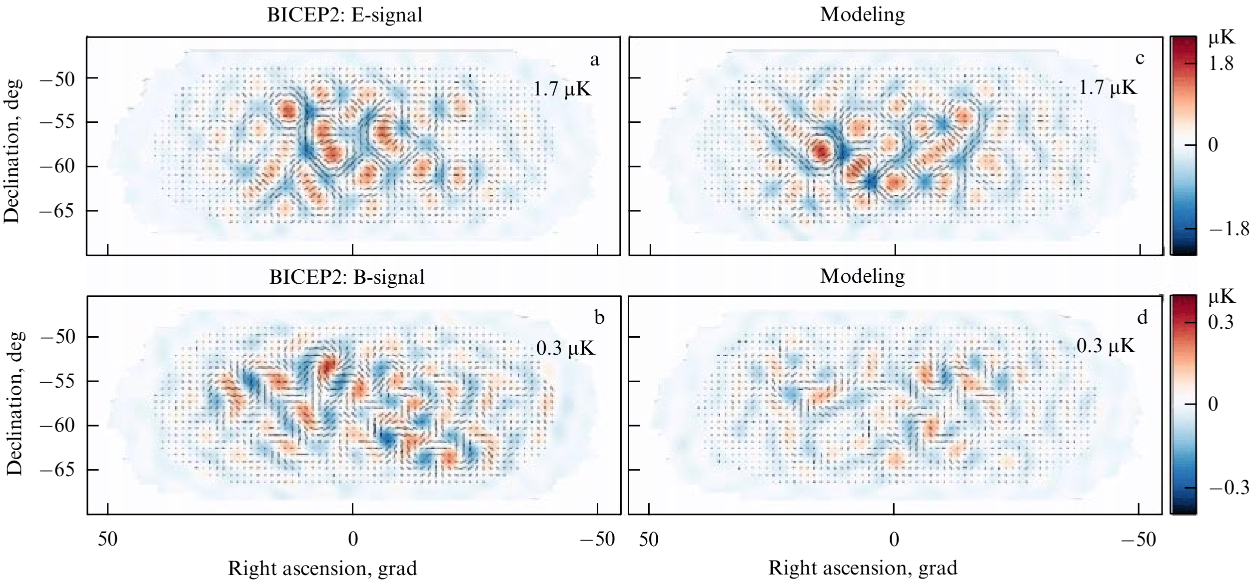

Figure 33. (Color online.) (a) E-mode and (b) B-mode polarization maps in the BICEP2 experiment. The equivalent maps in the lensed-ΛCDM + noise simulations for (c) E-mode and (d) B-mode. The maps are filtered to $50 < \ell < 120$. The excess B-mode signal is detected over lensing + noise ($S/N > 2$ at $\ell \sim 70$). (From [164].)

intervening zones of our Galaxy were estimated in [180]. Emission models (power spectra) were constructed with improved contributions from the galactic components at different angular scales. One section of the paper was devoted to the polarization B-mode emission in the field observed by BICEP2. In particular, the polarization B-mode power spectra constructed from the Planck data at 353 GHz in circle domains of the CMB maps with an area of 400 sq. deg at high galactic latitudes were extrapolated to the 150 GHz frequency band (as in the BICEP2 experiment). The highest frequency was chosen because the polarization effects are more prominent at high frequencies. With overlapping spectral bands, it is not difficult to interpolate data at intermediate frequencies. A thorough analysis of all possible contributions at different galactic latitudes and angular scales led to the following conclusions:

- the power spectra extrapolation shows that at high galactic latitudes, there is a significant dust contamination on scales that are most interesting for primordial gravitational wave studies;
- the polarized dust has a power spectrum with significant amplitude dispersion, and using the Planck data alone is not sufficient to precisely choose the polarized sky fields absolutely free of dust contamination;
- in the BICEP2 field study on degree and subdegree scales (harmonics $40 < \ell < 120$), the extrapolation of the spectrum to 150 GHz yields 1.32×10^{-2} μK^2 with a statistical uncertainty of $\pm 0.29 \times 10^{-2}$ μK^2, which is comparable to the BICEP2 measurements at the given angular scales;
- the frequency dependence of the B-mode power spectra corresponds to the expected polarized dust emission;
- there are regions in the sky where the polarization dust emission is two times lower than that registered in the BICEP2 experiment (Fig. 34).

After [180], paper [172] presenting the results of the joint Planck and BICEP2 data analysis appeared, reporting the upper bound on the tensor-to-scalar-mode ratio $r < 0.12$ at the 95% confidence level.

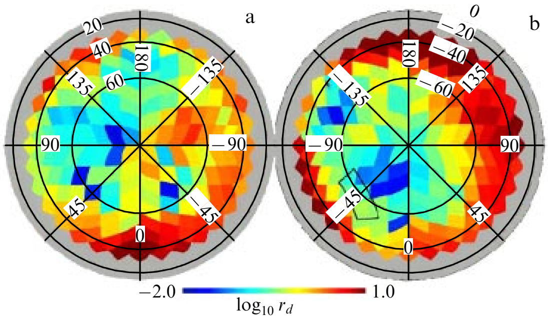

Figure 34. (Color online.) Maps of the $D_\ell^{\rm BB}$ amplitude with $\ell = 80$ at 150 GHz in the orthographic projection for the (a) northern and (b) southern galactic hemispheres. The maps are computed from the Planck 353 GHz data. The color presents the estimated contamination from dust in units $r_{\rm d}$, the ratio of the dust emission power spectrum amplitude to the $D_\ell^{\rm BB}$ amplitude of the primordial tensor mode for $r = 1$ at $\ell = 80$, corresponding to 6.71×10^{-2} μK^2. For example, $r_{\rm d} = 0.1$ means that the expected dust contamination at the $\ell = 80$ scale is equal to the primordial tensor mode CMB amplitude $D_\ell^{\rm BB}$ for $r = 0.1$. The black contour outlines the BICEP2 deep-field region. (From [180].)

6.7 Geometry and topology

Special papers are devoted to the geometric and topological properties of the Universe that could be inferred from the CMB maps [156, 181–184]. Using the observational data and the model CMB signal in different topologically multi-connected time–space universes, the authors rejected many multi-connected models of the Universe with flat, hyperbolic, and spherical geometry. In addition, the Planck data were shown to be unable to reliably test correlations that would be present in the case of a nontrivial topology, like a Universe in the shape of a dodecahedron or a cubic torus.

There are no confirmations of the physically anisotropic expansion of the Universe that could be described by the Bianchi models, although a template corresponding to the Bianchi VII$_h$ model [182, 184] can be constructed from the

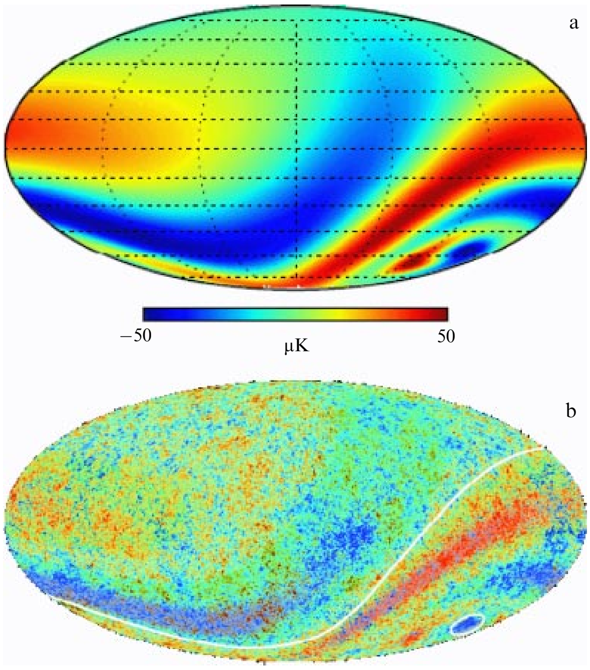

Figure 35. (Color online). (a) CMB in the Bianchi VII$_h$ anisotropic cosmological model. (b) The CMB map with the model signal superimposed.

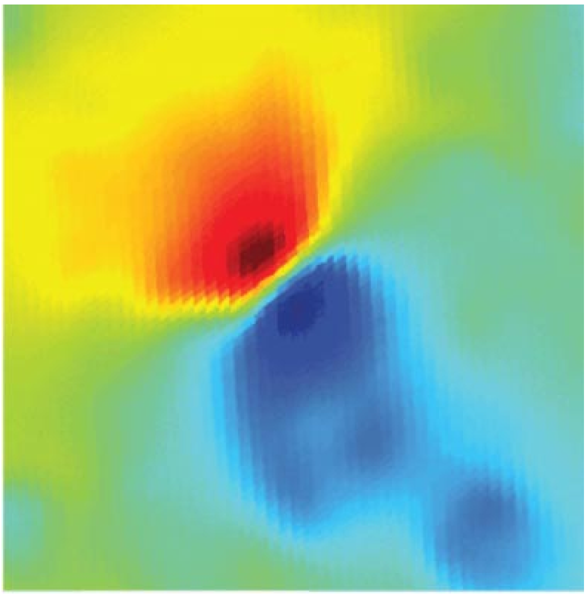

Figure 36. (Color online.) Characteristic discontinuity in the CMB temperature produced by a cosmic string. A Nambu–Goto string produces a cusp — a small region on the string that moves almost at the speed of light and generates the local CMB signal. (From [156].)

CMB maps. The interest in this model is maintained by its correspondence to three anomalies to be discussed in Section 7: the galactic north–south asymmetry in the power spectrum, the Axis of Evil, and the Cold Spot. The CMB anisotropy in this model is shown in Fig. 35. The fitting and analysis of this Bianchi-type anisotropic model were done using the Bayesian approach. If no physical assumptions are made and the Bianchi-type and standard cosmology are analyzed separately, the Planck CMB temperature anisotropy data corresponds to the Bianchi model with the Bayesian factor 2.3 in logarithmic units [184]. In the joint analysis with the inclusion of the standard cosmological model parameters, the Planck temperature and polarization data would require the amplitude -0.1 ± 0.04 compared to $+1$ if the Bianchi VII$_h$ model were real. For the vorticity parameter that can be applied to describe this model, the upper bound is $w/H_0 < 7.6 \times 10^{-10}$ at the 95% confidence level. In other words, the cosmological parameters with which this template could be generated on the map are inconsistent with the Planck measurements.

The Planck data enabled imposing upper bounds on the CMB fluctuations due to topological defects. The possibility of detecting topological defects in the form of cosmic strings — very massive, extended, and extremely thin formations that could survive from the Big Bang epoch — was discussed in [156]. The cosmic strings can have a huge energy density μ per unit length, which should lead to various observational effects, including gravitational lensing and background gravitational waves. The Planck studies concentrate on the string effects on the CMB maps, which generate peculiarities like linear disruptions in the temperature distribution (Fig. 36).

Effects comparable in amplitude could also be generated by other cosmological defects, for example, by semi-local strings and global textures. Each type of cosmological defect affects the CMB power spectrum and produces a specific non-Gaussianity on the CMB maps. These signatures can be used to separate various topological defects from other possible sources of the CMB anisotropy and systematic effects. Nambu–Goto strings and field theory strings with strong radiative effects were studied in [156]. Numerical simulations of cosmic strings using the Nambu–Goto action show that their cosmological appearances are scale-invariant, and several dozen long strings extended across each considered volume inside the horizon could be observed. These strings are continuous sources of gravitational perturbations inside the horizon, and the amplitude of perturbations is determined by the dimensionless parameter $G\mu/c^2 = (\eta/m_{\rm Pl})^2$, where η is the energy scale of the phase transition during string formation and $m_{\rm Pl}$ is the Planck mass.

The search for characteristic non-Gaussianities in the CMB fluctuations expected from cosmic strings yielded the upper bounds $G\mu/c^2 < 8.8 \times 10^{-7}$ from the bispectrum and $G\mu/c^2 < 7.8 \times 10^{-7}$ using the Minkowski functional. In fact, no signatures of cosmic strings have been found in the Planck data.

6.8 Variations of physical constants

Experimental measurements of possible variations of physical constants have been carried out in astrophysical studies for a long time (see, e.g., [185]). They can be performed using observations of absorption lines in quasar spectra, of first-generation stars, and of molecular absorption lines. Primordial nucleosynthesis data and, of course, the CMB observations are used. The Planck collaboration discussed these issues in [186]. Variations of some fundamental constants, in particular, the fine structure constant α or the electron mass $m_{\rm e}$, can change the recombination history, which naturally affects the CMB fluctuations and the corresponding angular power spectrum (Fig. 37).

Due to the Planck experimental data, the precision of determining the possible variations of the constants at the recombination time ($z \sim 10^3$) could be improved almost

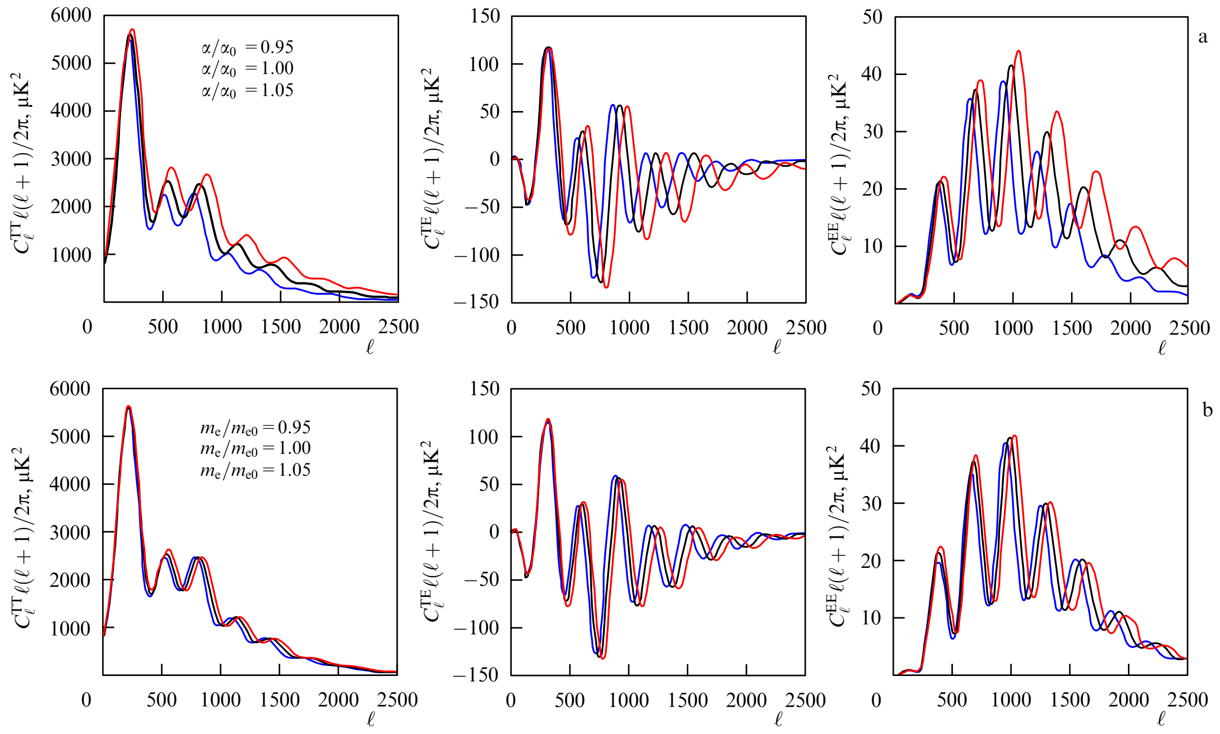

Figure 37. (Color online.) Model TT, TE, and EE angular power spectra of the CMB for different values of (a) the fine structure constant α and (b) the electron mass m_e. The curves show −5% (blue) and +5% (red) variations. The black curve corresponds to the standard parameters. (From [186].)

fivefold (specifically, by decreasing the admissible interval) over the WMAP results. The new constraints on the independent variations of constants inferred from the Planck data are $\Delta\alpha/\alpha = (3.6 \pm 3.7) \times 10^{-3}$ for the fine structure constant and $\Delta m_e/m_e = (4 \pm 11) \times 10^{-3}$ for the mass of the electron at the 68% confidence level. Bounds are also obtained for the possible spatial variation of α corresponding to the gradient across our Hubble volume: $\delta\alpha/\alpha = (-2.4 \pm 3.7) \times 10^{-2}$.

7. Anomalies

Anomalies in the CMB signal are considered in papers by the Planck collaboration devoted to the non-Gaussianity and isotropy [175, 176, 181, 183]. The main tests for the analysis of CMB isotropy include the use of the asymmetry and excess statistical moments, the Minkowski functional, spherical wavelets, N-point correlation functions, and peak statistics.

A statistical CMB anisotropy arises due to our motion in space filled with the CMB, which can be easily taken into account in the real data analysis. Apart from the explained violations of the statistical CMB isotropy, there are other deviations, which are, generally, signatures of non-Gaussianity. The 'standard' anomalies discovered in the WMAP data [187], which have been discussed in a number of papers [30, 188–198], have also been studied using the Planck data. We have already discussed searches for the non-Gaussianity and upper bounds derived from the Planck maps. However, non-Gaussianity can also appear as a statistical anisotropy, when the statistical properties of the CMB are different in different sky regions. A clear example is the low-multipole CMB signal (see Fig. 8), which shows the location of spots that 'know' the galactic or ecliptic coordinate system, as well as the direction of motion of Earth, which is highly improbable to expect from random CMB fluctuations. We note several effects on the CMB maps that were discovered in the WMAP data and persisted in the Planck measurements.

7.1 North–South power asymmetry on CMB maps

One of the effects on the CMB maps that we have already discussed is the North–South asymmetry of the signal in the galactic coordinates, which is also present in the ecliptical coordinates. A simple glance at the CMB map reveals that the number of hotter and colder spots in the southern hemisphere exceeds that in the northern hemisphere (see Figs 1 and 35). The asymmetry is easily confirmed by a variety of statistical tests that were done by the Planck collaboration. For a (symbolic) explanation, in particular, the Bianchi VII$_h$ model has been invoked, as discussed in Section 6.7. It cannot be ruled out that this anisotropy is accidental.

7.2 Axis of Evil

Another example of anisotropy is given by the close location of axes of two low harmonics, quadrupole and octupole. The axis along which the alignment of the spots occurs was dubbed the Axis of Evil.[8] This name was accepted in the physical literature. The Axis of Evil combines two effects observed on the WMAP and Planck maps (Fig. 38): 1) the effect of planarity — the quadrupole and octupole located along one plane such that the hot and cold spots of both harmonics lie along one line in the sky; 2) the effect of alignment — the virtual coincidence of axes perpendicular to the quadrupole and octupole planes. The coincidence of the quadrupole and octupole axes is most clearly seen in the WMAP data: the angle between the axes is $< 10°$. In the Planck data, this angle is 13° (see Fig. 38), which increases the

---

[8] Such was the original title of paper [181], later modified.

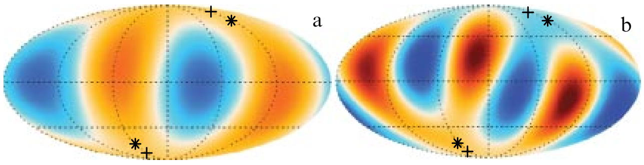

Figure 38. (Color online.) (a) The quadrupole and (b) the octupole on the CMB Planck map. The location of the perpendicular to the quadrupole and octupole axes is shown by the cross and asterisk, respectively. The angle between the axes is 13°. (From [181].)

probability of an arbitrary coincidence, but does not explain the sensitivity of the Axis of Evil to the direction of motion of Earth in the local cluster of galaxies and to the ecliptic coordinates. One interesting explanation for this anisotropy, suggested in [199], is related to the microwave emission from the Kuiper Belt.

In connection with the quadrupole, another anomalous effect has been discussed: its low amplitude, namely, the value of the coefficient $C_{\ell=2}$, which is below the admissible level determined by cosmic variance. Despite the Planck collaboration's conclusion [181] that the issue with the Axis of Evil is in fact resolved, Copi et al [200] applied different statistical tests of the quadrupole and octupole alignment to show that both harmonics are still connected with the direction of the dipole at a statistical significance above 3σ. We note that although the angle between the low harmonics is larger than 10° (alignment along a common direction is discussed in radio astronomy when the angle is less than 10°), the problem seems indeed to be unsolved. Both harmonics fix the ecliptic plane, whose width is more than 20°. We also note that the problems of the Axis of Evil and the quadrupole amplitude are frequently connected in the CMB studies, and both problems may be explained together.

7.3 Cold Spot

The origin of the anomaly called the Cold Spot, also located in the southern hemisphere (Fig. 39), remains unknown. This fluctuation, with a size of about 10°, also has an unusual form — three connected cold spots (on the smoothed map), with a deep minimum in the CMB signal in this region. Initially, this spot was noticed in 2005 by a Spanish group [189], who studied the difference in signal statistics between the northern and southern hemispheres using spherical wavelets. This group discovered that a significant deviation from the Gaussian statistics in the southern hemisphere is due to the presence of a spot on the galactic coordinates $(b, l) = (-57°, 209°)$ with a size of $\sim 10°$ and an amplitude below -4σ, where σ^2 is the dispersion of fluctuations. The probability of an accidental appearance of such a spot on the map with Gaussian fluctuations was estimated by map modeling and the wavelet method to be 0.2%. Without delving into a discussion of a different interpretation of the effect, we note that the spot is apparently related to the Galaxy, because it is present on the 408 MHz radio map (1982) dominated by synchrotron radiation, and also demonstrates a correlation with the galactic magnetic field [201].

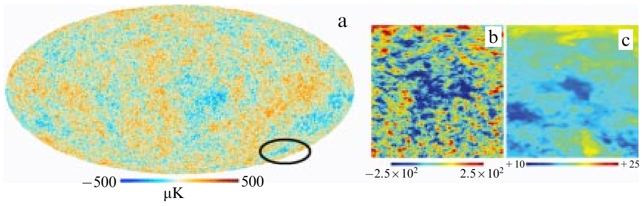

Figure 39. (Color online.) (a) Location of the Cold Spot on the CMB Planck map (the galactic coordinates of the center of the region: $l = 209°$, $b = -56°$). (b) The Cold Spot region 30° × 30°. (c) The Cold Spot region at 408 MHz, where the synchrotron foreground dominates.

7.4 Spectral parity violation

A remarkable anomalous property of the CMB map is related to parity asymmetry, first noticed by Kim and Naselsky [190]. The anomaly is that the fraction of the CMB power in even multipole numbers ℓ is significantly lower than that in multipoles with odd ℓ: at low harmonics, the spectral points C_ℓ with odd multipole numbers typically lie below those with even numbers. This anomaly is present in both WMAP and Planck data (Fig. 40). Using this property, a method for estimating the map quality using the CMB angular power spectrum C_ℓ was proposed. This approach is justified. In the standard cosmological model (which is now ΛCDM), the primordial random (Gaussian) perturbation field $\Phi(\mathbf{k})$ with a flat power spectrum gives rise to a plateau in the CMB angular power spectrum at low multipoles, $\ell(\ell+1)\,C_\ell \approx \text{const}$, due to the Sachs–Wolfe effect. Spherical harmonics change as $Y_{\ell m}(\hat{\mathbf{n}}) = (-1)^\ell Y_{\ell m}(-\hat{\mathbf{n}})$ under parity inversion. Therefore, the asymmetry in the angular power spectrum for even and odd harmonics can be considered the power asymmetry of even and odd map components.

The authors of [190] discovered that the power of odd multipoles systematically exceeds that of even multipoles at small ℓ, and called this phenomenon 'parity asymmetry'. To quantify this asymmetry, it was proposed to consider the ratio of the sum of squares of even multipoles P^+ to that of even multipoles P^-,

$$P^+ = \sum_{\text{even } \ell<\ell_{\max}} \frac{\ell(\ell+1)\,C_\ell}{2\pi}\,,$$

$$P^- = \sum_{\text{odd } \ell<\ell_{\max}} \frac{\ell(\ell+1)\,C_\ell}{2\pi}\,.$$

An interesting hypothesis proposed in [190] that the low amplitude of the CMB quadrupole can have the same origin as the parity asymmetry anomaly. In the Planck data analysis, Monte Carlo simulations showed that for only 0.2% of 1000 CMB simulations, the P^+/P^- ratio is in the tail of the distribution (Fig. 40) [183]. Due to the North–South CMB power asymmetry, which is more prominent for multipoles $2 \leqslant \ell \leqslant 19$ than for $20 \leqslant \ell \leqslant 40$, it is assumed that anomalies, including the hemisphere power asymmetry, the low amplitude of the quadrupole, and parity asymmetry have a common origin for low ℓ. Such anomalies could be explained by both cosmological arguments, by which the Universe for some reasons prefers the odd mode power, and an unknown effect of systematic uncertainties in observation and data analysis.

7.5 Low amplitude of low multipoles

The analysis of the Planck observations revealed one more anomalous effect. It turned out that at low multipoles $\ell \in [5; 30]$, the measured amplitudes of the CMB spectrum are lower than expected in the ΛCDM model [27, 117]. The power spectra of all four CMB maps presented by the Planck

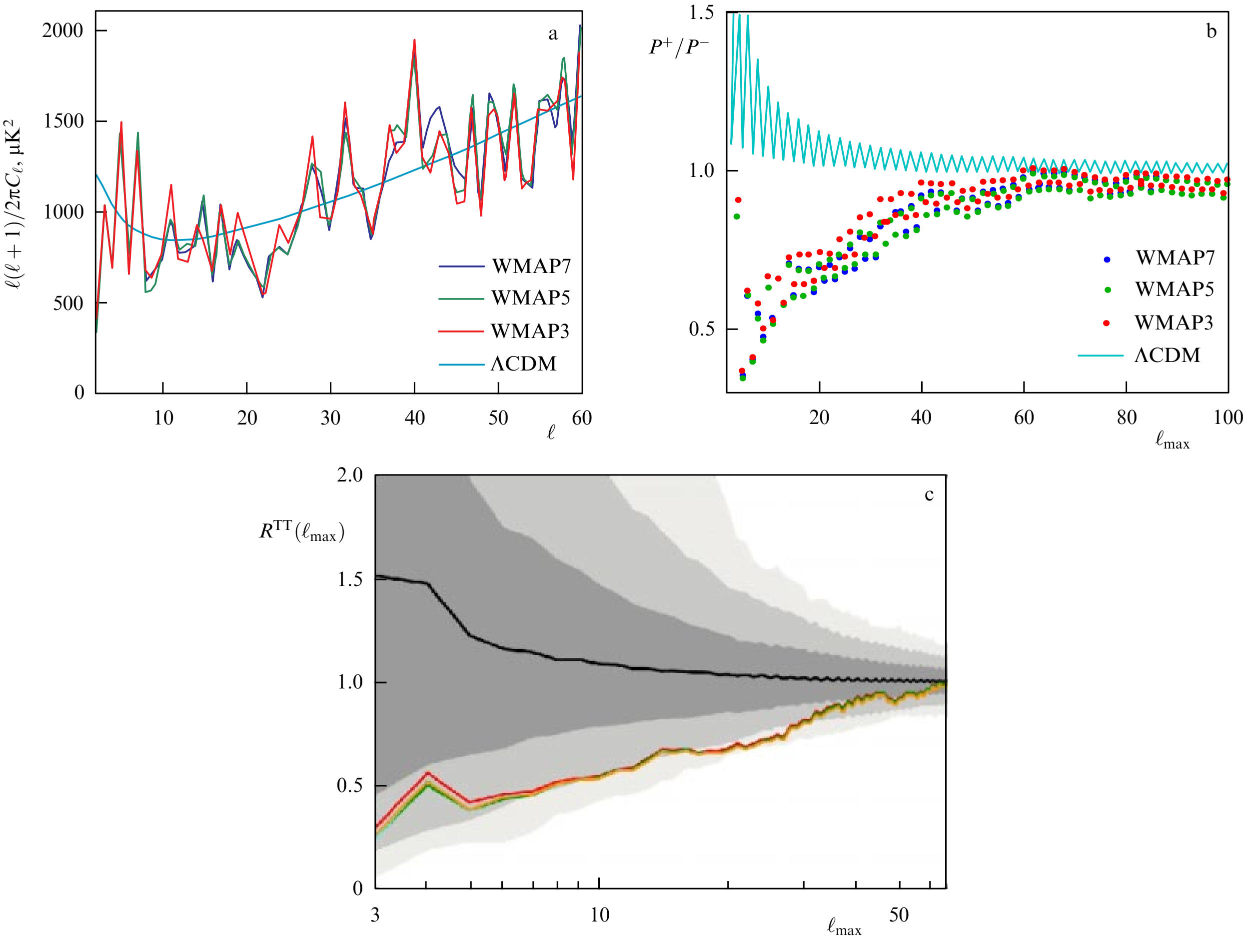

Figure 40. (Color online.) (a) Angular power spectrum (nonsmoothed) of the WMAP experiment has a saw-toothed shape — separation in the spherical harmonic number parity. (b) The ratio P^+/P^- of the sum of amplitudes of even multipoles to that of odd harmonics as a function of the number of the maximal multipole in the sum, $\ell_{\max}$. (From [190].) (c) The ratio $R^{\mathrm{TT}} = P^+/P^-$ for the CMB Planck 2015 Commander (red), NILC (orange), SEVEM (green), and SMICA (blue) maps as a function of $\ell_{\max}$. The shaded grey regions (from dark to light) indicate the respective 1σ, 2σ, and 3σ confidence regions. (From [183].)

collaboration differ at low multipoles by less than 50 μK^2 for each multipole. At the same time, the difference from the WMP9 ILC map is more than 100 μK^2, i.e., at the 2%–3% level. This difference cannot be due to Planck instrumental errors.

But the most intriguing is the relatively low amplitude of low multipoles leading to the 'tension' between the Planck data and the ΛCDM model, which best fits the measured power density in the entire frequency range, especially at the intermediate and high harmonics (see Fig. 26). The power deficit at low spectral frequencies $\ell \lesssim 40$ is 5%–10% at the 2.5–3σ statistical significance.

Thus, the Planck data [117] suggest that although the simplest ΛCDM model perfectly corresponds to the observed intermediate and small-scale angular CMB fluctuations, the inconsistency with data at low harmonics may signify that this model is incomplete.

7.6 Curiosity

As a curious fact, we note the presence of the so-called 'initials' of Steven Hawking on the microwave background WMAP map. In 2010, the Planck project scientist Jan Tauber claimed that these symbols are not on the Planck map. However, in Fig. 41, a region is seen that resembles Hawking's initials in the WMAP and Planck data. As can be noticed, on the new maps, 'dots' emerged near the 'letters' S and H. It should be noted that there is no physical meaning in identifying these symbols: this is simply the play of our imagination fitting templates for random signal distributions.

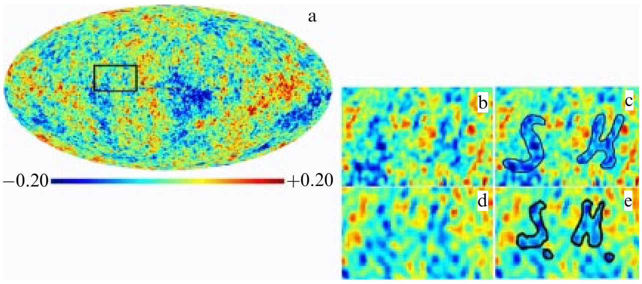

Figure 41. (Color online.) (a) Location of the region with SH templates on the WMAP CMB map. (b) The zoomed SH region. (c) Symbols SH contoured. (d) The zoomed SH region on the Planck map smoothed to the WMAP angular resolution. (d) The zones of the contoured SH symbols (with 'dots') on the Planck map.

8. Conclusion

Thus, of the three principal goals of the Planck mission — high-accuracy measurements of cosmological parameters, the search for and building of a catalogue of Sunyaev–Zeldovich galaxy clusters, and the measurement of the polarization B-mode signal to test the inflation theory — the first two can be considered to be completed. To achieve the third goal, additional observations with better sensitivity and frequency coverage and improvement of the polarization component separation methods from the CMB signal are required. The discovery of cold magnetized dust is also of great interest.

The results of measurements of cosmological parameters from the power spectra built from the temperature anisotropy and polarization Planck measurements confirmed [117] the base (standard) cosmological ΛCDM model. The Planck data improved the parameters of this model [117] (see Table 4 therein with the parameters consistent with other experiments). Among them are the angular size of the sound horizon at the epoch of last scattering estimated from the position of peaks in the angular power spectrum (in the notation $100 \times \theta_*$, i.e., multiplied by 100),[9] which is 1.04112 ± 0.00029 rad; the amplitude of primary density perturbations A_s multiplied by 10^{10} and written as a logarithm, $\ln(10^{10} A_s) = 3.064 \pm 0.023$; the scalar spectral index $n_s = 0.9667 \pm 0.0040$; densities of baryonic and dark matter, $\Omega_b h^2 = 0.02230 \pm 0.00014$ ($\Omega_b = 0.049$) and $\Omega_{CDM} h^2 = 0.1188 \pm 0.0010$ ($\Omega_{CDM} = 0.259$), as well as their relative sum, the matter density $\Omega_m = 0.3089 \pm 0.0062$; and the redshift z_{re} corresponding to the reionization epoch during which the neutral gas in the Universe became ionized again by the ultraviolet emission of the first stars and active galactic nuclei, $z_{re} = 8.8^{+1.2}_{-1.1}$. In calculations, instead of the parameter z_{re}, another but fully equivalent quantity is used: the optical depth τ in the reionization epoch, $\tau = 0.066 \pm 0.012$.

The above parameters fix the cosmological model and allow determining other parameters from the Planck data alone or in combination with other consistent experiments. Among other parameters, we note the density of dark energy $\Omega_\Lambda = 0.6911 \pm 0.0062$, which is related both to the value of θ_* and to the CMB photons passing through clusters of galaxies over cosmological time (the Sachs–Wolfe effect). Another important parameter is the present-day Hubble expansion parameter, the Hubble constant (according to the Planck data, $H_0 = 67.74 \pm 0.46$ km s^{-1} Mpc^{-1}). The Hubble parameter determines the age of the Universe $t_0 = 13.799 \pm 0.021$ bln years. The dispersion of the power spectrum of matter distribution can be calculated from the optical depth, which determines the properties of a medium and is related to the matter density, and the gravitational lensing data. It is described by the parameter $\sigma_8 = 0.8159 \pm 0.0086$ characterizing matter clustering inside an 8 Mpc volume. Another density parameter, $\Omega_K = 1 - \Omega_0$, describing the curvature of the Universe, is related to the total energy density Ω_0, which includes Ω_Λ, Ω_{CDM}, Ω_b, radiation and neutrino densities, and to the characteristic size of the CMB spots at the recombination time t_*. Using only the CMB data measured by Planck instruments, gravitational lensing data, and information from optical sky surveys, the curvature estimate is $\Omega_K = 0.0008^{+0.0040}_{-0.0039}$. The small value of Ω_K suggests that our Universe is flat with a high accuracy (i.e., the sum of the angles of any large-scale triangle is 180°), which in turn favors inflationary expansion in the early Universe.

We also note five parameters of the extended model: the mass of neutrinos $\sum m_{\nu_i} < 0.194$ eV, the effective number of neutrino species $N_{eff} = 3.04 \pm 0.33$, the primordial helium fraction $Y_P = 0.249^{+0.025}_{-0.026}$, the upper bound on the tensor-to-scalar perturbation modes $r_{0.002} < 0.113$, which is in agreement with Starobinsky's R^2 model, and the quintessence parameters for dark matter described by a dynamical field, $w = -1.0119^{+0.075}_{-0.80}$. A comparison of these results with the WMAP data is presented in Table 5.

Small but significant deviations between the Planck and WMAP results have been discussed in papers published by the Planck collaboration. The difference in the baryonic density Ω_b and the dark matter density Ω_Λ and, as a consequence, in the Hubble constant H_0, is explained in [118] by invoking an additional test — the analysis of cosmological parameters using CMB gravitational lensing by clusters of galaxies. This possibility was provided by the better angular resolution of the Planck instruments than that of WMAP, as well as by observations of additional baryons in large-scale structure filaments. In [202], possible reasons for discrepancies between the results are discussed. In particular, the component separation procedure by the WMAP methods (ILC map-making) and those used in the multi-frequency Planck 2013 data release is analyzed. It was found that exclusion of the 217 GHz data leads to good recovery (within a $< 1.1\sigma$ accuracy) of the WMAP9 results from the Planck data alone. The authors conclude that the 217 GHz data calibration may be problematic, which affected the results.

We note that the data processing pipeline, especially the destriping procedure, was later changed, which notably resulted in a difference between the Planck 2013 and Planck 2015 maps (Fig. 42). The most noticeable difference was found in the 217 GHz maps, which significantly contribute to the resulting Planck CMB maps. By analyzing the WMAP9 and Planck data for intermediate multipoles ($\ell > 100$), the authors of [203] came to several conclusions:

1) the observed sky is the same for both missions, but the observed harmonics are different;

2) the difference in the power spectra is stable and exceeds that allowed by the cosmic variance;

3) a single measurement of cosmological parameters has errors within the Gaussian uncertainty;

4) the deviation in joint determination of the six parameters leads to a 6σ error;

5) the strongest difference in the joint determination of parameters arises in $\Omega_{CDM} h^2$ and A_s;

6) the main influence on the cosmological parameters is due to effects related to the Planck antenna beam and is not related to the WMAP beam.

That the differences between both datasets are due to systematic uncertainties is supported by our comparison of the WMAP and Planck maps for harmonics that have the maximum difference in the CMB power spectra of both missions [204, 205].

Thus, it can be concluded that the ΛCDM model is firmly established from both the WMAP and Planck data. This is a beautiful result. Multiple measurements of the Sunyaev–Zeldovich effect, mapping of the galactic molecular gas and

---

[9] The parameter θ_* and the standard parameters θ_{MC} from Table 4 in Section 6 as calculated by the CosmoMC code [134] are very close but somewhat different, because they are derived from different approximations.

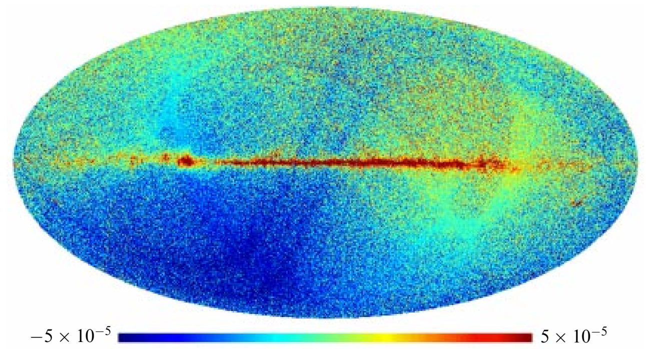

Figure 42. 2015 and 2013 217 GHz Planck map difference. The galactic emission (the central band) artefacts in the ecliptic plane reflecting the scan strategy of the Planck mission are visible.

other important results opened new possibilities in astrophysics. Anomalies on the CMB map still need convincing explanations.

Studies carried out by the Planck space mission, in addition to scientific results, afford a series of independent cosmological tests based exclusively on the CMB measurements:

- the angular power spectrum C_ℓ assessed separately at low ($2 \leqslant \ell \leqslant 50$), intermediate ($50 < \ell < 600$), and high harmonics for determination of the cosmological parameters;
- the correlation power spectra C_ℓ^{TE} and C_ℓ^{EE} for determination of the reionization parameters; low E-mode harmonics for the joint determination with C_ℓ^{TT} of the cosmological parameters;
- the correlation power spectra C_ℓ^{TB} and C_ℓ^{BB} for searches for relic gravitational waves and determination of parameters of the inflationary model;
- statistical properties of the signal: Gaussianity as the inflationary model parameter; the amplitude of harmonics as the parameter to analyze the topology and geometry of the Universe; statistical anisotropy as a test for the complicated inflationary model;
- clusters of galaxies appearing on the CMB map due to the Sunyaev–Zeldovich effect as a tool to measure some cosmological parameters and galaxy cluster masses;
- CMB lensing;
- CMB maps as a test of the topology of the Universe.

Due to better angular resolution and sensitivity, the number of tests performed by the Planck mission is much larger than in the WMAP mission. The independent parameter determinations and a large number of points in the angular power spectrum, whose amplitudes have been checked and improved many times, undoubtedly lend credence to the data obtained and to the results of their analysis.

We note that the CMB studies have not been completed. It is necessary to improve taking the emission of cold magnetized dust into account to advance the studies of the polarization B-mode. The incompleteness of the catalogue of SZ galaxy clusters is obvious. The flux measurements from point-like sources at a $< 5\sigma$ level in the Planck maps is of additional interest for studies of the signal anisotropy at high harmonics. Studies of the CMB anomalies also continue.

Acknowledgments

The author is deeply grateful to the referee for the useful comments that improved the presentation and allowed reflecting unrevealed topics. The author also thanks his colleagues A G Doroshkevich, P D Naselsky, V A Rubakov, I D Novikov, and V N Lukash for the fruitful discussions of the studies presented here. In addition, it is a pleasant duty to thank Dmitry Zimin's noncommercial Dynasty Foundation for support of the studies, which helped to prepare this review. The study used the ESA's publicly available Planck Legacy Archive and NASA's WMAP archive (Lambda). The data analysis and the CMB maps were made using the GLESP package [22, 23]. The work is supported by the Russian Foundation for Basic Research (grant 13-02-00027).

References

1. Bennett C L et al. *Astrophys. J. Suppl.* **148** 1 (2003); astro-ph/0302207
2. Bennett C L et al. *Astrophys. J. Suppl.* **148** 97 (2003); astro-ph/0302208
3. Spergel D N et al. *Astrophys. J. Suppl.* **148** 175 (2003); astro-ph/0302209
4. Hinshaw G et al. *Astrophys. J. Suppl.* **170** 288 (2007); astro-ph/0603451
5. Hinshaw G et al. *Astrophys. J. Suppl.* **180** 225 (2009); arXiv:0803.0732
6. Jarosik N et al. *Astrophys. J. Suppl.* **192** 14 (2011); arXiv:1001.4744
7. Bennett C L et al. *Astrophys. J. Suppl.* **208** 20 (2013)
8. Hinshaw G et al. *Astrophys. J. Suppl.* **208** 19 (2013)
9. Aghanim N et al. (Planck Collab.) *Astrophys. Astrophys.* **571** A4 (2014)
10. Ade P et al. (Planck Collab.) *Astrophys. Astrophys.* **571** A7 (2014)
11. Ade P et al. (Planck Collab.) *Astrophys. Astrophys.*, submitted; arXiv:1502.01582
12. Ade P et al. (Planck Collab.) *Astron. Astrophys.*, submitted; arXiv:1502.01585
13. Ade P et al. (Planck Collab.) *Astrophys. Astrophys.* **571** A2 (2014)
14. Keihänen E et al. *Astron. Astrophys.* **510** A57 (2010); arXiv:0907.0367
15. Ade P et al. (Planck Collab.) *Astrophys. Astrophys.*, submitted; arXiv:1507.08853
16. Ade P et al. (Planck Collab.) *Astrophys. Astrophys.*, submitted; arXiv:1502.01586
17. Ade P et al. (Planck Collab.) *Astrophys. Astrophys.*, submitted; arXiv:1502.01587
18. Górski K M et al. *Astrophys. J.* **622** 759 (2005)
19. Verkhodanov O V, Doroshkevich A G *Phys. Usp.* **56** 801 (2013); *Usp. Fiz. Nauk* **183** 849 (2013)
20. Crittenden R G, Turok N G "Exactly azimuthal pixelizations of the sky", Report DAMTP-1998-78 (1998); astro-ph/9806374
21. Tegmark M *Astrophys. J.* **480** L87 (1997); astro-ph/9611130
22. Doroshkevich A G et al. *Int. J. Mod. Phys. D* **14** 275 (2005); astro-ph/0305537
23. Doroshkevich A G et al. *Int. J. Mod. Phys. D* **20** 1053 (2011); arXiv:0904.2517
24. Jones W C et al. *Astropys. J.* **647** 823 (2006); astro-ph/0507494
25. Stompor R et al. *Phys. Rev. D* **65** 022003 (2003); astro-ph/0106451
26. Naess S *JCAP* (10) 007 (2014); arXiv:1405.5524
27. Planck Collab. *Astrophys. Astrophys.* **536** A1 (2011)
28. Verkhodanov O V *Phys. Usp.* **55** 1098 (2012); *Usp. Fiz. Nauk* **182** 1177 (2012)
29. Tegmark M, Efstathiou G *Mon. Not. R. Astron. Soc.* **281** 1297 (1996)
30. Tegmark M, de Oliveira-Costa A, Hamilton A *Phys. Rev. D* **68** 123523 (2003)
31. Bonaldi A et al. *Mon. Not. R. Astron. Soc.* **382** 1791 (2008)
32. Kim J, Naselsky P, Christensen P R *Phys. Rev. D* **79** 023003 (2009)
33. Maino D et al. *Mon. Not. R. Astron. Soc.* **374** 1207 (2007); astro-ph/0609228
34. Stolyarov V et al. *Mon. Not. R. Astron. Soc.* **336** 97 (2002)
35. Leach S M et al. *Astron. Astrophys.* **491** 597 (2008); arXiv:0805.0269
36. Doroshkevich A G, Verkhodanov O V *Phys. Rev. D* **83** 043002 (2011); arXiv:1008.4094
37. Ade P et al. (Planck Collab.) *Astrophys. Astrophys.* **571** A12 (2014)

38. Ade P et al. (Planck Collab.) *Astrophys. Astrophys.*, submitted; arXiv:1502.05956
39. Wandelt B D, Larson D L, Lakshminarayanan A *Phys. Rev. D* **70** 083511 (2004)
40. Eriksen H K et al. *Astropys. J.* **676** 10 (2008); arXiv:0709.1058
41. Haslam C G T et al. *Astron. Astrophys.* **47** 1 (1982)
42. Delabrouille J et al. *Astron. Astrophys.* **493** 835 (2009)
43. Martinez-Gonzalez E et al. *Mon. Not. R. Astron. Soc.* **345** 1101 (2003)
44. Ade P et al. (Planck Collab.) *Astrophys. Astrophys.*, submitted; arXiv:1502.01588
45. Ade P et al. (Planck Collab.) *Astron. Astrophys.* **571** A6 (2014)
46. Ade P et al. (Planck Collab.) *Astron. Astrophys.* **571** A11 (2014)
47. Ade P et al. (Planck Collab.) *Astron. Astrophys.* **571** A14 (2014); arXiv:1303.5074
48. Ade P et al. (Planck Collab.) *Astron. Astrophys.* **566** A55 (2014)
49. Ade P et al. (Planck Collab.) *Astron. Astrophys.* **576** A104 (2015)
50. Draine B T, Lazarian A *Astrophys. J.* **508** 157 (1998)
51. de Oliveira-Costa A et al. *Astrophys. J.* **567** 363 (2002)
52. Finkbeiner D P et al. *Astrophys. J.* **617** 350 (2004)
53. Semenova T A, Pariiskii Yu N, Bursov N N *Astron. Rep.* **53** 1 (2009); *Astron. Zh.* **86** 3 (2009)
54. Komatsu E et al. *Prog. Theor. Exp. Phys.* (6) 06B10224 (2014); arXiv:1404.5415
55. Ali-Haimoud Y, Hirata C M, Dickinson C *Mon. Not. R. Astron. Soc.* **395** 1055 (2009)
56. Silsbee K, Ali-Haimoud Y, Hirata C M *Mon. Not. R. Astron. Soc.* **411** 2750 (2011)
57. Ade P et al. (Planck Collab.) *Astron. Astrophys.* **571** A13 (2014)
58. Zeldovich Ya B, Sunyaev R A *Astrophys. Space Sci.* **4** 301 (1969)
59. Battistelli E S et al. *Astrophys. J.* **598** L75 (2003); astro-ph/0303587
60. Diego J M, Ascasibar Y *Mon. Not. R. Astron. Soc.* **389** 1805 (2008); arXiv:0804.0432
61. Aghanim M et al. (Planck Collab.) *Astrophys. Astrophys.*, submitted; arXiv:1502.01596
62. Ade P et al. (Planck Collab.) *Astron. Astrophys.* **571** A30 (2014)
63. Zaldarriaga M, Seljak U *Phys. Rev. D* **55** 1830 (1997); astro-ph/9609170
64. Kamionkowski M, Kosowsky A, Stebbins A *Phys. Rev. D* **55** 7368 (1997); astro-ph/9611125
65. Pacholczyk A G *Radio Astrophysics. Nonthermal Processes in Galactic and Extragalactic Sources* (San Francisco: W. H. Freeman, 1970)
66. Page L et al. *Astrophys. J. Suppl.* **170** 335 (2007); astro-ph/0603450
67. Kogut A et al. *Astrophys. J. Suppl.* **665** 355 (2007); arXiv:0704.3991
68. Vidal M et al. *Mon. Not. R. Astron. Soc.* **452** 656 (2015); arXiv:1410.4438
69. Ade P A R et al. (Planck Collab.) *Astrophys. Astrophys.*, submitted; arXiv:1506.06660
70. Ade P et al. (Planck Collab.) *Astron. Astrophys.* **564** A45 (2014)
71. Ade P et al. (Planck Collab.) *Astron. Astrophys.* **576** A104 (2015)
72. Ade P et al. (Planck Collab.) *Astron. Astrophys.* **576** A105 (2015)
73. Ade P et al. (Planck Collab.) *Astron. Astrophys.* **576** A106 (2015)
74. Ade P et al. (Planck Collab.) *Astron. Astrophys.* **576** A107 (2015)
75. Adam R et al. (Planck Collab.) *Astron. Astrophys.* **586** A133 (2016); arXiv:1409.5738
76. Abergel A et al. (Planck Collab.) *Astron. Astrophys.* **536** A24 (2011); arXiv:1101.2036
77. Ade P et al. (Planck Collab.) *Astron. Astrophys.* **571** A13 (2014)
78. Ade P et al. (Planck Collab.) *Astron. Astrophys.* **536** A22 (2011)
79. Ade P et al. (Planck Collab.) *Astron. Astrophys.* **536** A23 (2011)
80. Ade P et al. (Planck Collab.) *Astron. Astrophys.* **536** A20 (2011)
81. Ade P et al. (Planck Collab.) *Astron. Astrophys.* **536** A19 (2011); arXiv:1101.2029
82. Ade P et al. (Planck Collab.) *Astron. Astrophys.* **586** A132 (2016); arXiv:1409.2495
83. Ade P et al. (Planck Collab.) *Astron. Astrophys.* **557** A53 (2013)
84. Ade P et al. (Planck Collab.) *Astron. Astrophys.* **554** A139 (2013); arXiv:1208.5483
85. Finkbeiner D P *Astropys. J.* **614** 186 (2004)
86. Dobler G, et al. *Astrophys. J.* **717** 825 (2010)
87. Ade P et al. (Planck Collab.) *Astron. Astrophys.* **536** A17 (2011)
88. Ade P et al. (Planck Collab.) *Astron. Astrophys.* **582** A28 (2015); arXiv:1407.5452
89. Ade P et al. (Planck Collab.) *Astron. Astrophys.* **536** A7 (2011)
90. Ade P et al. (Planck Collab.) *Astron. Astrophys.* **536** A13 (2011)
91. Ade P et al. (Planck Collab.) *Astron. Astrophys.* **550** A133 (2013); arXiv:1207.4706
92. Ade P et al. (Planck Collab.) *Astron. Astrophys.* **571** A28 (2014); arXiv:1303.5088
93. Ade P et al. (Planck Collab.) *Astron. Astrophys.*, submitted; arXiv:1507.02058
94. Verkhodanov O V et al. *Astrophys. Bull.* **70** 156 (2015); *Astrofiz. Byull.* **70** 164 (2015)
95. Verkhodanov O V et al. *Astron. Lett.* **41** 457 (2015); *Pis'ma Astron. Zh.* **41** 499 (2015)
96. Ade P et al. (Planck Collab.) *Astron. Astrophys.*, submitted; arXiv:1508.04171
97. Sunyaev R A, Zeldovich Ya B *Astrophys. Space Sci.* **7** 3 (1970)
98. Ade P et al. (Planck Collab.) *Astron. Astrophys.* **557** A52 (2013)
99. Ade P et al. (Planck Collab.) *Astron. Astrophys.* **571** A21 (2014)
100. Ade P et al. (Planck Collab.) *Astron. Astrophys.* **571** A20 (2014)
101. Ade P et al. (Planck Collab.) *Astron. Astrophys.*, submitted; arXiv:1502.01597
102. Vikhlinin A A et al. *Phys. Usp.* **57** 317 (2014); *Usp. Fiz. Nauk* **184** 339 (2014)
103. Kompaneets A S *Sov. Phys. JETP* **4** 730 (1957); *Zh. Eksp. Teor. Fiz.* **31** 876 (1956)
104. Ade P et al. (Planck Collab.) *Astron. Astrophys.* **550** A129 (2013); arXiv:1204.2743
105. Ade P et al. (Planck Collab.) *Astron. Astrophys.* **550** A134 (2013)
106. Ade P et al. (Planck Collab.) *Astron. Astrophys.* **550** A132 (2013)
107. Kashlinsky A et al. *Astrophys. J.* **712** 81 (2010); arXiv:0910.4958
108. Atrio-Barandela F et al. *Astrophys. J.* **719** 77 (2010); arXiv:1001.1261
109. Planck Collab. *Astron. Astrophys.* **561** A97 (2014)
110. Planck Collab. *Astron. Astrophys.* **536** A18 (2011)
111. Naselsky P D, Novikov D I, Novikov I D *Reliktovoe Izluchenie Vselennoi* (Relic Radiation in the Universe) (Moscow: Nauka, 2003)
112. Gorbunov D S, Rubakov V A *Introduction to the Theory of the Early Universe*: *Cosmological Perturbations and Inflationary Theory* (Singapore: World Scientific, 2011); Translated from Russian *Vvedenie v Teoriyu Rannei Vselennoi*: *Kosmologicheskie Vozmushcheniya. Inflyatsionnaya Teoriya* (Moscow: KRASAND, 2010)
113. Lukash V N, Mikheeva E V *Fizicheskaya Kosmologiya* (Physical Cosmology) (Moscow: Fizmatlit, 2010)
114. Sakharov A D *Zh. Eksp. Teor. Fiz.* **49** 345 (1965)
115. Komatsu E, Spergel D N *Phys. Rev. D* **63** 063002 (2001); astro-ph/0005036
116. Lewis A, Challinor A, Lasenby A *Astrophys. J.* **538** 473 (2000); astro-ph/9911177
117. Ade P et al. (Planck Collab.) *Astron. Astrophys.*, submitted; arXiv:1502.01589
118. Ade P et al. (Planck Collab.) *Astron. Astrophys.* **571** A16 (2014)
119. Pisanti O et al. *Comput. Phys. Commun.* **178** 956 (2008)
120. Hirata C M *Phys. Rev. D* **78** 023001 (2008)
121. Chluba J, Thomas R M *Mon. Not. R. Astron. Soc.* **412** 748 (2011)
122. Shaw J R, Chluba J *Mon. Not. R. Astron. Soc.* **415** 1343 (2011)
123. Lukash V N, Rubakov V A *Phys. Usp.* **51** 283 (2008); *Usp. Fiz. Nauk* **178** 301 (2008)
124. Sahni V, Starobinsky A *Int. J. Mod. Phys. D* **9** 373 (2000)
125. Bond J R, Efstathiou G *Mon. Not. R. Astron. Soc.* **226** 655 (1987)
126. Sugiyama N *Astropys. J. Suppl.* **100** 281 (1995)
127. Ma C.-P, Bertschinger E *Astrophys. J.* **455** 7 (1995)
128. Seljak U, Zaldarriaga M *Astrophys. J.* **469** 437 (1996); astro-ph/9603033
129. Zaldarriaga M, Seljak U, Bertschinger E *Astrophys. J.* **494** 491 (1998)
130. Lesgourgues J, Tram T *JCAP* (09) 032 (2011)
131. Planck Collab. *Astron. Astrophys.* **571** A17 (2014)
132. Smith R E et al. *Mon. Not. R. Astron. Soc.* **341** 1311 (2003)
133. Takahashi R et al. *Astrophys. J.* **761** 152 (2012)
134. Lewis A, Bridle S *Phys. Rev. D* **66** 103511 (2002); astro-ph/0205436
135. Ade P et al. (Planck Collab.) *Astron. Astrophys.*, subimtted; arXiv:1502.01583

136. Ade P et al. (Planck Collab.) *Astron. Astrophys.*, subimtted; arXiv:1507.02704
137. Ade P et al. (Planck Collab.) *Astron. Astrophys.* **571** A15 (2014)
138. Lewis A *Phys. Rev. D* **87** 103529 (2013)
139. Ade P et al. (Planck Collab.) *Astron. Astrophys.* DOI: 10.1051/0004-6361/201525941; arXiv:1502.01591
140. Knox L, Song Y-S *Phys. Rev. Lett.* **89** 011303 (2002); astro-ph/0202286
141. Challinor A, Lewis A *Phys. Rev. D* **71** 103010 (2005); astro-ph/0502425
142. Lewis A, Challinor A *Phys. Rep.* **429** 1 (2006); astro-ph/0601594
143. Hirata C M et al. *Phys. Rev. D* **70** 103501 (2004); astro-ph/0406004
144. Smith K M et al. *Phys. Rev. D* **76** 043510 (2007); arXiv:0705.3980
145. Hirata C M et al. *Phys. Rev. D* **78** 043520 (2008); arXiv:0801.0644
146. Das S et al. *JCAP* (04) 014 (2014); arXiv:1301.1037
147. Story K T et al. *Astrophys. J.* **779** 86 (2013); arXiv:1210.7231
148. Smith K M et al. *AIP Conf. Proc.* **1141** 121 (2009); arXiv:0811.3916
149. Okamoto T, Hu W *Phys. Rev. D* **67** 083002 (2003); astro-ph/0301031
150. van Engelen A et al. *Astrophys. J.* **756** 142 (2012); arXiv:1202.0546
151. Anderson L et al. *Mon. Not. R. Astron. Soc.* **441** 24 (2014); arXiv:1312.4877
152. Ross A J et al. *Mon. Not. R. Astron. Soc.* **449** 835 (2015); arXiv:1409.3242
153. Beutler F et al. *Mon. Not. R. Astron. Soc.* **416** 3017 (2011); arXiv:1106.3366
154. Ade P et al. (Planck Collab.) *Astron. Astrophys.*, subimtted; arXiv:1502.02114
155. Ade P et al. (Planck Collab.) *Astron. Astrophys.* **571** A22 (2014)
156. Ade P et al. (Planck Collab.) *Astron. Astrophys.* **571** A25 (2014)
157. Ijjas A, Steinhardt P J, Loeb A *Phys. Lett. B* **723** 261 (2013); arXiv:1304.2785
158. Guth A H, Kaiser D I, Nomura Y *Phys. Lett. B* **733** 112 (2014); arXiv:1312.7619
159. Linde A, arXiv:1402.0526
160. Ijjas A, Steinhardt P J, Loeb A *Phys. Lett. B* **736** 142 (2014); arXiv:1402.6980
161. Starobinsky A A *Phys. Lett. B* **91** 99 (1980)
162. Mukhanov V F, Chibisov G V *JETP Lett.* **33** 532 (1981); *Pis'ma Zh. Eksp. Teor. Fiz.* **33** 549 (1981)
163. Ade P et al. (BICEP2 Collab.) *Astrophys. J.* **792** 62 (2014); arXiv:1403.4302
164. Ade P et al. (BICEP2 Collab.) *Phys. Rev. Lett.* **112** 241101 (2014); arXiv:1403.3985
165. Grishchuk L P *Sov. Phys. JETP* **40** 409 (1975); *Zh. Eksp. Teor. Fiz.* **67** 825 (1974)
166. Starobinskii A A *JETP Lett.* **30** 682 (1979); *Pis'ma Zh. Eksp. Teor. Fiz.* **30** 719 (1979)
167. Rubakov V A, Sazhin M V, Veryaskin A V *Phys. Lett. B* **115** 189 (1982)
168. Sato K *Mon. Not. R. Astron. Soc.* **195** 467 (1981)
169. Polnarev A G *Sov. Astron.* **29** 607 (1985); *Astron. Zh.* **62** 1041 (1985)
170. Seljak U *Astrophys. J.* **482** 6 (1997)
171. Planck Collab. *Astron. Astrophys.* **571** A19 (2014)
172. Ade P A R et al. (BICEP2/Keck, Planck Collab.) *Phys. Rev. Lett.* **114** 101301 (2015); arXiv:1502.00612
173. Creminelli P et al. *JCAP* (05) 004 (2006); astro-ph/0509029
174. Senatore L, Smith K M, Zaldarriaga M *JCAP* (01) 028 (2010); arXiv:0905.3746
175. Ade P et al. (Planck Collab.) *Astron. Astrophys.*, submitted; arXiv:1502.01592
176. Ade P et al. (Planck Collab.) *Astron. Astrophys.* **571** A24 (2014)
177. Liu H, Mertsch P, Sarkar S *Astrophys. J.* **789** L29 (2014); arXiv:1404.1899
178. Mortonson M J, Seljak U *JCAP* (10) 035 (2014); arXiv:1405.5857
179. Flauger R, Hill J C, Spergel D N *JCAP* (08) 039 (2014); arXiv:1405.7351
180. Adam R et al. (Planck Collab.) *Astron. Astrophys.* **586** A133 (2016); arXiv:1409.5738
181. Ade P et al. (Planck Collab.) *Astron. Astrophys.* **571** A22 (2014)
182. Ade P et al. (Planck Collab.) *Astron. Astrophys.* **571** A2 (2014)
183. Ade P et al. (Planck Collab.) *Astron. Astrophys.*, submitted; arXiv:1506.07135
184. Ade P et al. (Planck Collab.) *Astron. Astrophys.*, submitted; arXiv:1502.01593
185. Varshalovich D A, Levshakov S A, Potekhin A Yu *Phys. Usp.* **36** 642 (1993); *Usp. Fiz. Nauk* **163** (7) 111 (1993)
186. Ade P A R et al. (Planck Collab.) *Astron. Astrophys.* **580** A22 (2015); arXiv:1406.7482
187. Bennett C L et al. *Astrophys. J. Suppl.* **192** 17 (2011); arXiv:1001.4758
188. Land K, Magueijo J *Phys. Rev. Lett.* **95** 071301 (2005)
189. Cruz M et al. *Mon. Not. R. Astron. Soc.* **356** 29 (2005)
190. Kim J, Naselsky P *Astrophys. J.* **714** L265 (2010)
191. Eriksen H K et al. *Astrophys. J.* **605** 14 (2004)
192. Copi C J et al. *Mon. Not. R. Astron. Soc.* **367** 79 (2006); astro-ph/0508047
193. Gruppuso A, Burigana C *JCAP* (08) 004 (2009)
194. Naselsky P D, Verkhodanov O V *Astrophys. Bull.* **62** 203 (2007); *Astrofiz. Byull.* **62** 218 (2007)
195. Naselsky P D, Verkhodanov O V, Nielsen M T B *Astrophys. Bull.* **63** 216 (2008); *Astrofiz. Byull.* **63** 231 (2008); arXiv:0707.1484
196. Verkhodanov O V, Khabibullina M L, Majorova E K *Astrophys. Bull.* **64** 263 (2009); *Astrofiz. Byull.* **64** 272 (2009); arXiv:0912.3073
197. Verkhodanov O V, Khabibullina M L *Astrophys. Bull.* **65** 390 (2010); *Astrofiz. Byull.* **65** 413 (2010); arXiv:1108.4128
198. Naiden Ya V, Verkhodanov O V *Astrophys. Bull.* **69** 488 (2014); *Astrofiz. Byull.* **69** 517 (2014)
199. Hansen M et al. *JCAP* (10) 059 (2012); arXiv:1206.6981
200. Copi C J et al. *Mon. Not. R. Astron. Soc.* **449** 3458 (2015); arXiv:1311.4562
201. Hansen M et al. *Mon. Not. R. Astron. Soc.* **426** 57 (2012); arXiv:1202.1711
202. Spergel D, Flauger R, Hlozek R *Phys. Rev. D* **91** 023518 (2015); arXiv:1312.3313
203. Larson D et al. *Astrophys. J.* **801** 9 (2015); arXiv:1409.7718
204. Verkhodanov O V *Astrophys. Bull.* **69** 330 (2014); *Astrofiz. Byull.* **69** 350 (2014)
205. Verkhodanov O V *Phys. Part. Nucl.* **46** 237 (2015); *Fiz. Elem. Chast. At. Yad.* **46** 422 (2015)